Spontaneous Electromagnetic Emission from a Strongly Localized Plasma Flow

by

Erik M. Tejero

A dissertation submitted to the Graduate Faculty of
Auburn University
in partial fulfillment of the
requirements for the Degree of
Doctor of Philosophy

Auburn, Alabama
May 9, 2011

Keywords: plasma waves, plasma instabilities, velocity shear

Approved by

Edward Thomas, Jr., Chair, Professor of Physics
William Amatucci, Staff Scientist at Naval Research Laboratory
Stephen Knowlton, Professor of Physics
Minseo Park, Professor of Physics
Roy Hartfield, Professor of Aerospace Engineering

Abstract

The laboratory experiments described in this dissertation establish that strongly localized DC electric fields perpendicular to the ambient magnetic field can behave as a radiation source for electromagnetic ion cyclotron waves, transporting energy away from the region of wave generation.

This investigation is motivated by numerous space observations of electromagnetic ion cyclotron waves. Ion cyclotron waves are important to space weather dynamics due to their ability to accelerate ions transverse to the background magnetic field, leading to ion outflows in the auroral regions. Many different theoretical mechanisms have been presented to account for these waves. Sheared flows produced by localized electric fields coupled with a perpendicular magnetic field are a potentially important energy source that can create waves of this type.

In situ observations of sheared plasma flows collocated with electromagnetic wave activity have led to this laboratory effort to investigate the impact of electromagnetic, velocity shear-driven instabilities on the near-Earth space plasma dynamics. Under scaled ionospheric conditions in the Space Physics Simulation Chamber at the Naval Research Laboratory (NRL), the transition from electrostatic to electromagnetic ion cyclotron (EMIC) wave propagation has been investigated.

Previous experiments at West Virginia University, NRL, and Auburn University demonstrated that transverse sheared plasma flows can independently drive electrostatic ion cyclotron waves. It was also observed that these waves were capable of heating the ions in the direction transverse to the magnetic field. The general wave characteristics and wave dispersion experimentally observed are in agreement with the current theoretical models. The electrostatic waves generated in the experiments described in this dissertation were consistent with the previous electrostatic experiments described above. In addition, the electromagnetic component of these waves increase by two orders of magnitude as the plasma β was increased.

The EMIC waves exhibited an electric field threshold of 60.5 V/m and their frequency increased as the applied electric field increased. The observed EMIC waves are predominantly azimuthally propagating $m = 1$ cylindrical waves, which propagate in the direction of the $\mathbf{E} \times \mathbf{B}$ drift. A velocity shear modified dispersion relation was derived from the Peñano and Ganguli model for electromagnetic waves in the presence of sheared flows, and the dispersion relation is compared with experimental observations.

Acknowledgments

I would like to acknowledge my advisors Dr. Edward Thomas, Jr. and Dr. William Amatucci with special thanks to Dr. Amatucci for his day-to-day guidance and encouragement without whom this would not have been possible. The critical reading and assessment of the this document and the experimental results in general by Dr. Christopher Cothran were invaluable in keeping me on the right track. Theory guidance and gentle prodding by Dr. Gurudas Ganguli and Dr. Christopher Crabtree are greatly appreciated. I would like to acknowledge Mr. George Gatling for software and hardware support. I would also like to thank the rest of my committee, Dr. Stephen Knowlton and Dr. Minseo Park, as well as my outside reader Dr. Roy Hartfield for being willing to read this dissertation. Last but certainly not least, I would like to thank Hannah Kurtis for being willing to put up with me in general and for helping to keep me sane throughout this process.

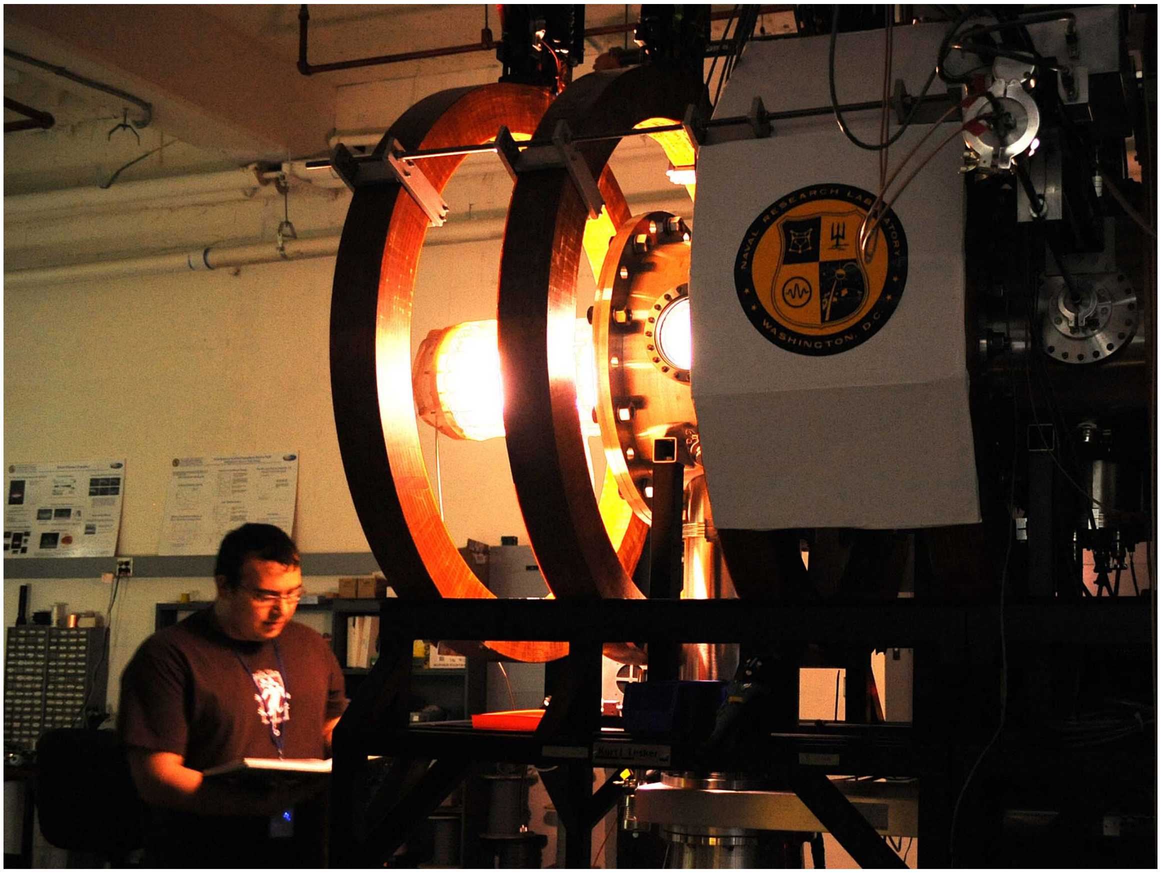

Figure 1: The author basking in the warm glow of his plasma.

Table of Contents

List of Figures

List of Tables

Chapter 1

Introduction

Strongly localized plasma flows are capable of driving a variety of instabilities in a wide range of plasma environments from space to fusion plasmas. Sheared plasma flows transverse to the background magnetic field have been predicted to drive Alfvén waves for a large range of frequencies below the ion cyclotron frequency. Of particular interest are Alfvén waves near the ion cyclotron frequency due to their ability to heat ions and affect bulk plasma transport. We present the results from a directed laboratory investigation confirming the spontaneous generation of electromagnetic ion cyclotron waves due to these transverse sheared flows.

In the following sections of the introduction, we will discuss the motivation for this work by examining some of the unresolved questions posed by observations in space and how the presence of localized, small-scale electric field structures can play an important role in resolving these outstanding issues. Space observations suffer from a variety of complications that can make it very difficult to definitively test the theoretical solutions posed. There is often an ambiguity in determining whether an observation is a result of a temporal or spatial process, and there is a lack of a reproducible environment where parameters can be isolated and tested individually. Laboratory experiments can play a key role in verifying theoretical models and assisting in the interpretation of *in situ* data, since experiments can be conducted in a controlled, reproducible fashion to isolate the process under investigation and are designed to be diagnosed thoroughly. In the last section we present a review of the laboratory experiments that paved the way for the current investigation.

1.1 Motivation

Since the initial observation of ionospheric ion outflows [92], a number of different sources of magnetospheric plasma have been identified. These ionospheric sources include the polar wind

[11], cleft ion fountain [63], polar cap outflows [93], and ion fluxes in the auroral zone [92] and can account for a significant fraction of the magnetospheric plasma. The H^+ and He^+ ions that comprise the polar wind, which was theoretically predicted by Banks and Holzer [12] and later confirmed by observations [75], is a dominant source of particle flux.

O^+ ions, originating from low-altitude, cold, gravitationally bound ionospheric distributions, were observed to be accelerated to energies sufficient to overcome gravity and outflow to the magnetosphere. Ion drift measurements in the cleft ion fountain and the presence of O^+ ions in the plasma sheet and ring current have led to the conclusion that these ion outflows are the dominant source of mass in the magnetosphere [23]. These energetic ion flows: ion beams, ion conics, and upwelling ions, are identified by their energy, angular distribution in velocity space, and spatial location [110]. The origin of the ion fluxes in the auroral zone and the cleft ion fountain, however, is not well understood.

A majority of the ionospheric ion outflow is directly associated with the auroral zone and is caused by perpendicular energization of all major ion species. This extra perpendicular energy can be converted to parallel energy via the mirror force. The accelerated ions travel up the field lines of the divergent terrestrial magnetic field and form conic-shaped distributions in velocity space [8]. Transversely accelerated ions (TAI) have been observed by several sounding rockets: SCIFER [54] and AMICIST [16], and by numerous satellites: Hilat [101], Freja [7], FAST [20], and CLUSTER [103] at altitudes from 400 km to greater than 4000 km and with energies ranging from 1 eV to 1 keV. TAI are an important part of the coupling between the ionosphere and the magnetosphere. The physical mechanism for the acceleration is the interaction between the ions and electric fields at some frequency. While more than one mechanism may be responsible for the energization, several observations indicate that there is a strong correlation between TAI and broadband low-frequency waves [23, 78]. A statistical study of observations by Freja indicated that TAI are most often associated with observations of boardband extremely low-frequency (BBELF) fluctuations in the auroral zone up to 1700 km [54]. Another statistical study of observation by FAST indicated that

99% of TAI are associated with BBELF fluctuations, at 84%, and electromagnetic ion cyclotron (EMIC) waves, at 15%, up to 4200 km [68].

A variety of homogeneous plasma instabilities have been suggested as the source for these broadband waves. Field-aligned current is often associated with TAI, which led to the suggestion of a current-driven electrostatic ion cyclotron (CDEIC) instability as a viable option [53]. It was subsequently shown that the observed field aligned currents are rarely above threshold for the instability [54]. Alfvén waves are also frequently observed with the broadband waves [105]. It has been suggested that these broadband fluctuations are Doppler-shifted inertial Alfvén waves [96]. It was later shown that this interpretation was only partially correct and that the observed fluctuations were non-propagating in the reference frame of the plasma [57].

The idea of the near-Earth plasma environment as being a largely homogeneous medium has been replaced due to observations of a variety of inhomogeneities at the smallest detectable scale lengths. Some examples of these observations are auroral arcs with thicknesses of 100 m [70, 18] and gradients in precipitating electron flux with scale lengths down to 10 m [15], localized electric fields of large magnitude in the polar magnetosphere [73, 74], and sheared plasma flows observed using radar backscatter techniques [86, 99]. Several theories for these broadband fluctuations have been proposed that utilize plasma inhomogeneity as the source of free energy. There are the shear assisted current driven electrostatic ion acoustic instability and the shear assisted current driven electrostatic ion cyclotron instability, where the current threshold can be substantially lowered due to the presence of parallel velocity shear [41]. The electrostatic inhomogeneous energy density driven (IEDD) instability [35], electromagnetic ion cyclotron modes [83], and electromagnetic modes in the subcyclotron regime [82] can all be driven by transverse velocity shear. The single tearing (ST) mode [90], double tearing (DT) mode, and current-advective shear-driven interchange (CASDI) mode [91] are magnetohydrodynamic modes driven by the transverse gradient in the field-aligned current. All of these modes are supported by space observations as viable theories for BBELF and the source of TAI, but there is no conclusive evidence for selecting one above the others.

Previous work at West Virginia University [61, 4] and the Naval Research Laboratory (NRL) [5] has experimentally verified the existence of the electrostatic IEDD instability, however, the absence of laboratory experiments exploring the characteristics of the other proposed shear-driven modes indicates a key dearth in our understanding of the physical processes of the space environment due to plasma inhomogeneities.

1.2 Space Observations

1.2.1 Ion Flows

The first ion outflow measurements were observations of a flux of precipitating keV O^+ ions in the auroral zone [92] and were later confirmed by observations of upflowing ions (UFI) above 5000 km by the S3-3 satellite. Two types of UFI were observed: ion beams, which are ion flows mostly parallel to the magnetic field, and ion conics, which are ion flows at an angle to the magnetic field [94]. There are in general two broad categories of ion outflows: bulk ion flows and energized ion flows. Bulk ion flows typically have energies of a few eV and have bulk flow velocities. An example of a bulk ion flow is the polar wind, which has thermal O^+ upflow in the topside auroral zone. Energized ion flows are characterized by much higher energies in the range from 10 eV to greater than 1 keV. In contrast to bulk ion flows, only a small fraction of the ions are energized. Examples of energized ion flows are upwelling ions, ion beams, and ion conics, including transversely accelerated ions.

The polar wind is the outflow of thermal ions near open magnetic field lines in the polar ionosphere resulting mainly from the ambipolar acceleration of ambient ions. The polar wind consisting of H^+ and He^+ ions was confirmed by thermal ion measurements on ISIS-2 [46], and Akebono observed the existence of O^+ polar wind [1]. It occurs essentially at all times and at all latitudes poleward of the plasmasphere and is characterized by energy less than a few eV and temperature of a fraction of an eV. The polar wind can be supersonic above 1500-2000 km and has a larger velocity on the dayside than on the nightside [110].

The auroral bulk upflow was first identified by the Alouette I sounding rocket [64]. It is a bulk ion upflow of thermal O^+ in the topside auroral ionosphere at altitudes from 400 km to 1500 km and is not caused by an auroral potential drop. The main heating mechanism is frictional heating and increased temperature at low altitudes results in an increased parallel pressure gradient, while new plasma is horizontally convected into the heating region [8]. In contrast to the polar wind the bulk of the ions in the flow do not reach escape velocity [66, 104], but do have enough energy to reach regions of higher ion energization at higher altitudes and consequently are an important source for other auroral energization mechanisms [34].

Energetic auroral ions are divided into two main types, ion beams and ion conics, which are distinguished by the angle of the flow relative to the magnetic field. Ion beams are upflowing ions that have a peak flux along the upward magnetic field direction. They are generally observed at altitudes above 5000 km with energies from 10 eV to a few keV. Ion conics have a peak flux at an angle with respect to the upward magnetic field direction. They are generally observed at altitudes from 1000 km [58, 109], out to several Earth radii [47, 22]. TAI have peak angles at or close to 90 degrees with respect to the magnetic field. They are typically located 400 km [109, 10], out to several Earth radii in the auroral zone [47, 9]. All major ion species are accelerated perpendicular to the ambient magnetic field to energies from a few eV to 1 keV. The ions are accelerated gradually over an extended altitude region appearing as ion conics of increasing energy and slowly decreasing cone angle [110]. This ion heating has been well correlated with observations of BBELF up to an altitude of at least 1700 km within the auroral ionosphere [7].

Upwelling ions have been observed at altitudes of 2000-5000 km and on the dayside are typically less energetic but have higher fluxes than transversely accelerated ions on the nightside. They have characteristic temperatures of a few eV and a parallel energy component, resulting in upward ion fluxes exceeding 10^{12} $\mathrm{m}^{-2}\mathrm{s}^{-1}$, where all observed ion species were heated [65].

1.2.2 Broadband Extra Low Frequency Fluctuations

Broadband extra low frequency (BBELF) fluctuations are a phenomenon frequently found in the topside auroral F region and at higher altitudes. The observed wave activity is several mV/m or larger fluctuating electric field with a power law spectrum extending from well below the local O$^+$ ion cyclotron frequency to well above the H$^+$ cyclotron frequency in the observer reference frame, essentially from a few Hz to a few kHz. No structure is observed at the cyclotron frequencies in the electric field power spectrum [54]. At frequencies below the O$^+$ cyclotron frequency, magnetic fluctuations are observed along with the electric fluctuations, and the magnetic fluctuations typically decrease faster with frequency than the electric field fluctuations [7, 44]. Measurements of the wavelength of BBELF fluctuations at higher frequencies using interferometric coherency have led to the conclusion that it is characterized by short wavelengths, in some cases on the order of the O$^+$ gyroradius [16, 55]. Rocket observations of BBELF fluctuations suggest that it is most commonly found just poleward of the region 1 currents. On the nightside this corresponds to the "Alfvénic" aurora or return current region [69]. On the prenoon dayside it corresponds to the region poleward of the convection reversal.

The importance of BBELF fluctuations is that they are the leading candidate responsible for transversely accelerated ions in the auroral ionosphere [7, 78, 59]. Figure 1.1 shows a segment of SCIFER sounding rocket data illustrating the correlation between transversely accelerated ions in the top panel and BBELF fluctuations in the middle panel, taken from Kintner *et. al* [54]. The fact that in some cases BBELF fluctuations are electromagnetic [102, 105], and in other cases are electrostatic [17] suggests that there may be more than one physical description for the observed broadband fluctuations [57].

Direct *in situ* observations of strongly sheared transverse plasma flows have frequently been associated with broadband low-frequency oscillations. For example, Kelley and Carlson [49] reported detection of intense velocity shear in association with large- and small-scale electrostatic waves near the edge of an auroral arc. The largest-amplitude waves were collocated with the strongest velocity shear (scale length 100 m). The long-wavelength waves were explained by the

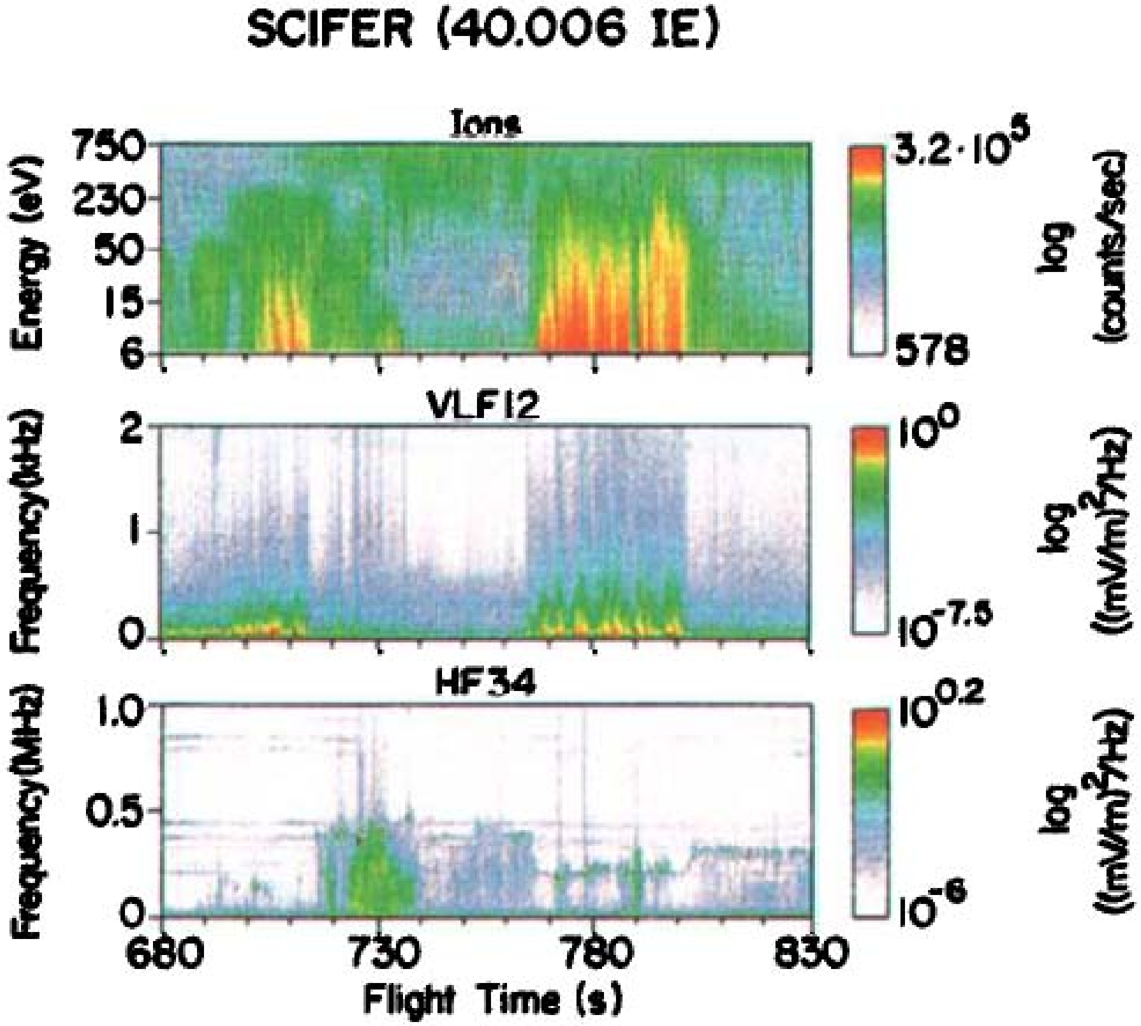

Figure 1.1: Segment of data from SCIFER sounding rocket illustrating the correlation between transversely heated ions (top panel) and BBELF fluctuations (middle panel). The lower panel shows higher frequency spectrum with Langmuir waves present. Reproduced from Kintner *et al.* [54].

Kelvin-Helmholtz instability, but a mechanism capable of explaining the observed small-scale irregularities was lacking. Kelly and Carlson [49] state that “A velocity shear mechanism operating at wavelengths short in comparison with the shear scale length, such as those observed here, would be of significant geophysical importance.” Earle *et al.* [31] also describe sounding rocket observations of broadband, low-frequency (10 Hz $<$ f $<$ 1000 Hz) electrostatic waves well correlated with highly transverse flows and magnetic field aligned current (FAC). While some of the spectra showed agreement with the spectrum that would be anticipated for CDEIC waves [53, 28, 30], other spectra implied a more important role for velocity shear.

A number of researchers have considered sheared plasma flow to be an important element in driving low-frequency broadband waves which can provide the necessary transverse ion heating. Clear indication of broadband fluctuations associated with large velocity shears, FAC (generally below the anticipated thresholds for current-driven instabilities), and upward flowing conic-shaped ion energy distributions in the auroral F region was found using DE 2 satellite observations [13]. The authors point out the consistency of their results with numerical simulations of small-scale turbulence generated by secondary instabilities growing on low-frequency primary waves [52] and discuss possible direct velocity shear influence on the growth of current-driven ion-cyclotron waves. Further evidence of the relationship between velocity shear and ion energization was provided by observations of thermal ion upwellings using HILAT satellite data from the dayside polar ionosphere [101]. It was found that shear in the transverse plasma velocity is common to most thermal ion upwelling observations. Tsunoda *et al.* [101] suggested that velocity shear provides a substantial portion of the free energy necessary for the initial heating and subsequent transport of ionospheric plasma up to magnetospheric altitudes. Indeed, upflowing oxygen ions contained within regions of sheared transverse plasma flow have been observed by the DE 2 satellite [67]. In addition, Kivanc and Heelis [56] have investigated the statistical relationship between horizontal velocity shears and vertical ion drifts in the high-latitude ionosphere using DE 2 data. Their results indicate that the vertical ion drift depends on the transverse shear when the bulk horizontal plasma drift is less than 1 km/s. For bulk horizontal flows exceeding 1 km/s, however, the data are more consistent with a scenario of Joule heating initiating the ion outflow.

1.3 Laboratory Experiments

Unambiguous *in situ* detection of small-scale, quasi-static structures is difficult, principally because temporal observations are made while the spacecraft is moving through the medium being diagnosed. Often, the question as to whether the observed structures are spatial or temporal arises. Consequently, application of theoretical models to the observations can become difficult. Laboratory experiments can provide crucial guidance in bridging the gap between theoretical models and the interpretation of *in situ* observations, especially when they are performed under carefully scaled conditions. With the distinct advantage of thorough diagnosis under controlled, reproducible conditions, laboratory experiments can be a very useful tool for uncovering important observational signatures, as well as helping to validate and refine theoretical models. This synergistic approach can lead to greater confidence in the interpretation of spacecraft data.

The effects of sheared flows on space plasmas, both parallel and transverse to a background magnetic field, have motivated a variety of laboratory experiments. Transverse shear in field aligned ion flow was first considered by D'Angelo using a fluid theory [26]. It was shown that an instability is triggered when the gradient in the drift exceeds a critical value for plasmas with $T_e = T_i$. The parallel velocity shear mechanism can be relevant to space plasmas with strong inhomogeneities in field-aligned flows like auroral arcs[18] and the polar cusps [27, 85]. In the laboratory these effects were studied by D'Angelo and von Goeler [29] in a double-ended Q machine. The experiments showed that sufficiently large shear could drive azimuthally propagating waves with frequencies near the ion cyclotron frequency. Willig *et al.* [108] reproduced many features of this "D'Angelo mode" and conclusively showed that the instability was driven by shear in the flow not the flow itself.

Similar to the transverse shear work of D'Angelo and von Goeler [29], Kent *et al.* [51] observed a wave localized to the region containing shear in the rotational velocity of the plasma that agreed well with Kelvin-Helmholtz (KH) theory. Jassby [48] conducted a detailed analysis of the KH instability, comparing theoretical results with measurements from a Q machine experiment in which the level of transverse shear could be controlled by an externally applied electric field. In a shear layer several ion gyroradii wide, Jassby observed azimuthally propagating, low-frequency KH waves and waves with frequency slightly higher than the ion cyclotron frequency with growth rates and amplitude smaller than the KH waves.

The generation of ion-cyclotron waves by strong potential structures was investigated in a double-ended Q machine by Nakamura *et al.* [89] and Sato *et al.* [87]. Two plasmas of different diameters and potentials were merged, creating a strong, three-dimensional double layer. Azimuthally propagating electrostatic waves with frequency above the ion cyclotron frequency were observed. Alport *et al.* [2] investigated strong, three-dimensional magnetized double layers in a weakly ionized argon discharge with a diverging magnetic field. Large-amplitude, narrow-band electrostatic waves with frequency corresponding to the ion cyclotron frequency and several harmonics were observed at the position of the parallel double layer. The waves were primarily radially propagating transverse to the axial magnetic field.

Velocity shear effects are believed to be important in space plasmas, particularly because small-scale transverse electric field structures are frequently being observed by high-resolution *in situ* diagnostics. The transverse, localized electric fields are often found in conjunction with field aligned current [57]. Ganguli *et al.* [35, 36, 37, 34] and Ganguli [33] have theoretically investigated the generalized plasma equilibrium which includes effects of velocity shear generated by localized transverse electric fields, density gradients, and field-aligned currents. This study has identified a new branch of plasma oscillation called the inhomogeneous energy-density-driven instability, which is sustained by shear-induced inhomogeneity in the wave energy density. Application of this model to space plasmas has been made by Gavrishchaka *et al.* [39, 43]. Depending on the local conditions, the oscillations can be in the ion cyclotron frequency range, causing the waves to be mistaken for the CDEIC instability especially when FAC is present. In contrast to the CDEIC instability, the IEDD waves are predicted to have a broadband, spiky spectral signature and to propagate predominantly in the $\mathbf{E} \times \mathbf{B}$ direction [37, 42, 77].

Laboratory investigation of the effects due to the combination of FAC and localized transverse electric fields were first performed at West Virginia University in a Q machine plasma. The relative contributions of these free-energy sources could be externally controlled using a segmented electrode consisting of an inner disk and an outer annulus [21]. The transverse dc electric fields were used to vary the magnitude of the $\mathbf{E} \times \mathbf{B}$ drift, which generated a radial shear in the azimuthal flow due to the electric field localization. Using this setup, Koepke *et al.* [61] and Amatucci [3], demonstrated that the character of electrostatic ion-cyclotron waves can change significantly when the effects of transverse shear are included. When weak electric fields were applied and sufficiently large parallel electron drift were applied, CDEIC waves were observed. As the velocity shear was increased, a distinct transition in the mode characteristics occurred. The wave amplitude became large, the spectrum became much broader, and the waves became spatially localized within the velocity-shear region and a transition to azimuthal propagation was observed. Most significantly, the experiments demonstrated that the threshold values of the FAC con be substantially reduced in the presence of velocity shear [3], in good agreement with theoretical predictions. By comparison with theoretical predictions, it was determined that these waves resulted from the resonant response of the IEDD instability [61, 4, 3, 60, 100].

In the case of strong shear, ion cyclotron waves can grow from a reactive response of the plasma to shear-induced inhomogeneity in wave energy density without the presence of field-aligned currents [35, 37]. This regime was investigated and verified by Amatucci *et al.* [5] in the Naval Research Laboratory's Space Physics Simulation Chamber (NRL SPSC). There was good agreement between the experimentally measured values of mode amplitude and the theoretically predicted IEDD instability growth rate. The wave propagation is primarily in the azimuthal direction, but the axial wave number increased with an increase in the electric field, implying that the waves become more oblique. These observational signatures of wave generation by transverse velocity shear have been invoked in conjunction with ground-based photometer measurements of rapid variations in the frequency of flickering aurora [71]. These results may also have relevance to the observations of BBELF by the SCIFER sounding rocket data where these waves were found in association with localized electric fields.

Measurements of perpendicular ion energization resulting from the shear-driven waves in collisionless conditions were made in the NRL SPSC [106, 6]. The ion temperature was observed to increase by a factor of two to four following the onset of the shear-driven waves. No increase in ion energy was detected in the presence of strong, but sub-threshold, transverse electric fields, establishing the waves as the source of ion heating. The IEDD instability maintains a large growth rate over a wide range of temperature ratios [35, 40]; it represents a more efficient source of ion heating than the CDEIC instability, which is self-limiting as T_i increases with respect to T_e [80].

In a set of papers [81, 82, 83], Peñano and Ganguli, derive a system of eigenvalue equations describing electromagnetic waves in a collisionless, magnetized plasma in the presence of a localized transverse inhomogeneous dc electric field. They numerically solve the resulting dispersion relation for typical conditions in the F region of the ionosphere in two regimes: very low frequencies and for frequencies near the ion cyclotron frequency. In the subcyclotron regime [82], the results were compared to those obtained from numerically solving the dispersion relation describing the electrostatic KH mode. Growth rates were compared as a function of the real part of the frequency normalized to the Alfvén frequency $\omega_A = k_z v_A$. The solution from the electromagnetic treatment could be accurately described by the electrostatic treatment for $\Re(\omega) >> \omega_A$. Both modes have a critical frequency below which they are stable, but the critical frequency from the electromagnetic treatment is lower, which indicates that there is a frequency range where the mode is purely electromagnetic. This suggests that this wave mode could have similar frequency spectrum to BBELF, the very low frequency electromagnetic components yielding to higher purely electrostatic fluctuations. In the ion cyclotron regime [83], it was shown that localized inhomogeneous transverse shear can drive instabilities near the ion cyclotron frequency. These waves have characteristics similar to observations of EMIC waves near the edges of auroral arcs.

Chapter 2

Theory

In a series of papers Ganguli *et al.* [35, 36, 38] investigated the effects of inhomogeneous transverse flows on the stability of a magnetized plasma. A kinetic, electrostatic dispersion relation describing ion cyclotron modes was first studied with the addition of an inhomogeneous transverse electric field. A top hat electric field, a uniform electric field in a central region and zero outside of that region, was employed to aid in understanding. Using negative energy wave considerations, it was shown that these sheared transverse flows can lead to an instability with the Doppler-shifted frequency resonant with the ion cyclotron frequency. In subsequent papers, the theory was extended to arbitrary flow profiles[36], cylindrical geometry[84], and electromagnetic instabilities[81, 82, 83].

We can gain a general understanding for this type of instability by comparing it to the two-stream instability where the negative energy wave concept is often used to explain it. Consider a plasma with no magnetic field where the ions are stationary and the electrons are drifting at a velocity v_0. The characteristic frequency for the electron and ion fluids are the electron and ion plasma frequency, respectively. If the electron plasma frequency can be Doppler-shifted near the ion plasma frequency, then an instability can grow.

The negative energy wave formalism can be described in physical terms as follows. If the time averaged energy density with the wave present is less than the time averaged energy density without the wave, then the wave is said to have negative energy, because it lowers the total energy of the system. In the system just described, the electron fluctuations can be shown to have negative energy, while the ion fluctuations have positive energy [24]. At any point in space, these two waves can grow at the expense of each other, which is an example of a local instability.

If we consider a uniform plasma with the magnetic field in the $\hat{z}$-direction and a uniform electric field in the $\hat{x}$-direction, the plasma will undergo a bulk plasma drift given by the $\mathbf{E} \times \mathbf{B}$ drift v_E. Since both species drift at the same velocity, we an transform to a frame moving at v_E, where it is clear that there is no free energy to drive an instability. For this reason, a non-uniform electric field is required for this instability.

In the presence of a non-uniform electric field, it is possible to have a region with negative energy and a region with positive energy. A wave packet can couple these two regions, allowing for the flow of energy from the negative energy region to the positive energy region leading to wave growth, which is an example of a non-local instability. The coupling of these two regions with differing energy densities resulted in it being called the inhomogeneous energy density driven instability.

In the first few sections of the chapter, we will seek a general understanding of the underlying physics of this instability. We will first examine the concept of negative energy waves following the derivation in Stix [97], and their use in determining plasma instability. Next, we will study the effects of applying a top hat electric field to the simplest system that supports ion cyclotron modes. With an understanding of this system, we will proceed to the electromagnetic theory.

2.1 Negative Energy Waves

We start from Poynting's Theorem in the standard differential form:

$$\nabla \cdot \left(\frac{1}{\mu_0} \mathbf{E} \times \mathbf{B} \right) = - \left[\frac{1}{\mu_0} \mathbf{B} \cdot \frac{\partial \mathbf{B}}{\partial t} + \mathbf{E} \cdot \left(\mathbf{J} + \epsilon_0 \frac{\partial \mathbf{E}}{\partial t} \right) \right]. \tag{2.1}$$

Using Ohm's Law $\mathbf{J} = \boldsymbol{\sigma} \cdot \mathbf{E}$ and noting that the conductivity tensor $\boldsymbol{\sigma}$ has no explicit time dependence, we can write the following,

$$\nabla \cdot \left(\frac{1}{\mu_0} \mathbf{E} \times \mathbf{B} \right) = - \left[\frac{1}{\mu_0} \mathbf{B} \cdot \frac{\partial \mathbf{B}}{\partial t} + \mathbf{E} \cdot \frac{\partial}{\partial t} \left(\{ \boldsymbol{\sigma} + \mathbf{I} \epsilon_0 \} \cdot \mathbf{E} \right) \right]. \tag{2.2}$$

Taking the expression in braces in the above equation to be the dielectric tensor $\boldsymbol{\epsilon}$, we can write:

$$\nabla \cdot \left(\frac{1}{\mu_0} \mathbf{E} \times \mathbf{B} \right) = - \left[\frac{1}{\mu_0} \mathbf{B} \cdot \frac{\partial \mathbf{B}}{\partial t} + \mathbf{E} \cdot \frac{\partial \mathbf{D}}{\partial t} \right], \tag{2.3}$$

where we have used that $\mathbf{D} = \boldsymbol{\epsilon} \cdot \mathbf{E}$ for the electric displacement. The left-hand side of Equation (2.3) represents the flux of electromagnetic energy and the right-hand side represents the rate of change of the energy density.

If we now look for plane wave solutions such that $\mathbf{E}$, $\mathbf{B}$, and $\mathbf{D}$ vary as the real part of $\mathbf{A}_1 \exp i \left(\mathbf{k} \cdot \mathbf{x} - \omega t \right)$, we can rewrite Poynting's Theorem in terms of time averaged harmonic fields. Absorbing the spatial fluctuations into the complex amplitude and allowing the frequency ω to be complex, we can write the real part of the harmonic fields as

$$\Re \left(\mathbf{A}_1 e^{-i\omega t} \right) = \frac{1}{2} \left[\mathbf{A}_1 e^{-i\omega t} + \mathbf{A}_1^* e^{-i\omega^* t} \right]. \tag{2.4}$$

Using these definitions, we start with the left-hand side of Equation (2.3):

$$\begin{aligned} \frac{1}{\mu_0} \nabla \cdot (\mathbf{E} \times \mathbf{B}) = \frac{1}{4\mu_0} \nabla \cdot \Big[& \left(\mathbf{E}_1 \times \mathbf{B}_1 \right) e^{-i2\omega t} + \left(\mathbf{E}_1 \times \mathbf{B}_1^* \right) e^{-i(\omega - \omega^*)t} \\ & + \left(\mathbf{E}_1^* \times \mathbf{B}_1 \right) e^{-i(\omega - \omega^*)t} + \left(\mathbf{E}_1^* \times \mathbf{B}_1^* \right) e^{i2\omega^* t} \Big]. \end{aligned} \tag{2.5}$$

Setting $\omega = \omega_r + i\omega_i$ explicitly and time averaging Equation (2.5) over one period, any oscillatory terms will time average to zero. The remaining growth terms will yield a phase factor after averaging, resulting in:

$$\nabla \cdot \langle \mathbf{S} \rangle = \frac{1}{4\mu_0} \nabla \cdot \left[\left(\mathbf{E}_1 \times \mathbf{B}_1^* \right) + \left(\mathbf{E}_1^* \times \mathbf{B}_1 \right) \right] e^{2\phi_i}. \tag{2.6}$$

Take the first term on the right-hand side of Equation (2.3) and apply the same procedure as above:

$$\begin{aligned}
-\frac{1}{\mu_0}\left\langle \mathbf{B}\cdot\frac{\partial \mathbf{B}}{\partial t}\right\rangle &= -\frac{1}{\mu_0}\left\langle \frac{1}{2}\left[\mathbf{B}_1 e^{-i\omega t}+\mathbf{B}_1^* e^{i\omega^* t}\right]\cdot\frac{\partial}{\partial t}\frac{1}{2}\left[\mathbf{B}_1 e^{-i\omega t}+\mathbf{B}_1^* e^{i\omega^* t}\right]\right\rangle \\
&= -\frac{1}{4\mu_0}\left\langle\left[\mathbf{B}_1 e^{-i\omega t}+\mathbf{B}_1^* e^{i\omega^* t}\right]\cdot\left[\left(-i\omega\right)\mathbf{B}_1 e^{-i\omega t}+\left(i\omega^*\right)\mathbf{B}_1^* e^{i\omega^* t}\right]\right\rangle \\
&= -\frac{1}{4\mu_0}\left[\left(i\omega_r+\omega_i\right)\mathbf{B}_1\cdot\mathbf{B}_1^*+\left(-i\omega_r+\omega_i\right)\mathbf{B}_1^*\cdot\mathbf{B}_1\right]e^{2\phi_i} \\
&= -\frac{\omega_i}{2\mu_0}\left|\mathbf{B}_1\right|^2 e^{2\phi_i}. \qquad (2.7)
\end{aligned}$$

The second term on the right-hand side of Equation (2.3) is a bit more complicated and will be carefully taken in parts. The electric displacement itself is assumed to be a plane wave oscillation, and the real part can be written as before as:

$$\Re\left(\mathbf{D}\right)=\frac{1}{2}\left[\boldsymbol{\epsilon}\cdot\mathbf{E}_1 e^{-i\omega t}+\left(\boldsymbol{\epsilon}\cdot\mathbf{E}_1\right)^* e^{i\omega^* t}\right]. \qquad (2.8)$$

The whole second term, using a similar procedure as above, can be written as:

$$\begin{aligned}
-\left\langle \mathbf{E}\cdot\frac{\partial \mathbf{D}}{\partial t}\right\rangle &= -\left\langle \frac{1}{2}\left[\mathbf{E}_1 e^{-i\omega t}+\mathbf{E}_1^* e^{i\omega^* t}\right]\cdot\frac{1}{2}\left[-i\omega\boldsymbol{\epsilon}\cdot\mathbf{E}_1 e^{-i\omega t}+i\omega^*\boldsymbol{\epsilon}^*\cdot\mathbf{E}_1^* e^{i\omega^* t}\right]\right\rangle \\
&= -\frac{1}{4}\left[i\omega^*\mathbf{E}_1\cdot\boldsymbol{\epsilon}^*\cdot\mathbf{E}_1^*-i\omega\mathbf{E}_{\mathbf{0}}^*\cdot\boldsymbol{\epsilon}\cdot\mathbf{E}_1\right]e^{2\phi_i}. \qquad (2.9)
\end{aligned}$$

In order to finish evaluating this term, we need to explore some tensor properties. Any tensor can be written as the sum of a hermitian tensor and an anti-hermitian tensor. If the adjoint or complex conjugate transpose of a tensor returns the same tensor, $\mathbf{H}^\dagger=\mathbf{H}$, then it is hermitian. If the adjoint of a tensor returns the negative of the original tensor, $\mathbf{A}^\dagger=-\mathbf{A}$, then it is anti-hermitian. We express a tensor $\mathbf{T}$ in terms of its hermitian and anti-hermitian parts:

$$\mathbf{T}=\mathbf{H}+\mathbf{A}, \qquad (2.10)$$

where the hermitian and antihermitian parts are defined as follows:

$$\mathbf{H} = \frac{1}{2}\left(\mathbf{T} + \mathbf{T}^{\dagger}\right) \tag{2.11a}$$

$$\mathbf{A} = \frac{1}{2}\left(\mathbf{T} - \mathbf{T}^{\dagger}\right). \tag{2.11b}$$

If we take the adjoint of the expressions in Equation (2.11), we can verify that the hermitian and anti-hermitian definitions are satisfied. The reason for using this property is to exploit the inherent symmetry of the above definitions. We will explore these symmetries in the following aside. If we explicitly separate the real and imaginary parts of a hermitian tensor $\mathbf{H} = \boldsymbol{\alpha} + i\boldsymbol{\beta}$ and an anti-hermitian tensor $\mathbf{A} = \boldsymbol{\gamma} + i\boldsymbol{\delta}$, where $\boldsymbol{\alpha}$, $\boldsymbol{\beta}$, $\boldsymbol{\gamma}$, and $\boldsymbol{\delta}$ have real components, we can write:

$$\begin{array}{cc} \mathbf{H}^{\dagger} = \mathbf{H} & \mathbf{A}^{\dagger} = -\mathbf{A} \\ (\boldsymbol{\alpha}_{ij} + i\boldsymbol{\beta}_{ij})^{\dagger} = \boldsymbol{\alpha}_{ji} - i\boldsymbol{\beta}_{ji} = \boldsymbol{\alpha}_{ij} + i\boldsymbol{\beta}_{ij} \qquad & (\boldsymbol{\gamma}_{ij} + i\boldsymbol{\delta}_{ij})^{\dagger} = \boldsymbol{\gamma}_{ji} - i\boldsymbol{\delta}_{ji} = -\boldsymbol{\gamma}_{ij} - i\boldsymbol{\delta}_{ij}. \end{array}$$

Equating the real and imaginary parts of each set, we have the following relations:

$$\begin{array}{ll} \boldsymbol{\alpha}_{ij} = \boldsymbol{\alpha}_{ji} \qquad & \boldsymbol{\gamma}_{ij} = -\boldsymbol{\gamma}_{ji} \\ \boldsymbol{\beta}_{ij} = -\boldsymbol{\beta}_{ji} \qquad & \boldsymbol{\delta}_{ij} = \boldsymbol{\delta}_{ji}. \end{array}$$

These four expressions tell us that the $\Re(\mathbf{H})$ and the $\Im(\mathbf{A})$ are symmetric, while the $\Im(\mathbf{H})$ and the $\Re(\mathbf{A})$ are anti-symmetric. These symmetries imply that the complex conjugate of a hermitian tensor is equivalent to its transpose, $\mathbf{H}^{*} = \mathbf{H}^{T}$, and that the complex conjugate of an anti-hermitian tensor is equivalent to the negative of its transpose, $\mathbf{A}^{*} = -\mathbf{A}^{T}$. Using these definitions, we can rewrite Equation (2.9) as the following:

$$-\left\langle \mathbf{E} \cdot \frac{\partial \mathbf{D}}{\partial t} \right\rangle = -\frac{1}{4}\left[i\omega^{*}\mathbf{E}_1 \cdot \left(\boldsymbol{\epsilon}_{\boldsymbol{H}}^{*} + \boldsymbol{\epsilon}_{\boldsymbol{A}}^{*}\right) \cdot \mathbf{E}_1^{*} - i\omega\mathbf{E}_1^{*} \cdot \left(\boldsymbol{\epsilon}_{\boldsymbol{H}} + \boldsymbol{\epsilon}_{\boldsymbol{A}}\right) \cdot \mathbf{E}_1\right] e^{2\phi_i}. \tag{2.12}$$

From the symmetry properties we can evaluate the following expressions:

$$\mathbf{E}_1 \cdot \boldsymbol{\epsilon}_H^* \cdot \mathbf{E}_1^* = \mathbf{E}_1 \cdot \boldsymbol{\epsilon}_H^T \cdot \mathbf{E}_1^* = \mathbf{E}_1^* \cdot \boldsymbol{\epsilon}_H \cdot \mathbf{E}_1 \tag{2.13}$$

$$\mathbf{E}_1 \cdot \boldsymbol{\epsilon}_A^* \cdot \mathbf{E}_1^* = \mathbf{E}_1 \cdot -\boldsymbol{\epsilon}_A^T \cdot \mathbf{E}_1^* = -\mathbf{E}_1^* \cdot \boldsymbol{\epsilon}_{\boldsymbol{A}} \cdot \mathbf{E}_1. \tag{2.14}$$

With these expressions, we can finish evaluating Equation (2.12):

$$\begin{aligned} -\left\langle \mathbf{E} \cdot \frac{\partial \mathbf{D}}{\partial t} \right\rangle &= -\frac{1}{4}\left[-i\left(\omega - \omega^*\right)\mathbf{E}_1^* \cdot \boldsymbol{\epsilon}_H \cdot \mathbf{E}_1 - i\left(\omega + \omega^*\right)\mathbf{E}_1^* \cdot \boldsymbol{\epsilon}_A \cdot \mathbf{E}_1\right] e^{2\phi_i} \\ &= -\frac{1}{2}\left[\omega_i \mathbf{E}_1^* \cdot \boldsymbol{\epsilon}_H \cdot \mathbf{E}_1 - i\omega_r \mathbf{E}_1^* \cdot \boldsymbol{\epsilon}_A \cdot \mathbf{E}_1\right] e^{2\phi_i}. \end{aligned} \tag{2.15}$$

Gathering all of the terms together from Equation (2.6), Equation (2.7), and Equation (2.15), we can write Poynting's theorem for harmonically varying fields as:

$$\begin{aligned} \frac{1}{\mu_0}\nabla \cdot \left[(\mathbf{E}_1 \times \mathbf{B}_1^*) + (\mathbf{E}_1^* \times \mathbf{B}_1)\right] = &-\Big[\frac{1}{\mu_0} 2\omega_i \mathbf{B}_1^* \cdot \mathbf{B}_1 + 2\omega_i \mathbf{E}_1^* \cdot \boldsymbol{\epsilon}_H \cdot \mathbf{E}_1 \\ &-2i\omega_r \mathbf{E}_1^* \cdot \boldsymbol{\epsilon}_A \cdot \mathbf{E}_1\Big]. \end{aligned} \tag{2.16}$$

If $\omega_i \ll \omega_r$, we can expand $\boldsymbol{\epsilon}$ in a Taylor series about the point $\omega = \omega_r$:

$$\begin{aligned} \boldsymbol{\epsilon}(\omega) &\approx \boldsymbol{\epsilon}(\omega_r) + (\omega - \omega_r)\left.\frac{\partial \boldsymbol{\epsilon}}{\partial \omega}\right|_{\omega=\omega_r} + \dots \\ &\approx \boldsymbol{\epsilon}(\omega_r) + i\omega_i \left.\frac{\partial \boldsymbol{\epsilon}}{\partial \omega}\right|_{\omega=\omega_r} + \dots \end{aligned} \tag{2.17}$$

Substituting this result into the definition for an anti-hermitian tensor given in Equation (2.11b), we can write the following expression:

$$\begin{aligned} \boldsymbol{\epsilon}_A &\approx \frac{1}{2}\left(\boldsymbol{\epsilon} + i\omega_i \frac{\partial \boldsymbol{\epsilon}}{\partial \omega} - \boldsymbol{\epsilon}^\dagger + i\omega_i \frac{\partial \boldsymbol{\epsilon}^\dagger}{\partial \omega}\right) + \dots \\ &\approx \boldsymbol{\epsilon}_A + i\omega_i \frac{\partial \boldsymbol{\epsilon}_H}{\partial \omega} \end{aligned} \tag{2.18}$$

This expression can be substituted into the last term in Equation (2.16):

$$\nabla \cdot \mathbf{S} = -\left[\frac{1}{\mu_0} 2\omega_i \mathbf{B}_1^* \cdot \mathbf{B}_1 + 2\omega_i \mathbf{E}_1^* \cdot \left(\frac{\partial}{\partial \omega}\left[\omega \boldsymbol{\epsilon}_H\right]\right) \cdot \mathbf{E}_1 + \omega_r \mathbf{E}_1^* \cdot \boldsymbol{\epsilon}_A \cdot \mathbf{E}_1\right], \tag{2.19}$$

where $\mathbf{S} = \frac{1}{\mu_0}\left[(\mathbf{E}_1 \times \mathbf{B}_1^*) + (\mathbf{E}_1^* \times \mathbf{B}_1)\right]$ is the Poynting vector. The first term on the right hand side of Equation (2.19) is the typical energy density in the wave magnetic field, while the second term is an effective energy density in the wave electric field, however, it represents the sum of the electrostatic energy density and the contribution of the charged-particle kinetic energy due to the coherent wave motion. The last term on the right hand side represents the dissipation or absorption of energy by the dielectric medium.

We can write the time averaged effective energy density for an electrostatic wave as

$$W_{eff} = \frac{1}{4}\left|\Phi_1\right|^2 \mathbf{k} \cdot \left(\frac{\partial}{\partial \omega}\left[\omega \boldsymbol{\epsilon}_H\right]\right) \cdot \mathbf{k}, \tag{2.20}$$

where Φ_1 is the wave electrostatic potential. The sign of the effective electric wave energy density is determined by $\frac{\partial}{\partial \omega}\left[\omega \boldsymbol{\epsilon}_H\right]$. If this term is negative, the total energy of the system in a time averaged sense has been lowered due to the presence of the wave. It is energetically favorable for the wave to grow. This establishes a necessary but not sufficient criterion for instability, where

$$\frac{\partial}{\partial \omega}\left[\omega \boldsymbol{\epsilon}_H\right] < 0. \tag{2.21}$$

Nezlin [76] provides a good example of the use of this methodology in applying it to the plasma beam driven instability.

2.2 Electrostatic Example

In this section we use the simplest plasma model that supports ion cyclotron waves. We treat the ions as a cold fluid and the electrons using the Boltzmann relation, and we add an arbitrary electric field profile in the $\hat{x}$-direction. We assume electrostatic waves with a propagation angle almost perpendicular to B_0. As discussed in Chen [24], it is beneficial to make the propagation small enough such that the $\nabla = ik\hat{y}$ for the ions, but large enough that the electrons can carry out Debye shielding.

2.2.1 Model Description

Ion dynamics can be descibed by the cold fluid equations:

$$\begin{aligned} \frac{\partial n_i}{\partial t} + \nabla \cdot (n_i \mathbf{v}_i) &= 0 && (2.22) \\ \left(\frac{\partial}{\partial t} + \mathbf{v}_i \cdot \nabla\right) \mathbf{v}_i &= \frac{e}{m_i} \left(\mathbf{E} + \mathbf{v}_i \times \mathbf{B}\right), && (2.23) \end{aligned}$$

where m_i is the ion mass, e is the charge of an electron, n_i is the ion density, and $\mathbf{v}_i$ is the ion fluid velocity. We are considering only electrostatic modes, and we linearize the above equations by assuming the following forms:

$$\begin{aligned} \mathbf{B} &= B_0 \hat{z} \\ \mathbf{E} &= E_0(x)\hat{x} - \nabla\left(\phi_1(x) e^{i(ky-\omega t)}\right) \\ \mathbf{v}_i &= v_{1x}(x) e^{i(ky-\omega t)} \hat{x} + \left(v_0(x) + v_{1y}(x) e^{i(ky-\omega t)}\right) \hat{y} \\ n_i &= n_{i0} + n_{i1}(x) e^{i(ky-\omega t)} \end{aligned}$$

The 0 and 1 subscripts refer to the equilibrium and perturbed values for each quantity, respectively. The equilibrium velocity is given simply by the $\mathbf{E} \times \mathbf{B}$ velocity, $\mathbf{v}_0\left(x\right) \equiv v_E = -E_0/B_0\hat{y}$.

Let us now turn our attention to the fluctuating quantities. Linearizing Equation (2.23) leads to two coupled equations for the fluctuating velocities in the x and y directions

$$\begin{aligned} -i\omega_1 v_{1x} &= -\frac{e}{m_i}\frac{\partial \phi_1}{\partial x} + \Omega_{ci} v_{1y} \\ -i\omega_1 v_{1y} &= -ik\frac{e}{m_i}\phi_1 - \eta \Omega_{ci} v_{1x}, \end{aligned}$$

where $\omega_1 = \omega - kv_E$ and $\eta = 1 + \frac{1}{\Omega_{ci}} \frac{\partial v_E}{\partial x}$. Solving these equations yields the following expressions for the fluctuating velocity components in terms of the wave potential

$$v_{1x} = -\frac{ie}{m_i D}\left(\omega_1 \frac{\partial \phi_1}{\partial x} - k\Omega_{ci}\phi_1\right) \tag{2.24}$$

$$v_{1y} = -\frac{e}{m_i D}\left(\eta\Omega_{ci} \frac{\partial \phi_1}{\partial x} - k\omega_1\phi_1\right), \tag{2.25}$$

where $D = \omega_1^2 - \eta\Omega_{ci}^2$. Keeping only the first order terms in Equation (2.22), we are left with the following expression for the ion density fluctuations

$$n_{i1} = \frac{n_0}{i\omega_1}\left(\frac{\partial v_{1x}}{\partial x} + ikv_{1y}\right). \tag{2.26}$$

Assuming Boltzmann electrons yields the following expression for the electron density fluctuations with temperature T_e

$$n_{e1} = n_0 \frac{e\phi_1}{T_e}. \tag{2.27}$$

Using the plasma approximation of quasi-neutrality, $n_{i1} \approx n_{e1}$ we can derive the following differential equation for the wave potential

$$D\frac{\partial}{\partial x}\left(\frac{1}{D}\frac{\partial \phi_1}{\partial x}\right) + \left(\frac{m_i}{m_e}\frac{D}{v_{te}^2} + \frac{k\Omega_{ci}}{\omega_1}\frac{1}{D}\frac{\partial D}{\partial x} - k^2\right)\phi_1 = 0, \tag{2.28}$$

where $v_{te} = \sqrt{T_e/m_e}$ is the electron thermal velocity. If we assume the following form for the background electric field,

$$\mathbf{E}(x) = \begin{cases} E_0, \text{ for } |x| \leq L \\ 0, \text{ for } |x| > L, \end{cases} \tag{2.29}$$

we can divide the space into two regions, where within each region, $\frac{\partial v_E}{\partial x} = 0$, $\eta = 1$, $D = \omega_1^2 - \Omega_{ci}^2$, and $\frac{\partial D}{\partial x} = 0$. With these simplifications $\omega_1 = \omega - kv_E$ in Region (i), where $|x| \leq L$ and $\omega_1 = \omega$ in

Region (ii), where $|x| > L$ and leads to the following differential equations

$$\frac{\partial^2 \phi_i}{\partial x^2} = -\kappa_i^2 \phi_i \tag{2.30}$$

$$\frac{\partial^2 \phi_{ii}}{\partial x^2} = -\kappa_{ii}^2 \phi_{ii}, \tag{2.31}$$

where ϕ_i and ϕ_{ii} are the wave potential in Region (i) and (ii) respectively and

$$\kappa_i^2 = \frac{m_i}{m_e} \frac{\omega_1^2 - \Omega_{ci}^2}{v_{te}^2} - k^2 \tag{2.32}$$

$$\kappa_{ii}^2 = \frac{m_i}{m_e} \frac{\omega^2 - \Omega_{ci}^2}{v_{te}^2} - k^2. \tag{2.33}$$

The even solutions to these differential equations can be written as

$$\phi_i(x) = A \cos(\kappa_i x) \tag{2.34}$$

$$\phi_{ii}(x) = B \exp(i\kappa_{ii} x + i\delta), \tag{2.35}$$

where A, B, and δ are constants. By requiring that these solutions and their derivatives be continuous across the boundary, $x = L$, we arrive at the following transcendental equation for the real and imaginary parts of ω:

$$-\kappa_i \tan(\kappa_i L) = i\kappa_{ii}. \tag{2.36}$$

2.2.2 Analysis

If Equations (2.32) and (2.33) are rearranged, we can see the effects of imposing the top-hat electric field.

$$\omega_1^2 - \Omega_{ci}^2 - \left(\kappa_i^2 + k^2\right) v_s^2 = 0 \tag{2.37}$$

$$\omega^2 - \Omega_{ci}^2 - \left(\kappa_{ii}^2 + k^2\right) v_s^2 = 0 \tag{2.38}$$

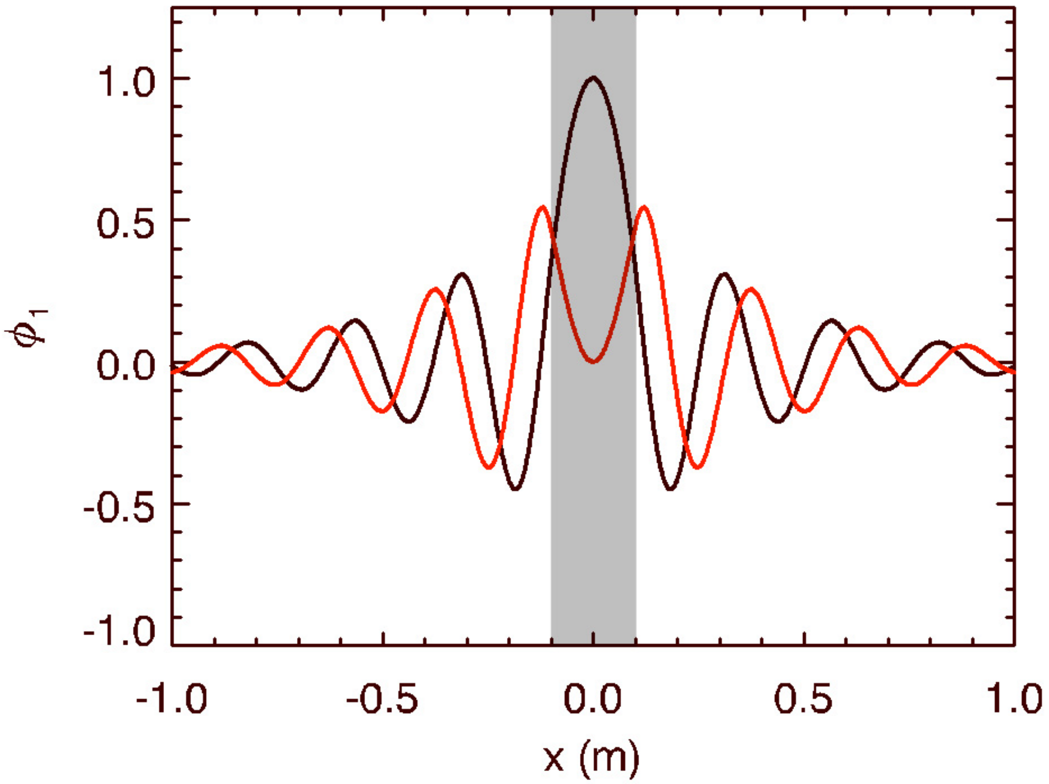

Figure 2.1: Real (black) and imaginary (red) parts of the radial eigenfunction for the wave potential, using $L = 0.1$ m, $E_0 = -600$ V/m, and $k = 9.2$ m^{-1}. This value of k yields the maximum growth rate for the lowest order mode for the given parameters. The associated eigenvalue is $\omega = 1.4\,\Omega_{ci}$ and $\gamma = 0.07\,\Omega_{ci}$. The shaded region indicates the location of the flow layer.

These dispersion relations are those from the fluid model that we have chosen with the addition of an effective k_x given by κ_i and κ_{ii} in the two regions. By applying the top-hat electric field, we have imposed a spatial scale on the plasma and must include a wave vector in the $\hat{x}$-direction in the dispersion relation.

Equation (2.36) can be solved numerically using a root finder to determine the complex ω that will satisfy the matching conditions at the boundary. The plasma parameters that we use to solve the equation are as follows: density $n_0 = 10^{16}$ m^{-3}, electron temperature $T_e = 3.0$ eV, background magnetic field $B_0 = 0.03$ T, and the ion species is singly ionized Argon. If we take $L = 0.1$ m and the electric field $E_0 = -600$ V/m, we find unstable solutions with the maximum growth

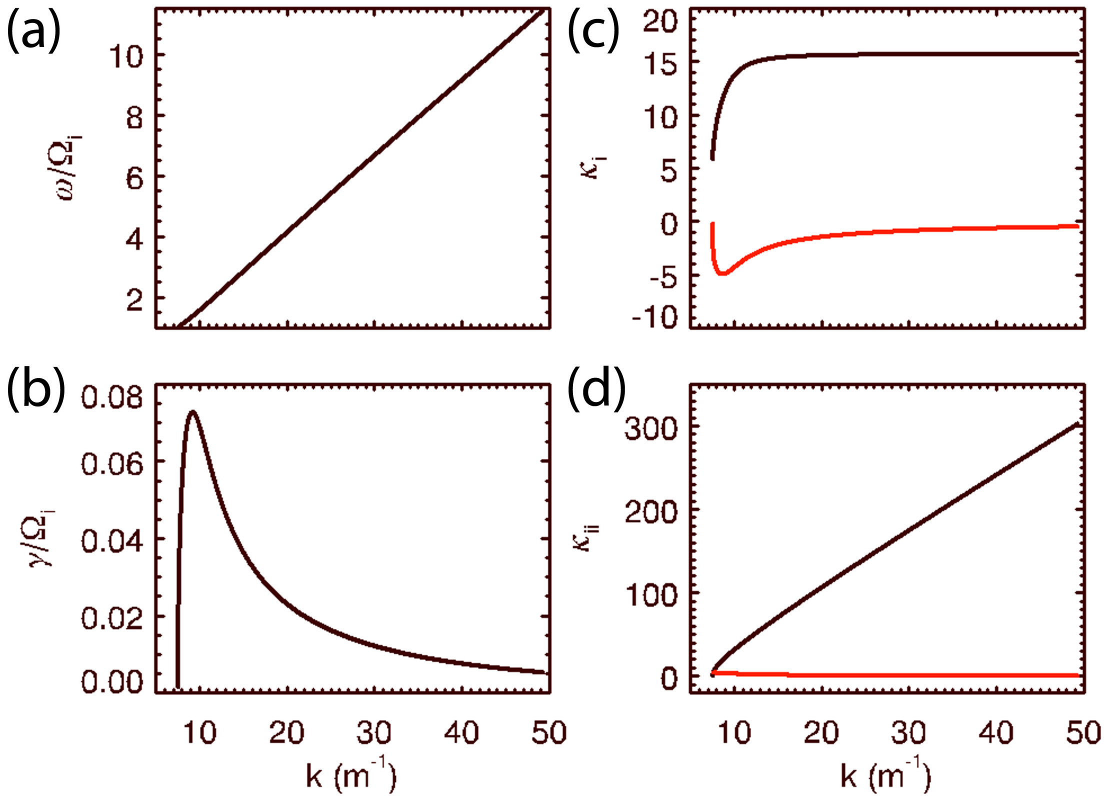

Figure 2.2: Normalized real frequency (a), real (black) and imaginary (red) parts of κ_i (b), normalized growth rate (c), and real (black) and imaginary (red) parts of κ_{ii} (d) as functions of k for the same conditions as above.

rate at $k = 9.2\ \mathrm{m}^{-1}$ and with eigenvalue $\omega = 1.4\ \Omega_{ci}$ and $\gamma = 0.07\ \Omega_{ci}$. Figure (2.1) shows the real (black) and imaginary (red) parts of this radial eigenfunction for the wave potential for the lowest order mode. This typical eigenfunction is in agreement with the eigenfunctions reported by Ganguli et al [38].

Figure (2.2) (b) shows the growth rate normalized to the ion cyclotron frequency as a function of k for the parameters given above for the lowest order mode. There are two regions where the growth rate goes to zero. The cutoff at large k is a geometric effect that can be seen from the form of Equation (2.36). When γ goes to zero, κ_i becomes purely real and κ_{ii} becomes purely imaginary. This makes Equation (2.36) purely real. Under these conditions the left-hand-side of

Equation (2.36), has periodic singularities. The first of which occurs when $\kappa_i L = \pi/2$. This effectively sets a limit on the smallest perpendicular wavelength for the instability.

The cutoff at small k gives the flow threshold for the instability. This can be seen by applying the negative energy wave formalism to this analysis. We can calculate the effective wave energy density using the expression from Equation (2.20) and the dielectric constant that is given by the left-hand side of Equation (2.37). In order for the system to be unstable, the negative energy wave formalism requires that $\langle W_{eff} \rangle < 0$, and this sign is determined by

$$\omega \frac{\partial \boldsymbol{\epsilon}}{\partial \omega} = 2\omega\omega_1. \tag{2.39}$$

The energy density can become negative if $\omega_1 < 0$, which implies that $kv_E > \omega$. This imposes a necessary condition for instability, however, it is not sufficient as will be shown below.

The first bit of information we will need is an expression for the real and imaginary parts of the square root of a complex number. If $z^2 = \alpha + i\beta$, where α and β are both real, we write an expression for z, by writing z^2 in terms of magnitude and phase. The magnitude is given by $r = \sqrt{\alpha^2 + \beta^2}$, and the phase is $\theta = \arctan(\beta/\alpha)$. The real and imaginary parts of z are $z_R = \sqrt{r}\cos(\theta/2)$ and $z_I = \sqrt{r}\sin(\theta/2)$. We take Equations (2.32-2.33), and explicitly substitute $\omega = \omega_r + i\gamma$.

$$\begin{aligned}
\kappa_i^2 &= \alpha_i + i\beta_i & \qquad \kappa_{ii} &= \alpha_{ii} + i\beta_{ii} \\
\alpha_i &= \frac{\omega_{1r}^2 - \gamma^2 - \Omega_{ci}^2}{v_s^2} - k^2 & \qquad \alpha_{ii} &= \frac{\omega_r^2 - \gamma^2\Omega_{ci}^2}{v_s^2} - k^2 \\
\beta_i &= \frac{2\gamma\omega_{1r}}{v_s^2} & \qquad \beta_{ii} &= \frac{2\gamma\omega}{v_s^2},
\end{aligned}$$

where $\omega_{1r} = \omega_r - kv_E$. From Figure (2.2) (c), we can see that as γ goes to zero as we lower k, the real part of κ_i is positive and the imaginary part of $\kappa_i \to 0^-$. This implies that θ_i must be negative, which requires α_i and β_i to have opposite signs. From the negative energy analysis we know that $\omega_{1r} < 0$ and $\gamma > 0$, we know that $\beta_i < 0$. This means that $\alpha_i > 0$, which gives us the following expression:

$$
\begin{aligned}
\omega_{1r}^2 > &\quad \Omega_{ci}^2 + k^2 v_s^2 \\
\Rightarrow \omega_{1r} > &\quad \left|\sqrt{\Omega_{ci}^2 + k^2 v_s^2}\right|,
\end{aligned}
$$

where we have used that at threshold γ goes to zero. Again using that ω_{1r} must be negative, we keep only the negative root.

$$
\begin{aligned}
\omega_{1r} < &\quad -\sqrt{\Omega_{ci}^2 + k^2 v_s^2} \\
\Rightarrow k v_E > &\quad \omega_r + \sqrt{\Omega_{ci}^2 + k^2 v_s^2}
\end{aligned}
\tag{2.40}
$$

In turn, we can see from Figure (2.2) (d), that the real part of $\kappa_{ii} \to 0^+$ and the imaginary part of $\kappa_{ii} > 0$ as γ goes to zero as we lower k. These two conditions imply that $\theta_{ii} > 0$, which requires that α_{ii} and β_{ii} have the same sign. Since by construction $\omega > 0$ and $\gamma > 0$, then β_{ii} must be positive. This implies that $\alpha_{ii} > 0$, which allows us to write the following expression for ω_r as we let $\gamma \to 0$:

$$\omega_r > \sqrt{\Omega_{ci}^2 + k^2 v_s^2}. \tag{2.41}$$

Substituting this result into Equation (2.40), we can write the threshold condition for this instability:

$$k v_E > 2\sqrt{\Omega_{ci}^2 + k^2 v_s^2}. \tag{2.42}$$

This threshold condition ensures that the wave energy density is negative in the region with the flow and that ω_1 can satisfy Equation (2.37).

We can use the unstable solution plotted in Figure 2.1 and Equations (2.24-2.26) to calculate the oscillating velocity and density of the fluid as functions of space and time. With these quantities, we can construct the time averaged energy density and see how this wave is indeed a negative energy wave.

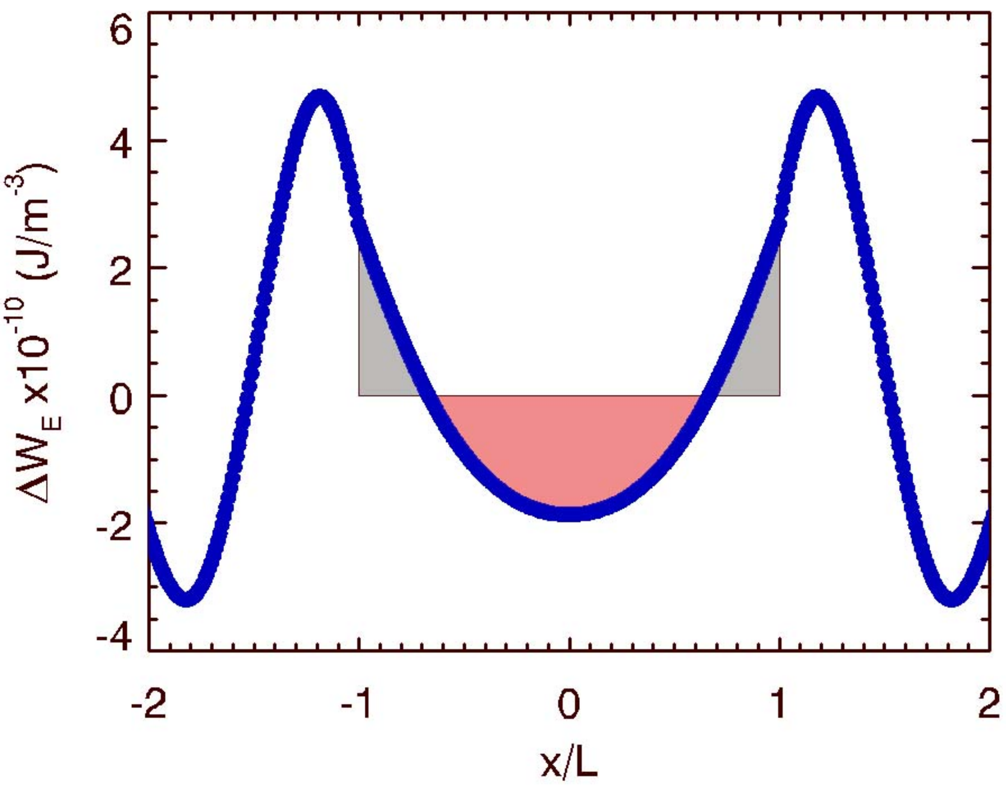

Figure 2.3: The time averaged change in the energy density stored in the electric field. The wave acts to reduce the applied background electric field.

We first calculate the change in the energy density stored in the electric field:

$$\Delta W_E = \left\langle \frac{1}{2}\epsilon_0 \left|\mathbf{E}_0 + \mathbf{E}_1\right|^2 \right\rangle - \frac{1}{2}\epsilon_0 \left|\mathbf{E}_0\right|^2 , \tag{2.43}$$

where $<>$ denotes a time average, $\mathbf{E}_0$ is the background electric field, and $\mathbf{E}_1 = -\nabla\phi_1$ is the wave electric field. The resulting change in the energy density stored in the electric field as a function of the normalized position in the $\hat{x}$-direction is plotted in Figure 2.3. As can be seen, the wave acts to reduce the electric field in the top hat region, which is consistent with the simulations of *Palmadesso et al.* [79].

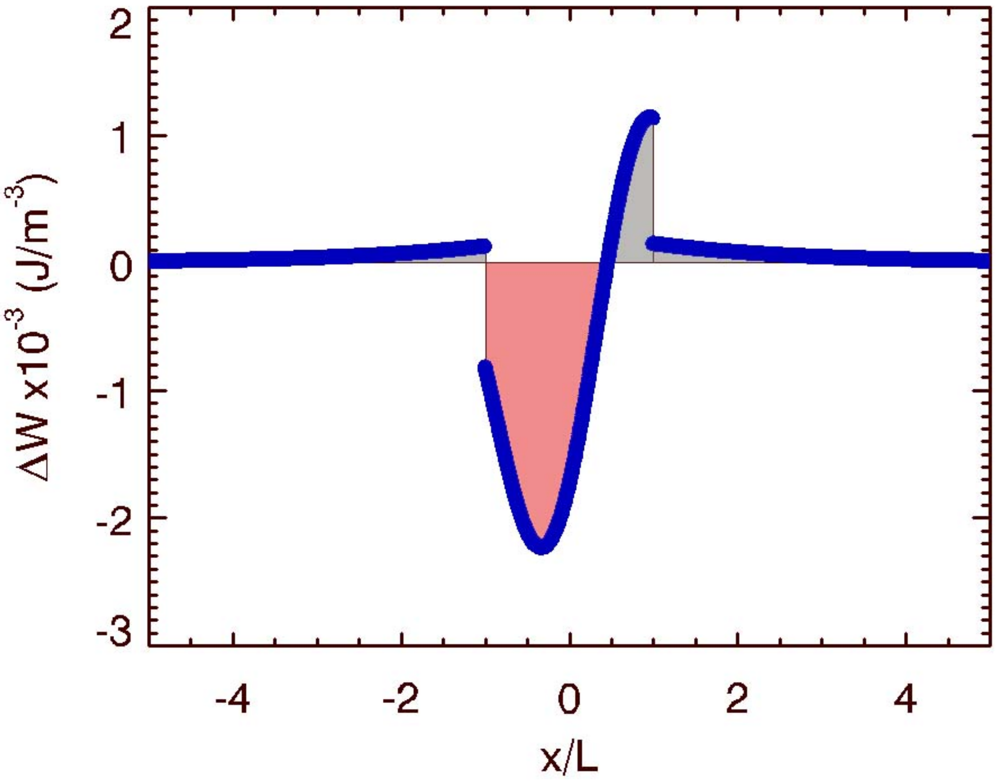

Figure 2.4: The time averaged change in the energy density of the whole system. The waves acts to lower the energy density of the system.

We can also look at the change in energy density of the system due to the instability:

$$\Delta W = \left\langle \frac{1}{2} m_i \left(n_0 + n_1\right) \left|\mathbf{v}_0 + \mathbf{v}_1\right|^2 \right\rangle - \frac{1}{2} m_i n_0 \left|\mathbf{v}_0\right|^2 + \Delta W_E, \tag{2.44}$$

where we have used ΔW_E from Equation (2.43). The resulting change in the energy density for the system as a function of the normalized position in the $\hat{x}$-direction is plotted in Figure 2.4. As expected, the total energy of the system is lowered due to the presence of the wave. This is due to the fact that the ion density fluctuations and the ion velocity fluctuations are out of phase. Over a wave period, the kinetic energy of the particles is less than at equilibrium. The wave acts to lower the energy density of the system. It is energetically favorable for the wave to grow.

2.3 Electromagnetic Model

In this section we present the Peñano and Ganguli [81] non-local, collisionless model for electromagnetic waves in the presence of an inhomogeneous electric field transverse to the background magnetic field. What follows is an outline of the derivation, however, a thorough treatment can be found in Appendix A. A Cartesian coordinate system is used with the background magnetic field along the z axis, such that $\mathbf{B}_0 = B_0\hat{z}$. The nonuniform DC electric field is in the x direction, $\mathbf{E}_0 = E_0(x)\hat{x}$. This leads to an equilibrium $\mathbf{E} \times \mathbf{B}$ drift along the y axis, $v_E = -E_0/B_0$. We assume perturbations of the form:

$$\tilde{A} = A_1(x)\exp\left[i\left(k_y y + k_z z - \omega t\right)\right], \tag{2.45}$$

where k_y and k_z are real wave vector components, $A_1(x)$ is the complex amplitude, and ω is the complex frequency.

The ions and the motion of the electrons perpendicular to the background magnetic field are treated as cold fluids. We can express the perturbed perpendicular current density as

$$\mathbf{J}_{1\perp} = \rho_1 v_E + \sum_{\alpha} q_\alpha n_{0\alpha}\mathbf{v}_{1\perp\alpha}, \tag{2.46}$$

where the subscript α denotes the plasma species, q is the charge, n is the density, $v_\perp$ is the perpendicular fluid velocity components. The perturbed charge density ρ_1 is determined from the linearized continuity equation:

$$i\omega\rho_1 = \frac{\partial J_{1x}}{\partial x} + ik_y J_{1y} + ik_z J_{1z}. \tag{2.47}$$

The perturbed ion velocities and the perpendicular components of the perturbed electron velocities are determined from the linearized momentum equation in terms of the perturbed electric field components. We construct the perpendicular current density and the ion contribution to the parallel current density by substituting into Equation (2.46):

$$
\begin{aligned}
J_{1x} =& - i\omega\epsilon_0 \sum_\alpha \frac{\omega_{p\alpha}^2}{\omega^2\Omega_\alpha^2 D_\alpha}\left(\omega_1^2 E_{1x} + i\omega\Omega_\alpha E_{1y} - i\omega_1 v_E \frac{\partial E_{1y}}{\partial x}\right) && (2.48)\\
J_{1y} =& \rho_1 v_E - i\omega\epsilon_0 \sum_\alpha \frac{\omega_{p\alpha}^2}{\omega^2\Omega_\alpha^2 D_\alpha}\left(\omega\omega_1 E_{1y} - \Omega_\alpha\eta_\alpha v_E \frac{\partial E_{1y}}{\partial x} - i\Omega_\alpha\eta_\alpha\omega_1 E_{1x}\right) && (2.49)\\
J_{i1z} =& i\omega\epsilon_0 \left(\frac{\omega_{pi}^2}{\omega}\right)\left(E_{1z} + \frac{k_z v_E}{\omega_1} E_{1y}\right), && (2.50)
\end{aligned}
$$

where $D_\alpha = \eta_\alpha - \omega_1^2/\Omega_\alpha^2$, $\eta_\alpha = 1 + v_E'/\Omega_\alpha$, $\omega_1 = \omega - k_y v_E$, $\omega_{p\alpha}^2 = e^2 n_0/(\epsilon_0 m_\alpha)$ is the plasma frequency, and $\Omega_\alpha = q_\alpha B_0/m_\alpha$ is the signed cyclotron frequency. For consistency with assumptions made when calculating the kinetic electron response, we assume that $|v_E'/\Omega_e| \ll 1$ and set $\eta_e = 1$.

The parallel motion of the electrons is treated kinetically in order to retain electron Landau damping effects. The lowest order contribution to the perturbed parallel electron current density is determined by first assuming that the scale lengths of the background electric field is much larger than the electron gyroradius ($L_E \ll \rho_e$), the wave frequency is much smaller than the electron cyclotron frequency ($\omega \ll |\Omega_e|$), and the transverse wavelength is much bigger than the electron gyroradius ($k_\perp \rho_e \ll 1$). With these assumption we can write the parallel electron current density as

$$
J_{e1z} = i\omega\epsilon_0 \left(\frac{\omega_{pe}^2}{\omega^2}\right)\zeta_e^2 Z'(\zeta_e)\left(E_{1z} + \frac{k_z v_E}{\omega_1}E_{1y}\right), \tag{2.51}
$$

where $\zeta_e = \omega_1/\left(\sqrt{2}k_z v_{te}\right)$, $v_{te} = \sqrt{T_e/m_e}$, and Z' is the derivative of the plasma dispersion function with respect to its argument.

The perturbed current density is substituted in to the wave equation and the following matrix equation is obtained:

$$
\begin{pmatrix}
C_{11} & B_{12}\frac{\partial}{\partial x} + C_{12} & B_{13}\frac{\partial}{\partial x} \\
\frac{\partial B_{12}}{\partial x} + B_{12}\frac{\partial}{\partial x} - C_{12} & \frac{\partial A_{22}}{\partial x}\frac{\partial}{\partial x} + A_{22}\frac{\partial^2}{\partial x^2} + C_{22} & C_{23} \\
\frac{\partial B_{13}}{\partial x} + B_{13}\frac{\partial}{\partial x} & C_{23} & A_{33}\frac{\partial^2}{\partial x^2} + C_{33}
\end{pmatrix}
\begin{pmatrix} E_{1x} \\ E_{1y} \\ E_{1z} \end{pmatrix} = 0. \tag{2.52}
$$

The individual matrix elements used above are given below.

$$A_{22} = \frac{c^2}{\omega^2} - \sum_\alpha \frac{\omega_{p\alpha}^2}{\omega^2} \frac{v_E^2}{\Omega_\alpha^2 D_\alpha} \tag{2.53}$$

$$A_{33} = \frac{c^2}{\omega^2} \tag{2.54}$$

$$B_{12} = -i \left[\frac{k_y c^2}{\omega^2} + \sum_\alpha \frac{\omega_{p\alpha}^2}{\omega^2} \frac{\omega_1 v_E}{\Omega_\alpha^2 D_\alpha} \right] \tag{2.55}$$

$$B_{13} = -i \frac{k_z c^2}{\omega^2} \tag{2.56}$$

$$C_{11} = 1 - \frac{k_y^2 c^2}{\omega^2} - \frac{k_z^2 c^2}{\omega^2} + \sum_\alpha \frac{\omega_{p\alpha}^2}{\omega^2} \frac{\omega_1^2}{\Omega_\alpha^2 D_\alpha} \tag{2.57}$$

$$C_{12} = -C_{21} = i \sum_\alpha \frac{\omega_{p\alpha}^2}{\omega^2} \frac{\omega}{\Omega_\alpha D_\alpha} \tag{2.58}$$

$$\begin{aligned} C_{22} =& 1 - \frac{k_z^2 c^2}{\omega^2} - \sum_\alpha \frac{\omega_{p\alpha}^2}{\Omega_\alpha^2 D_\alpha} \left(\frac{\Omega_\alpha}{\omega_1^2} \frac{\partial v_E}{\partial x} - 1 \right) \\ &+ \frac{k_z^2 v_E^2}{\omega_1^2} (P-1) + \frac{\partial}{\partial x} \left[\sum_\alpha \frac{\omega_{p\alpha}^2}{\omega^2} \left(\frac{\omega v_E}{\omega_1 \Omega_\alpha D_\alpha} \right) \right] \end{aligned} \tag{2.59}$$

$$C_{23} = C_{32} = \frac{k_y k_z c^2}{\omega^2} + \frac{k_z v_E}{\omega_1} (P-1) \tag{2.60}$$

$$C_{33} = P - \frac{k_y^2 c^2}{\omega^2} \tag{2.61}$$

The above system of eigenvalue equations can be solved numerically for the perturbed electric field profiles and the eigenvalue ω. It describes all cold plasma normal modes in the presence of transverse velocity shear. The inhomogeneous electric field introduces a variety of modifications to the dispersion of the waves [82]. A nonuniform Doppler shift is introduced that cannot be transformed away, which implies that the Doppler-shifted frequency controls the resonance properties. In addition, the cyclotron frequency is modified by the presence of the sheared flows. The effective cyclotron frequency $\Omega'_\alpha \to \sqrt{\eta_\alpha \Omega_\alpha}$. This can be seen from the factor $\Omega_\alpha^2 D_\alpha = \eta_\alpha \Omega_\alpha - \omega_1^2$, which is the cyclotron resonance.

2.4 Electromagnetic Top Hat

Since there are no spatial derivatives of E_{1x} in the first equation of Equation (2.52), E_{1x} in terms of E_{1y} and E_{1z} can be written as

$$E_{1x} = -\frac{1}{C_{11}} \left(B_{12} \frac{\partial E_{1y}}{\partial x} + B_{13} \frac{\partial E_{1z}}{\partial x} + C_{12} E_{1y} \right). \tag{2.62}$$

We apply a top hat electric field as defined in Equation (2.29) such that any derivative with respect to x that is not applied to a perturbed electric field is zero and substitute explicitly for E_{1x} in the remaining equations of Equation (2.52). We are left with two coupled differential equations

$$\begin{aligned} \left(A_{22} - \frac{B_{12}^2}{C_{11}} \right) \frac{\partial^2 E_{1y}}{\partial x^2} - \frac{B_{12} B_{13}}{C_{11}} \frac{\partial^2 E_{1z}}{\partial x^2} + \frac{B_{13} C_{12}}{C_{11}} \frac{\partial E_{1z}}{\partial x} & \\ + \left(\frac{C_{12}^2}{C_{11}} + C_{22} \right) E_{1y} + C_{23} E_{1z} = 0 & \qquad (2.63) \\ \left(A_{33} - \frac{B_{13}^2}{C_{11}} \right) \frac{\partial^2 E_{1z}}{\partial x^2} - \frac{B_{12} B_{13}}{C_{11}} \frac{\partial^2 E_{1y}}{\partial x^2} - \frac{B_{13} C_{12}}{C_{11}} \frac{\partial E_{1y}}{\partial x} & \\ + C_{23} E_{1y} + C_{33} E_{1z} = 0. & \qquad (2.64) \end{aligned}$$

If we take Region (i) to be where $x < -L$, Region (ii) to be where $-L < x < L$, and Region (iii) the be where $x > L$, then the above coupled second order differential equations have constant coefficients in each region individually, and we can assume a solution $\mathbf{E}_1 \propto \exp(i\kappa x)$. This yields the following characteristic system of equations:

$$\left[-\kappa^2 \mathbf{R} + i\kappa \left(\mathbf{S} - \mathbf{S}^T \right) + \mathbf{T} \right] \cdot \mathbf{E}_1 = 0, \tag{2.65}$$

where $\mathbf{R}$, $\mathbf{S}$, and $\mathbf{T}$ are 2×2 matrices, the superscript T denotes the transpose, and the vector $\mathbf{E}_1$ contains the components E_{1y} and E_{1z}. The nonzero matrix elements are as follows:

$$R_{11} = A_{22} - B_{12}^2/C_{11} \tag{2.66}$$

$$R_{12} = R_{21} = -B_{12}B_{13}/C_{11} \tag{2.67}$$

$$R_{22} = A_{33} - B_{13}^2/C_{11} \tag{2.68}$$

$$S_{12} = B_{13}C_{12}/C_{11} \tag{2.69}$$

$$T_{11} = C_{12}^2/C_{11} + C_{22} \tag{2.70}$$

$$T_{12} = R_{21} = C_{23} \tag{2.71}$$

$$T_{22} = C_{33}. \tag{2.72}$$

Taking the determinant and setting it equal to zero, leads to an equation that is biquadratic in κ, which has the following solution:

$$\kappa = \pm \left[\frac{1}{2A} \left(-B \pm \sqrt{B^2 - 4AC} \right) \right]^{1/2}, \tag{2.73}$$

where $A = R_{11}R_{22} - R_{12}^2$, $B = 2R_{12}T_{12} - S_{12}^2 - R_{22}T_{11} - R_{11}T_{22}$, and $C = T_{11}T_{22} - T_{12}^2$. The general solution to the electromagnetic top hat is

$$\text{Region (i)}: \mathbf{E}_1 = A_1\mathbf{e}_1 \exp\left(\pm i\kappa_1 x\right) + A_2\mathbf{e}_2 \exp\left(\pm i\kappa_2 x\right) \tag{2.74}$$

$$\begin{aligned} \text{Region (ii)}: \mathbf{E}_1 = {} & B_1\mathbf{e}_1 \exp\left(\pm i\kappa_1 x\right) + B_2\mathbf{e}_2 \exp\left(\pm i\kappa_2 x\right) \\ & + B_3\mathbf{e}_3 \exp\left(\pm i\kappa_3 x\right) + B_4\mathbf{e}_4 \exp\left(\pm i\kappa_4 x\right) \end{aligned} \tag{2.75}$$

$$\text{Region (iii)}: \mathbf{E}_1 = C_1\mathbf{e}_1 \exp\left(\pm i\kappa_1 x\right) + C_2\mathbf{e}_2 \exp\left(\pm i\kappa_2 x\right), \tag{2.76}$$

where the sign of κ used in Region (i) and (iii) are chosen such that the solution is evanescent as $x \to \pm\infty$. The vectors $\mathbf{e}_n$ are the wave electric field polarization in the yz plane associated with a given κ_n, and can be determined from [82]

$$\mathbf{e}_n = \left(\kappa_n^2 R_{22} - T_{22}\right)\hat{y} + \left(T_{12} - i\kappa_n S_{12} - \kappa_n^2 R_{12}\right)\hat{z}. \tag{2.77}$$

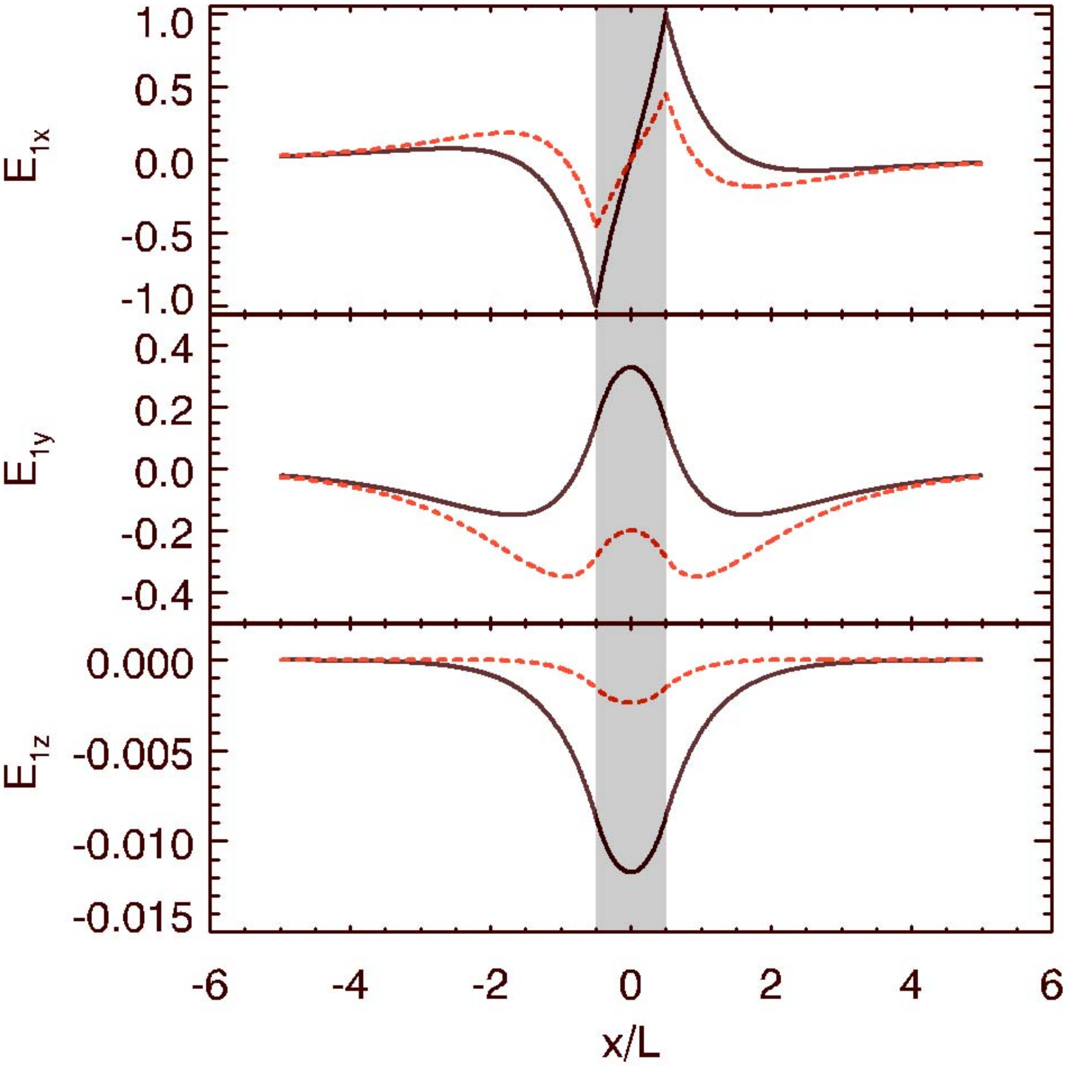

Figure 2.5: Real (solid black) and imaginary (dashed red) parts of the radial eigenfunctions of E_{1x} (top), E_{1y} (middle) and E_{1z} (bottom) for $L = 0.05$ m^{-1}, $E_0 = 400$ V/m, $B_0 = 300$ G, $n_0 = 10^{16}$ m^{-3}, $T_e = 3.0$ eV, $k_y = -7.7$ m^{-1}, $kz = 0.1$ m^{-1}, $\omega/\Omega_i = 0.713$, and $\gamma/\Omega_1 = 0.0927$.

We require that the function and its derivative be continuous at both boundaries, $x = -L$ and $x = L$, for each component of the perturbed electric field. The resulting system of equations

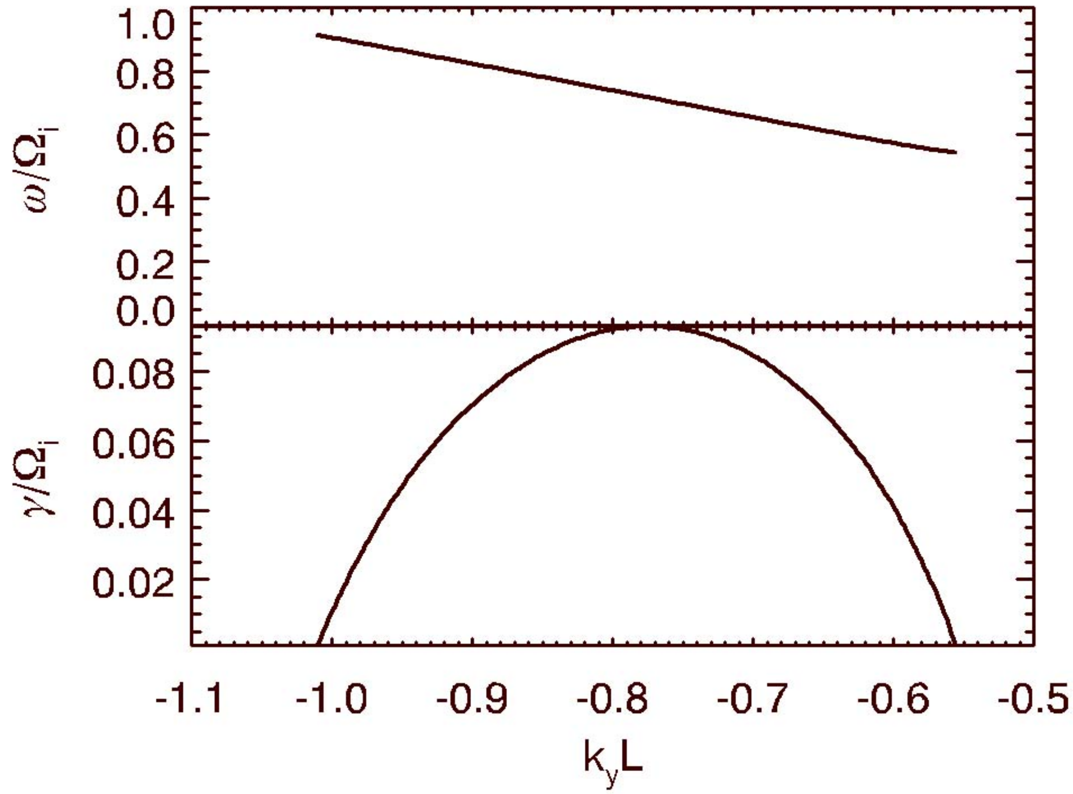

Figure 2.6: Real frequency (top) and growth rate (bottom) as a function of normalized k_y for the same parameters for Figure 2.5. Figure depicts the two thresholds for the instability, where the velocity threshold occurs for $k_yL = -0.58$.

is solved for the eigenvalue ω and eigenvector A. Figure 2.5 shows the resulting eigenfunctions for the experimentally relevant plasma parameters: density $n_0 = 10^{16}$ m^{-3}, electron temperature $T_e = 3.0$ eV, magnetic field $B_0 = 300$ G, electric field $E_0 = 400$ V/m, and electric field width $L = 0.05$ m. Figure 2.6 shows the dependence of the normalized real frequency (top) and normalized growth rate (bottom) as a function of k_yL. The threshold at $k_yL = -1.01$ occurs when the real frequency approaches the ion cyclotron frequency. The opposite threshold is equivalent to the velocity threshold for the instability.

2.5 Velocity Shear Modified Alfvén Wave Dispersion Relation

We now consider a smooth, continuous electric field profile, and we seek to examine the modifications to the typical Alfvén wave dispersion relation due to the presence of sheared transverse plasma flows. As we saw in Section 2.2, the first consequence of imposing an electric field profile in the $\hat{x}$-direction is that the wave becomes bounded in this direction and an effective k_x is now present. Although we can no longer Fourier transform in the x direction, we instead allow $\partial^2/\partial x^2 \rightarrow -k_x^2$ in Equation (2.52), where k_x now represents an averaged quantity over the profile as in a WKB approximation. We use the weak shear limit, $\frac{1}{\Omega_i}\frac{\partial v_E}{\partial x} << 1$, to aid in clarity of the physics although this limit can be relaxed. With these considerations and the assumption that ω_1 is on the order of Ω_i, $\eta_\alpha = 1$, $D_\alpha = 1 - \omega_1^2/\Omega_\alpha^2$, and we can rewrite Equation (2.52) as:

$$\begin{pmatrix} S - n_y^2 - n_z^2 & n_x n_y + \delta_0 & n_x n_z \\ n_x n_y + \delta_0 & S - n_z^2 + \delta_1 - n_x^2 & n_y n_z + \delta_2 \\ n_x n_z & n_y n_z + \delta_2 & P - n_x^2 - n_y^2 \end{pmatrix} \begin{pmatrix} E_{1x} \\ E_{1y} \\ E_{1z} \end{pmatrix} = 0, \tag{2.78}$$

where we have used that $S = \frac{\omega_{pi}^2}{\omega^2}\frac{\omega_1^2}{\Omega_i^2 - \omega_1^2}$, $P = \frac{\omega_{pe}^2}{\omega^2}\zeta^2 Z'(\zeta)$, $\delta_0 = S\frac{k_x v_E}{\omega_1}$, $\delta_1 = \delta_0^2/S + \delta_2^2/P - S(1 - \frac{\omega^2}{\omega_1^2})$, and $\delta_2 = P\frac{k_z v_E}{\omega_1}$. We obtain the dispersion relation by taking the determinant of Equation (2.78) and setting it equal to zero. If v_E is zero, δ_0, δ_1, and δ_2 are zero, and the dispersion relation reduces to:

$$\left(S - n^2\right)\left[\left(S - n_z^2\right)\left(P - n_\perp^2\right) - n_\perp^2 n_z^2\right] = 0. \tag{2.79}$$

The first factor describes the fast mode or compressional Alfvén wave, and the second factor describes the shear Alfvén wave. When $v_E \neq 0$, setting the determinant of Equation (2.78) equal to zero leads to the following dispersion relation:

$$\begin{aligned} &\left(S - n^2\right)\left[\left(S - n_z^2 + \delta_1\right)\left(P - n_\perp^2\right) - n_x^2 n_z^2 - \left(n_y n_z + \delta_2\right)^2\right] = \\ &- \left(P - n^2\right)\left(n_x^2 \delta_1 - \delta_0^2 - 2 n_x n_y \delta_0\right) + \left(n_x \delta_2 - n_z \delta_0\right)^2 . \end{aligned} \tag{2.80}$$

The presence of the inhomogeneous flow couples the compressional and shear Alfvén waves, and the dispersive properties can be significantly modified. These modifications will be examined in more detail in Section 4.4 with a comparison to the experimental observations.

Chapter 3

Experimental Setup

All of the experiments described in this dissertation were conducted in the Space Physics Simulation Chamber (SPSC) at the Naval Research Laboratory in Washington, DC. The SPSC is a large-scale, linear plasma device used to investigate basic near-Earth space plasma phenomena in appropriately scaled plasma conditions. The main objective of the space experiments section is to act as a bridge between *in situ* space data and theory to improve the understanding of basic geospace plasma processes. This work is in support of the Office of Naval Research's Space Research and Space Technology focus area. In the present chapter, we will give specific details of the the SPSC layout, capabilities, and plasma source. This will be followed by a detailed description of the experimental setup including all diagnostics used in the experiment.

3.1 Space Physics Simulation Chamber

The SPSC is composed of two main sections: the Main Chamber and the Source Chamber. Figure 3.1 shows a photograph of the SPSC with the Source Chamber section on the left-hand side of the photo. The two chambers are separated by a 70 cm gate valve that allows for the two chambers to be operated individually or as one long chamber. The Source Chamber was initially designed as a place to create and condition the plasma before injecting it into the larger volume of the Main Chamber, however, for the experiments reported here, it is used a separate experimental volume.

The Main Chamber is a 5-m long, 1.8-m diameter stainless steel vacuum chamber pumped by two cryogenic pumps with a base pressure of approximately 5×10^{-7} Torr. It has five water-cooled electromagnets capable of producing a maximum uniform axial magnetic field of 250 G. The plasma source is a large grid hot filament source composed of 140 Tungsten filaments that

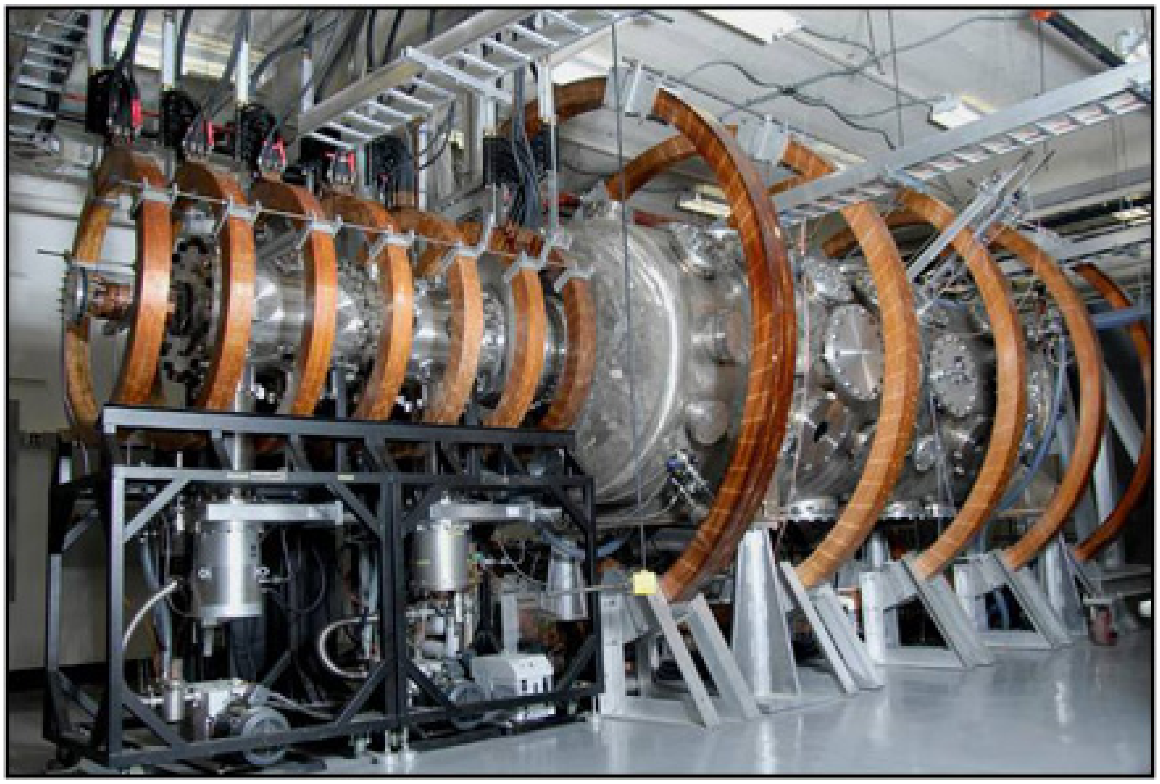

Figure 3.1: A photograph of the Space Physics Simulation Chamber.

are heated by a 20 V, 600 A power supply, which is capable of producing up to 20 A of emission current. The Argon plasma column has a diameter of approximately 75 cm with electron density up to 10^{10} cm^{-3} and electron temperature $0.1 - 1.5$ eV. The typical operating pressure is 10^{-4} Torr, which keeps the neutral collision frequency low.

The Source Chamber is a 1.5-m long, 0.55-m diameter stainless steel vacuum chamber that is pumped by turbo pumps with a typical base pressure 1×10^{-7} Torr. It has seven water-cooled electromagnets: each magnet has an inner diameter of 1.09 m and 110 turns. The first and last magnet in the array are each powered by two 60 V, 200 A power supplies. The inner five magnets are individually powered by a 40 V, 300 A power supply. The whole array is capable of producing a uniform axial magnetic field up to 750 G. The plasma source is an RF inductively coupled source, which is driven by a 250 W broadband amplifier with a frequency range of 10 kHz to 200 MHz. The source is typically operated at 14.2 MHz and 100 W of RF power yielding a 16-cm diameter

Argon plasma column with electron density $n = 10^{10}$ cm^{-3} and electron temperature $T_e = 3 - 5$ eV. The typical operating pressure is 1 mTorr, which results in an ion-neutral collision frequency of $\nu_{in} = 3.9 \times 10^3$ s^{-1}.

3.2 Experimental Layout

Figure 3.2 shows a schematic of the experimental setup. The ring electrodes are placed at the end of the internal axial translation stage approximately 125 cm away from the RF plasma source. The radial translation stages are in a plane approximately 20 cm away from the ring electrodes. In this plane are an emissive probe, a double probe, and a $\dot{B}$ probe. Each of the radial probes can be retracted to $r = 25$ cm, and can be translated 35 cm. There are two setups for the probe on the axial translation stage for the initial electrostatic experiments and the subsequent electromagnetic experiments.

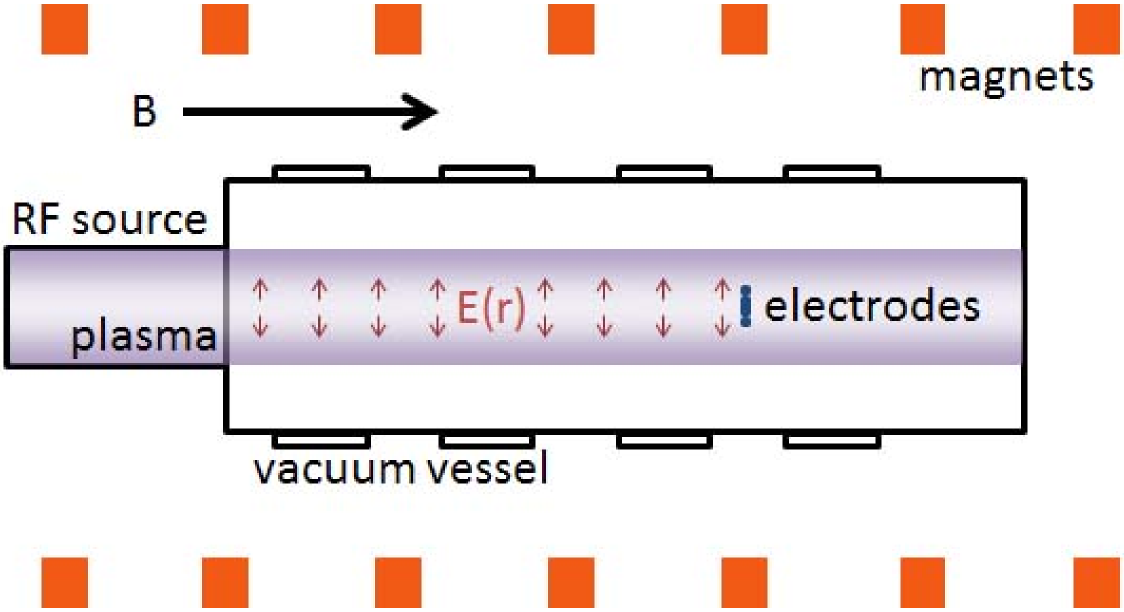

Figure 3.2: A schematic of the experimental setup.

For the electrostatic experiments, a probe with three single-tipped Langmuir probes was attached to the axial translation stage. The probe tips were displaced radially by approximately 1.0 cm center-to-center. This allowed for one probe tip on axis, one in the space between the ring electrodes, and one within the second electrode. Each tip consisted of a 3.2 mm-diameter stainless steel tube that was 3 mm long. For the electromagnetic experiments, the ring probe was attached to the axial translation stage, which is shown in Figure 3.11.

3.2.1 Plasma Source

In order to be able to measure the electromagnetic component of the instability, it was necessary to increase the plasma beta $\beta = \frac{nkT}{B^2/2\mu_0}$ in the experiment. Plasma beta is the ratio of the kinetic to magnetic pressure in the plasma, which is an effective measure of the ability of the plasma to modify the background magnetic field. The original experiments investigating the electrostatic velocity shear-driven ion cyclotron instabilities conducted in the SPSC were done at very low values of plasma beta $\beta = 8 \times 10^{-7}$, which were far too low to observe electromagnetic effects. In order to achieve the higher density and temperatures needed to increase β, the hot filament plasma source was replaced with an inductively coupled RF source.

The design for the RF antenna followed the considerations of Chen [25]. We use a half-wavelength Nagoya Type-III antenna [107] around a Pyrex tube as our plasma source. The tube has a 10-cm radius and is 45 cm long. Under these constraints we need to determine the proper length for the antenna for good coupling to the plasma wave we will launch. The wave we are trying to launch with our antenna is a helicon wave, which is just a bounded whistler mode. The dispersion relation for the whistler mode propagating at an angle θ with respect to the magnetic field is given by:

$$k^2 = \frac{\omega^2}{c^2} - \frac{\omega\omega_{pe}^2}{c^2\left(\omega - \Omega_{ce}\cos\theta\right)}. \tag{3.1}$$

If $\omega \ll \Omega_{ce}$ the displacement current term, ω^2/c^2, and the ω term in the denominator can be neglected. In this limit (3.1) can be written as:

$$k^2 = \frac{\omega\omega_{pe}^2}{c^2\Omega_{ce}\cos\theta}. \tag{3.2}$$

We can write the total wave number k as a sum of the perpendicular $k_\perp$ and parallel $k_\|$ components with respect to the background magnetic field, which allows us to write $\cos\theta = k_\|/k$. Since the helicon wave is bounded, the value of $k_\perp$ is determined by the boundary conditions. For a cylinder of radius a coaxial with B, we expect the lowest order radial function to be an m-th order Bessel function of the first kind $J_m(k_\perp r)$, and the edge of the cylinder must match with the first zero crossing of the radial wave function, i.e. $J_m(k_\perp a) = 0$. This determines the value of the perpendicular wave number $k_\perp = p_{m1}/a$, where we have used that p_{m1} is the first zero of the Bessel function with azimuthal mode number m. The Nagoya Type-III antenna will launch a cylindrical wave with azimuthal mode number $m = 1$, which yields $p_{11} \approx 3.83$. This implies that the perpendicular wave number is $k_\perp = 38.3$ m^{-1}. Substituting for $\cos\theta$ into Equation (3.2), yields the following expression:

$$k = \frac{\omega}{k_\|}\frac{\omega_{pe}^2}{c^2\Omega_{ce}} = e\mu_0 v_p \frac{n}{B}, \tag{3.3}$$

where we have used that $v_p = \omega/k_\|$, which is the wave phase velocity in the direction parallel to the magnetic field.

The impact-ionization cross section for Argon peaks for electron energies between $W = 50-200$ eV [98]. The optimal coupling for plasma production is achieved when the wave is resonant with electrons in this energy range, $\omega = k_\| v_p$. This allows the wave to sustain the plasma discharge by energizing electrons through Landau damping into the energy range for optimal ionization. We take $W = 50$ eV, which yields $v_p = \sqrt{2W/m_e} = 4.19 \times 10^6$ m/s. We choose a parallel wavelength of 30 cm, which corresponds to $k_\| = 20.9$ m^{-1}. These values result in a resonant frequency $f = \frac{\omega}{2\pi} \approx 14$ MHz. This frequency fits well into the range of our RF amplifier and matching network. Putting this $k_\|$ into Equation (3.3) and solving for n, we are left with a linear function in terms of B:

$$n = \frac{kB}{e\mu 0 v_p}, \tag{3.4}$$

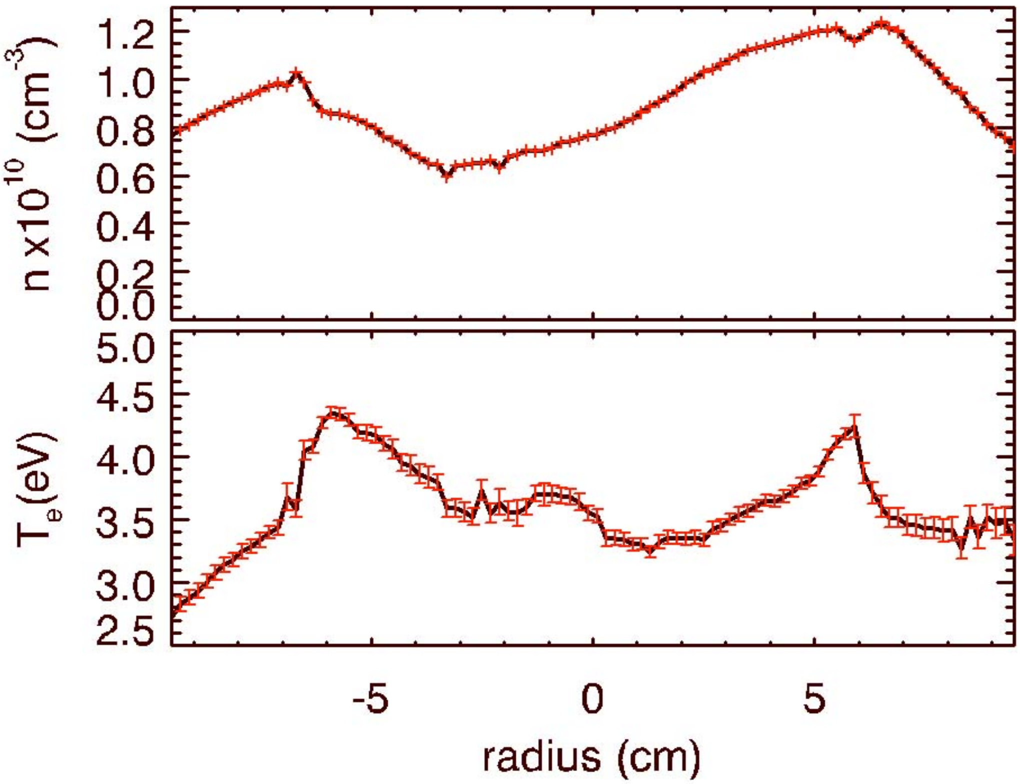

Figure 3.3: Typical density and electron temperature profiles.

which is what is required to fit the whistler dispersion relation. In order to be able to fit many ion gyroradii across the plasma column, we chose a background magnetic field of $B = 300$ G for typical operation. This results in approximately 30 ion gyroradii across the plasma column. At this magnetic field, the density would need to be $n = 1.55 \times 10^{12}$ cm^{-3} to fit the whistler dispersion relation. We constructed a Nagoya Type-III half-wavelength antenna with a 10-cm radius and 15-cm length. The antenna feed is composed of two 10 AWG bare solid conductor copper with single hole fish spine ceramic beads for electrical and thermal insulation. The entire assembly is covered in a copper braid that effectively extends the copper mesh Faraday cage to the matching network. This RF antenna design provides good coupling with the plasma. Figure 3.3 shows typical density and electron temperature profiles with 64 W of RF power as measured by a floating double probe. As can be seen a density of 1×10^{10} cm^{-3} can be achieved with a modest amount of power.

3.3 Diagnostics

The SPSC has a variety of plasma diagnostics to determine basic plasma parameters and wave characteristics. For these experiments, a floating double probe is used for plasma density and electron temperature measurements as well as density fluctuations. An emissive probe is used for DC plasma potential and electric field measurements and AC plasma potential fluctuations. Magnetic probes are used for measuring magnetic fluctuations. These diagnostics and the analysis used to determine the various plasma parameters and wave characteristics are described in the following sections.

3.3.1 Double Probe

Langmuir probes are often used to measure many basic plasma parameters: density, electron temperature, and plasma potential. Single-tipped Langmuir probes are difficult to interpret in RF plasma discharges due to the rapidly oscillating floating potential. One solution is to use an RF-compensated Langmuir probe [32], which makes use of RF chokes to reduce the voltage at the RF-source frequency across the plasma-probe junction. Another solution is to use a floating double probe. A double probe consists of two Langmuir probes connected by an isolated DC power supply. As the DC bias between the probes is swept, the current flowing between the probes is recorded. Since no ground reference is needed, the floating potentials of the probes are allowed to follow the oscillations in the plasma. This makes them ideal for use in RF generated plasmas.

To understand the operation of this diagnostic, consider an ideal double probe with identical tips. If either tip were swept as a Langmuir probe with the power supply referenced to ground, the resulting I-V characteristic would look like that shown in Figure 3.4, where collected electrons are treated as a positive current. One important point to note in the I-V characteristic is the floating potential V_f, which is the potential at which no net current is collected by the probe. This is the potential that an electrically isolated or "floating" electrode would assume in the plasma.

In the double probe configuration, rather than being referenced to chamber ground, an isolated power supply is connected between the two probe tips and the system as a whole floats electrically

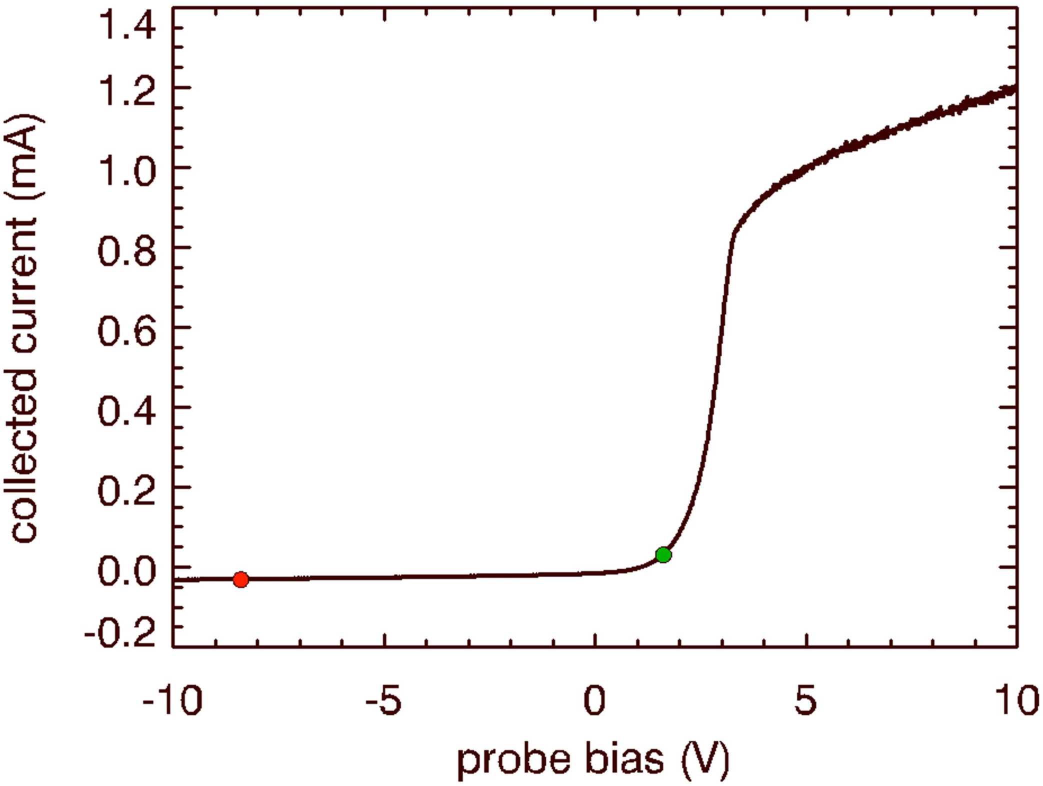

Figure 3.4: Typical current-voltage trace for a single-tipped Langmuir probe.

with respect to the plasma potential. If there is no DC bias between the probes, both probes will be at the floating potential and there will be no current flowing between them. If we now bias the probes relative to each other, the potential of probe 1 moves above the floating potential, and probe 1 collects predominantly electrons. Likewise, the potential of probe 2 moves below the floating potential, and probe 2 collects predominantly ions. With our chosen sign convention, this corresponds to current coming in to the circuit at probe 1 and leaving the circuit at probe 2. According to Kirchoff's laws, the magnitude of the current collected by each probe must be equal. In this way, the probes move around on the I-V characteristic with a separation determined by the DC bias and the voltages are such that magnitude of the collected currents are equal, which is the value of the current flowing through the circuit. As an example, we apply a 10 V bias between the probes. The voltage and collected current for probe 1 (green) and 2 (red) are indicated in Figure

3.4. Probe 1 floats to 1.62 V and collects 3.1 μA, while probe 2 floats to -8.39 V and collects -3.1 μA. The net current is zero, and the voltage difference is 10 V, the applied bias. The total current through the circuit is 3.1 μA.

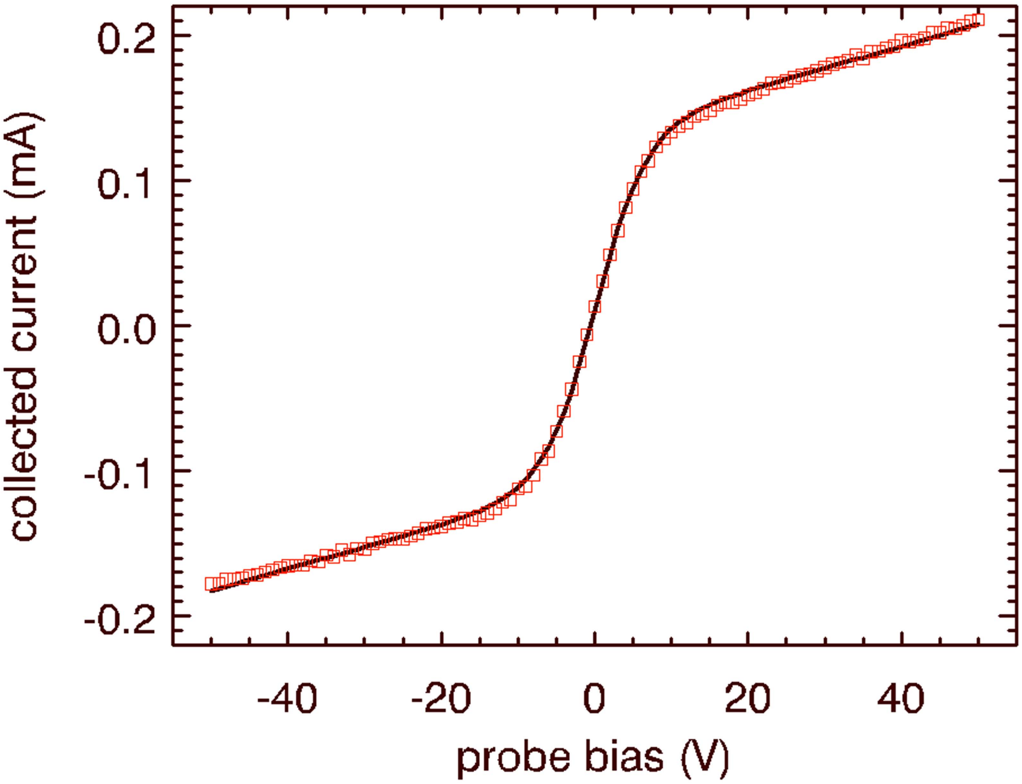

Figure 3.5: Typical current-voltage trace for a floating double probe (squares) and best non-linear fit (solid line).

We follow the derivation by Hershkowitz [45] for the theoretical I-V characteristic of a floating double probe. We assume that a double probe consisting of two identical spherical probes, labeled 1 and 2, with area A are inserted in to a Maxwellian plasma with density n and temperature T_e. Since the system is isolated from ground the electron and ion currents to the probes must cancel:

$$i_{1+} + i_{2+} = i_{1-} + i_{2-}. \tag{3.5}$$

The current I in the loop can be written as

$$I = i_{1+} - i_{1-} = i_{2-} - i_{2+}. \tag{3.6}$$

We can calculate the electron current density collected by one of the probes by taking the first moment of the distribution function

$$j_e(V) = e \int f(\mathbf{x}, \mathbf{v}, t) v_z dv_x dv_y dv_z, \tag{3.7}$$

where $f(\mathbf{x}, \mathbf{v}, t)$ is the electron distribution function. Evaluating the integral and multiplying by the probe area gives an expression for the probe current

$$i_{1-} = i_{1-}^* \exp\left(\frac{eV_1}{T_e}\right), \tag{3.8}$$

where $i_{1-}^* = Aen_0\sqrt{T_e/me}$ is the electron saturation current. Equations (3.5-3.8) can be rearranged to give

$$I = i_+ \tanh\left(\frac{eV}{2T_e}\right), \tag{3.9}$$

where $i_{1+} = i_{2+} = i_+$, which is the ion saturation current and V is the relative bias voltage defined as $V = V_1 - V_2$. The approximate ion saturation current is given by the following expression

$$i_+ = neA\sqrt{\frac{T_e}{m_i}}, \tag{3.10}$$

where m_i is the ion mass. Orbital theory developed by Langmuir and Mott-Smith [72] gives geometric corrections to the I-V characteristic. For spherical probes the sheath increases roughly linearly with increasing bias. This is seen in the I-V trace as a linear increase in the ion saturation current with increasing bias. With these considerations, the following model is used to analyze the double probe data:

$$I(V) = a_0(V - a_1) + a_2 \tanh\left(\frac{V - a_1}{a_3}\right) + a_4, \tag{3.11}$$

where a_1 allows for a voltage shift in the trace and a_4 allows for a current shift. A least squares fit is applied to the double probe data using the Levenberg-Marquardt method [62]. Figure 3.5 shows a typical double probe trace and best fit result from the fitting routine. Parameters a_2 and a_3 in conjunction with Equations (3.5) and (3.10) can be used to determine the electron temperature and plasma density. We first calculate the electron temperature in eV

$$T_e = \frac{a_3}{2}. \tag{3.12}$$

Once we have the electron temperature we can calculate the plasma density in m^{-3}

$$n = \frac{a_2}{eA\sqrt{eT_e/m_i}}, \tag{3.13}$$

where the probe area A is given in m^2 and the factor of e within the square root is used to convert the electron temperature to Joules.

The least squares fit also returns a covariance matrix. The diagonal of the covariance matrix is the square of statistical error in each of the best fit parameters. These errors along with the estimated errors in the probe area can be propagated through to determine the error in the determination of the plasma parameters. The error propagation equations were determined using the general procedure using partial derivatives with respect to each parameter as described in Bevington and Robinson [14]. The specific error equations are as follows

$$\begin{aligned} \delta T_e &= \sqrt{\frac{\delta a_3}{2}} && (3.14) \\ \delta n &= n\sqrt{\left(\frac{\delta a_2}{a_2}\right)^2 + \left(\frac{\delta A}{A}\right)^2 + \left(\frac{\delta T_e}{2T_e}\right)^2}, && (3.15) \end{aligned}$$

where δa_2 and δa_3 come from the covariance matrix. These error estimates only incorporate statistical error and do not include systematic errors or errors associated with inaccuracies in the model. With these caveats in mind, the error calculated from the standard deviation of the plasma parameters determined from many shots lies within these error estimates.

The main section of the double probe used in the SPSC experiments is a 15-cm long 3.2-mm diameter four-bore ceramic tube. One pair of holes is filled with a 0.25-mm diameter nichrome wire used to heat the probe to minimize contamination. The probe tips are two stainless steel ball bearings with a diameter or 3.175 mm. In the other pair of holes of the four-bore ceramic tube, there is a 26 AWG enameled copper wire. Once the wire leaves the four-bore ceramic tube, it is housed in a 1.65-mm diameter single bore ceramic tube that is 2.5 cm long. The wire is then inserted in a small hole drilled into the ball bearings. The enameled copper wire serves as both an electrical connection to the probe tip as well as structural support. The two probe tips have a separation of 1.4 cm. When the probe is being used to measure density and temperature, the probe tips are aligned just off of being parallel with the magnetic field to prevent shadowing.

3.3.2 Emissive Probe

When an isolated probe is placed in a plasma, it initially collects more electrons than ions due to the greater mobility of the electrons. This charge imbalance causes the probe to float to a voltage lower than the plasma potential, which serves to impede electron collection and attract a sufficient number of ions to maintain a net current of zero. A probe that can emit as well as collect electrons can take advantage of this condition to provide an accurate measurement of the plasma potential. The emissive probe filament is heated to a temperature, where, when an applied voltage is swept in the manner of a Langmuir probe, the electron emission portion of the IV characteristic is 10 times the level of electron saturation current. At such high emissivity, the I-V characteristic in the transition region between electron emission and electron collection becomes very steep and the floating potential approaches the plasma potential. In this limit, a high impedance measurement of the floating potential of the probe yields an accurate estimate of the plasma potential [50].

The probe tip consists of an 3.2-mm diameter four-bore ceramic tube and a 0.125-mm diameter, 0.5-cm long thoriated tungsten filament. The filament is pressure fit into two adjacent holes of the ceramic tube along with a 22 AWG copper wire. An isolated 6-V, 5-A, power supply operating in constant current mode is used to heat the filament to thermionic emission. A high impedance measurement of the voltage is made between the low voltage side of the heater supply and chamber ground.

The following calibration procedure is used to determine an operating heater current such that the probe emits an electron current sufficient to cause the floating potential of the probe to approach the plasma potential for all electric fields applied in the experiment. For the calibration, the digital multimeter used to measure floating potential of the probe is replaced with a source meter. The source meter allows us to bias the probe and measure the collected or emitted current with high precision. Figure 3.6 shows the floating potential of an emissive probe as a function of the heater current. The floating potential will asymptote at the plasma potential. The threshold for this emissive probe was 2.50 A at 3.42 V for a total heating power of 8.5 W.

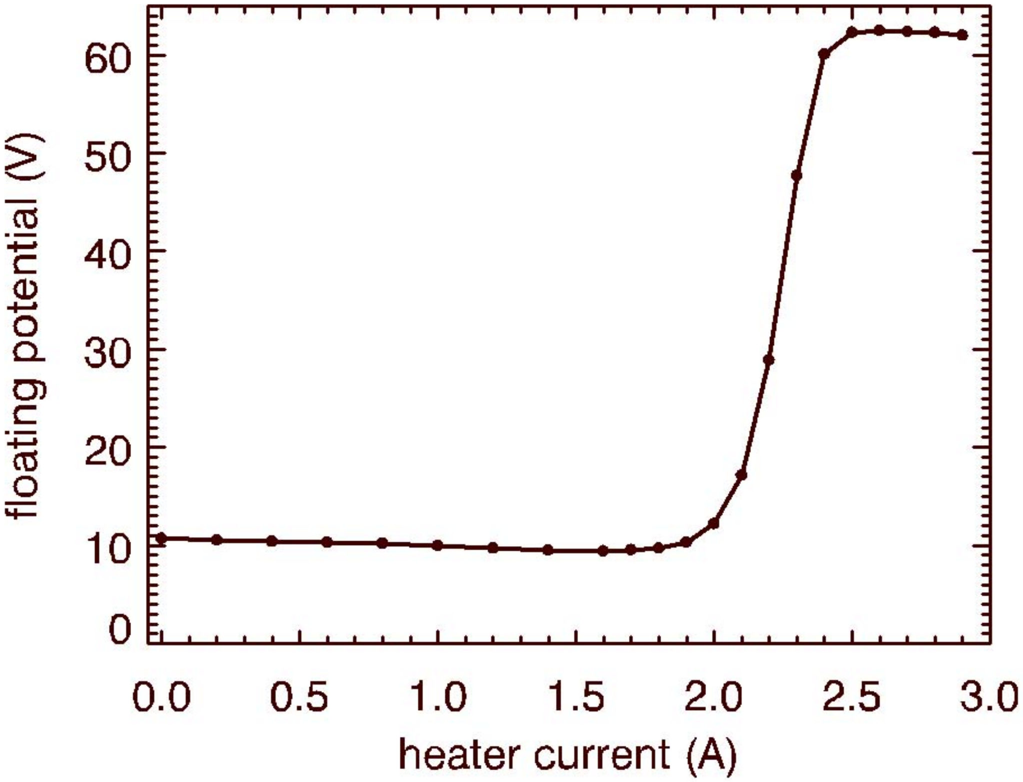

Figure 3.6: Emissive probe floating potential as a function of the applied heater current. The floating potential asymptotes at the plasma potential.

During normal operation of the emissive probe, we measure the radial profile of plasma potential. This profile is differentiated numerically to determine the radial electric field profile. Since the differentiation always considers the difference in the potential between two points, we do not concern ourselves with determining the best absolute measurement of the plasma potential. We can ignore the potential gradient across the filament due to the heater supply. This is also the reason we elect to use the floating potential of the probe instead of the more accurate limit of zero emission analysis technique [95] that can eliminate the effects of space charge on the plasma potential measurement.

A typical measurement consists of 100 voltage measurements at a given radial location. The average of the voltage measurements is taken as the plasma potential at that location, and the standard deviation of the measurements around the mean is taken as the statistical error in the measurement. We use the second order central algorithm for the numerical derivative:

$$f\left(x_i\right) = \frac{dy}{dx} = \frac{1}{2dx}\left(y_{i+1} - y_{i-1}\right). \tag{3.16}$$

This procedure causes us to lose the outer two radial points for every derivative. A sample plasma potential profile and derived electric field are plotted in Figure 3.7.

3.3.3 Magnetic Probe

A time varying magnetic flux through a loop of wire produces a voltage difference on the two ends of the loop according to Faraday's law. If we consider a harmonically varying magnetic field $\mathbf{B} = B_0 \exp\left[i(\mathbf{k}\cdot\mathbf{x} - \omega t)\right]$ through a stationary loop of area A, we can write Faraday's law as follows:

$$V = i\omega \mathbf{B}\cdot\hat{n}A, \tag{3.17}$$

where $\hat{n}$ is the unit vector normal to the loop. If we know the area of the loop and we measure the amplitude and frequency content of the voltage across the loop, we can calculated the amplitude of the magnetic field fluctuations at a given frequency.

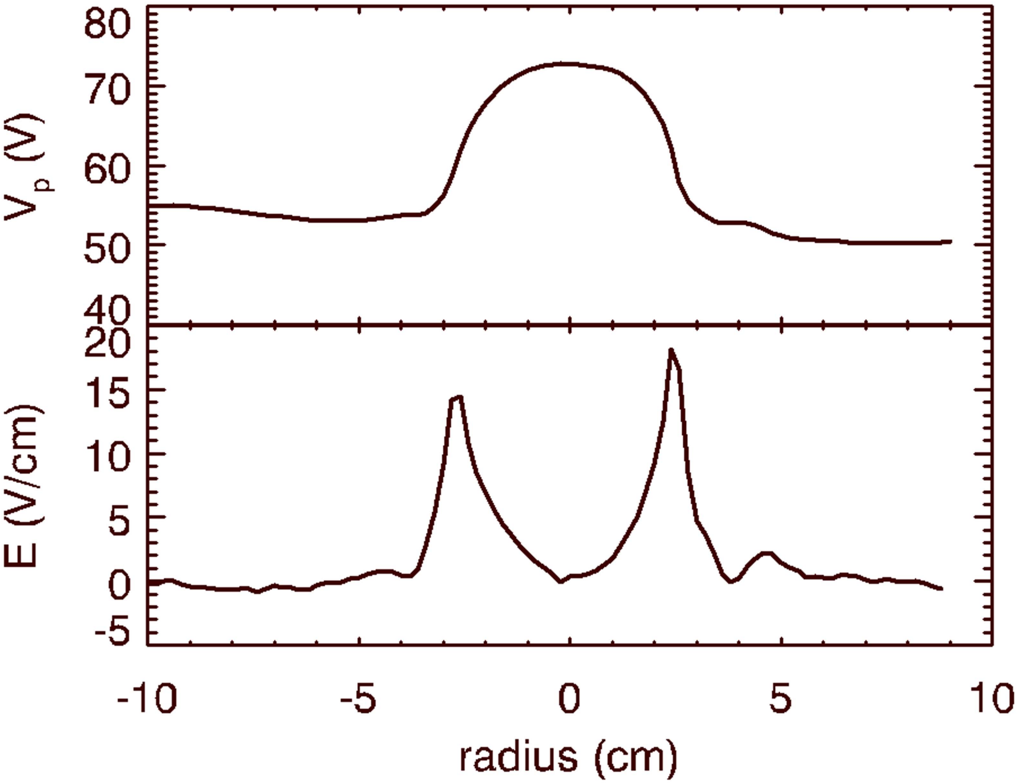

Figure 3.7: Example of plasma potential (top) and electric field (bottom) profiles.

An effective $\dot{B}$ probe must be small for good spatial resolution and minimal perturbation of the plasma, however, the total area must be large enough to measure small magnetic fields at our frequencies of interest. For the loop of the probe, we used a ceramic wound surface mount inductor with a nominal inductance of 33 μH. The inductor is 2.54 mm by 2.54 mm in cross-section and 3.25 mm long. The loop has a cross-sectional area of 0.0654 cm^2.

A twisted pair of wires is connected to each inductor, and the assembly is mounted to an 3.2-mm diameter ceramic tube. An insulating ceramic adhesive, Ceramabond, is used to rigidly attach the inductor and the ceramic tube while serving as an insulator between the electrical connections to the inductor and the plasma. A 4.8-mm stainless steel tube is placed over the ceramic tube, and aluminum foil is placed over the Ceramabond-covered inductor and tucked under the stainless steel tube. This assembly acts as an electrostatic shield for the probe. The foil is coated with a thin layer of Cerambond to insulate the foil from the plasma and to rigidly attach the stainless steel tube to the assembly.

A 11.4-cm diameter, 20-turn Helmholtz coil pair is used for probe calibration. The Helmholtz coil will produce a known and uniform axial magnetic field $B = (4/5)^{3/2}\mu_0 nI/R$, where n is the number of turns, I is the current, and R is the radius of the coil. With these dimensions, the region of magnetic field within 1% error is a radius of 3.4 cm [19], which is an order of magnitude larger than the coil. We use a 15 MHz function generator capable of producing a 10 V amplitude sine wave and sourcing the requisite current to drive the Helmholtz coil. The current in the coil is measured using a Pearson coil, which gives a 0.1 V/A signal with a response time less than 100 ns. With the probe centered in the Helmholtz coil, it is rotated to minimize the voltage signal and the direction of maximum signal is marked on the probe shaft. The minimum is easier to determine than the maximum due to the sign change. We record the output from the probe and Pearson coil for a frequency range of 100 Hz to 20 kHz with loop normal 90 degrees with respect to the axis of the Helmholtz coil. This gives us the frequency dependent error in the magnetic field component measured by the probe being calibrated With the probe rotated 90 degrees to give maximum signal, we repeat the frequency scan. A typical calibration curve for a three axis $\dot{B}$ probe is plotted in Figure 3.8, which shows the frequency dependent probe area calculated using Equation (3.17) for the frequency range of interest in the experiment. The color of the trace denotes the coil: coil1 (black), coil2 (red), and coil3 (green). The type of line denotes the magnetic field direction that was being tested: B_r (solid), B_θ (dotted), and B_z (dashed). The figure shows that the effective probe area for a coil in a direction perpendicular to the coil axis is over an order of magnitude smaller than the area parallel to the coil axis. Since the effective probe areas are relatively constant for the frequency range of interest, the value is averaged over the frequency range from 5 to 15 kHz. This yields an effective area for these probes of $A_1 = 23.1 \pm 0.5$ cm^2, $A_2 = 23.1 \pm 0.5$ cm^2, and $A_3 = 23.8 \pm 0.5$ cm^2. This gives approximately 350 turns for the coils.

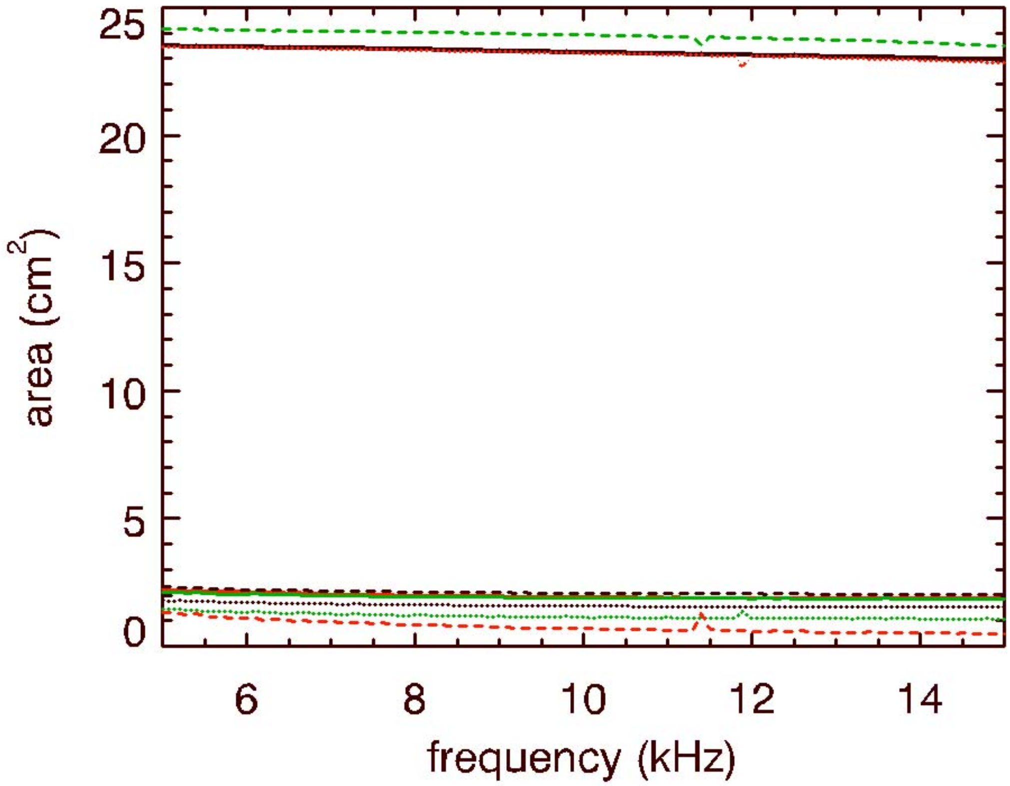

Figure 3.8: Typical calibration curves for $\dot{B}$ probes.

The first measurements of the magnetic fluctuations in our experiment were made using a spectrum analyzer, which has a sensitivity of -120 dBm but at the expense of losing phase information. These measurements indicated that maximum amplitude of the total magnetic fluctuations was approximately 0.25 μT. This results in voltage signals from the probe of approximately 100 μV. These voltage signals are too small for our oscilloscopes to measure, which is necessary for us to recover phase information for wave dispersion measurements. It was clear that we needed to design and build differential amplifiers for the probes.

3.3.4 Differential Amplifier Circuit

We chose a differential amplifier circuit for its large common mode rejection properties, which would insure that the recorded signal was due to the electric field inductively produced by the

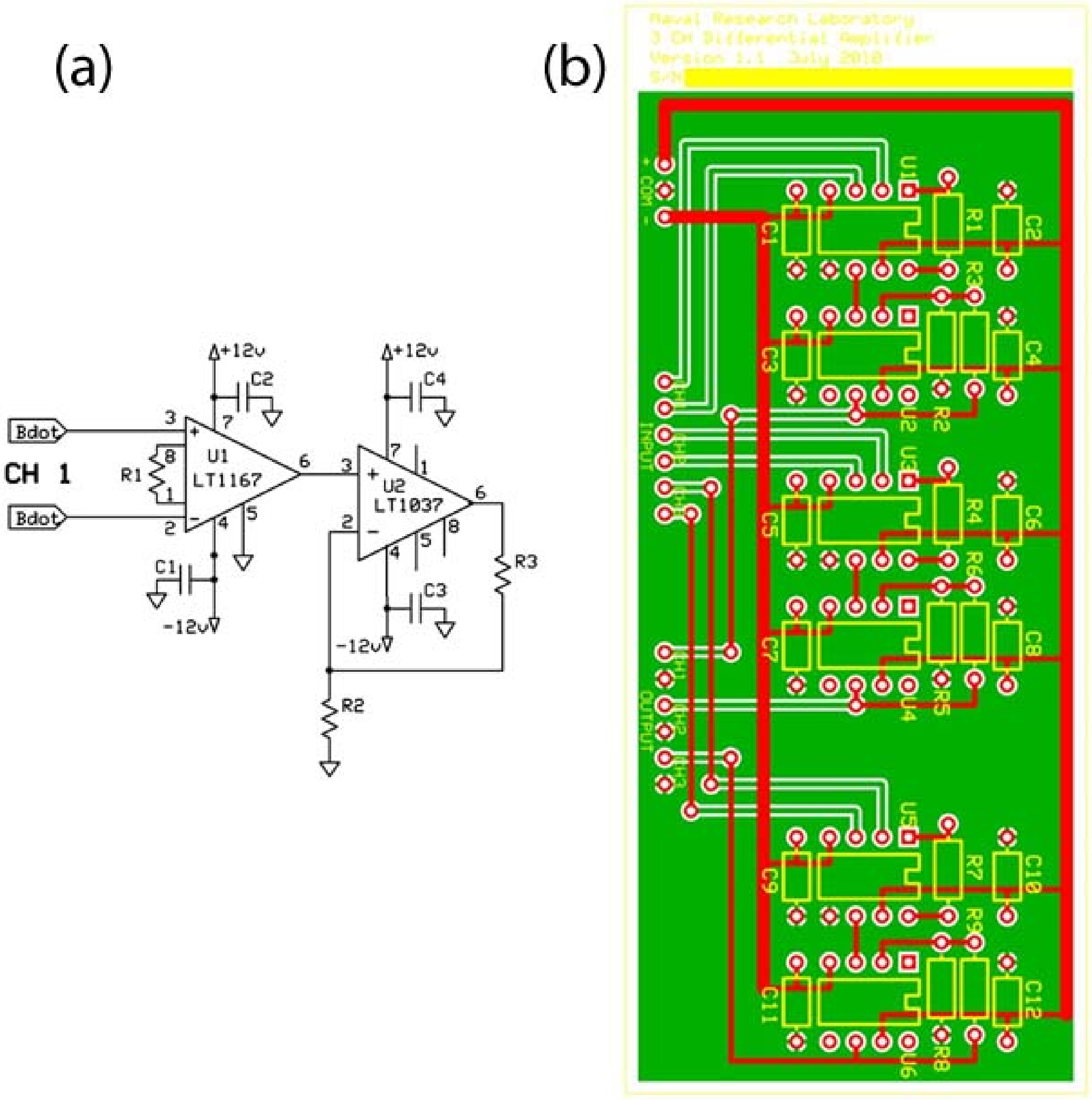

Figure 3.9: A schematic of the circuit (a) for a single channel differential amplifier and circuit board layout (b) for three amplification channels.

oscillating magnetic flux through the probe. A gain of 1000 was chosen for ease of oscilloscope measurements. This would have to be achieved in two stages in order to maintain the necessary frequency bandwidth. Figure 3.9 (a) depicts a schematic of the circuit for a single channel of amplification. The two main components are an instrumentation amplifier, the LT1167, and a low noise operational amplifier, the LT1037. Figure 3.9 (b) shows the circuit board layout for three amplification channels. Two of these boards were used to create a six channel differential amplifier box used for the six single $\dot{B}$ probes on the ring probe assembly. A similar six channel amplifier box was constructed for two three axis probes.

Code	Component
U1	LT1167
U2	LT1037
C1-C4	47 μF Tantalum 47 nF Ceramic
R1	500 Ω
R2	2 kΩ
R3	18 kΩ

Table 3.1: Component list for the differential amplifier circuit boards.

Table 3.1 lists the parts and values of the capacitors and resistors used in Figure 3.9. The LT1167 is a low noise instrumentation amplifier whose gain can be set by a single external resistor. The $500\ \Omega$ resistor sets the gain to 100. The voltage noise is 7.5 nV/$\sqrt{\text{Hz}}$. The main advantage of using this instrumentation amplifier is that it provides a typical common mode rejection of 125 dB at a gain of 100, which will limit the electrostatic pickup of the coil. The LT1037 is a low noise operational amplifier, with 2.5 nV/$\sqrt{\text{Hz}}$ wideband noise. The LT1037 is configured as a non-inverting amplifier with an additional gain of 10.

Each differential amplifier channel was separately calibrated using a network analyzer. The output port of the network analyzer was connected to one of the amplifier channels, the output of that amplifier channel was connected to the input port of the network analyzer through a 20 dB attenuator. The network analyzer sent a small amplitude signal at various frequencies from 500 Hz to 20 kHz, and recorded the amplified signal, averaging over a 100 Hz bandwidth. A typical calibration is plotted in Figure 3.10, which shows the magnitude (top) and phase (bottom) of the transmission coefficient, the ratio of the input power to output power as a function of frequency. As can be seen, the gain is relatively constant for the frequencies of interest, 5 to 20 kHz, and is approximately a gain of 1000. The phase, however, shows a linear change of approximately 0.8 degs/kHz over the frequency range tested. We must take this into account when analyzing phase correlation measurements as a function of frequency. Although the calibration curves were similar from channel to channel, we chose to individually calibrate a probe and its amplifier channel as a unit.

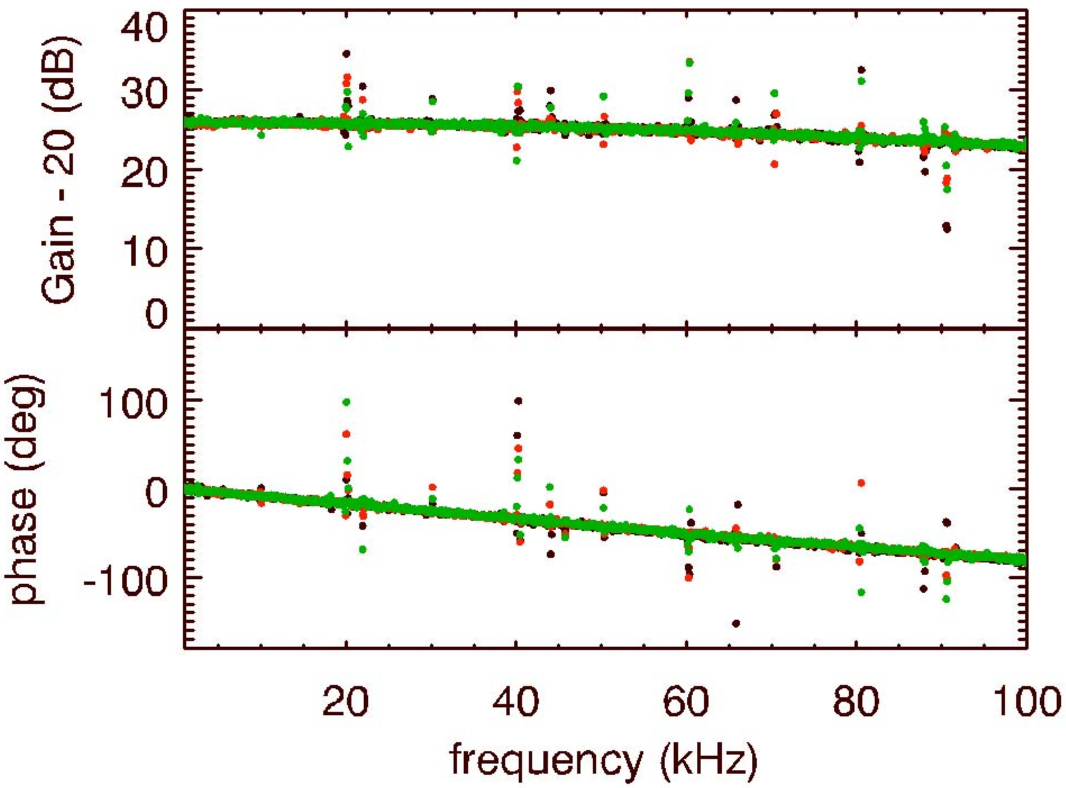

Figure 3.10: Typical calibration curves for the differential amplifier circuit showing the (top) magnitude and (bottom) phase of the ratio of input to output power for a 3 channel board.

3.4 Ring Electrodes

The electrodes used for the majority of the experiments presented here consist of a center disk and an annulus with a radial gap between the electrodes of 3 mm, which is approximately half an ion gyroradius. The electrostatic experiments, presented in Section 4.1, used a 2.2-cm diameter center disk and an annulus that was 2.5 cm wide and had an outer diameter of 5 cm. In the electromagnetic experiments, described in Section 4.2, we used a 2-cm diameter center disk and an isolated 0.6-cm wide annulus with an outer diameter of 3.8 cm. The electrodes were attached to a block of 6.4-mm thick teflon. Each electrode can be biased individually and sets the potential of a cylindrical shell of the plasma. The potential differences between these concentric shells of plasma generate an azimuthally symmetric, inhomogeneous radial electric field. This electric field in conjunction with the presence of the axial magnetic field, causes a cylindrically symmetric azimuthal plasma flow due to the $\mathbf{E} \times \mathbf{B}$ drift. The inhomogeneity in the radial electric field results in radial shear in the azimuthal velocity profile, which extends along the length of the device and is the source of the free energy to drive the observed instabilities.

3.4.1 SPSC Translation Stages

The SPSC is equipped with a variety of both internal and external translation stages for probe positioning. On the source chamber there are three axes for radial positioning, and one internal axial stage. Each axis consists of a controller, an amplifier, a stepper motor, and a stage with a precision lead screw. In addition there is a system consisting of three stages for x-y positioning of the laser induced fluorescence pump and probe beams and another internal motor mounted to the axial stage that connects to a vertical ring assembly that allows for radial positioning of an array of probes while maintaining a fixed azimuthal orientation. These translation stages will all be described in detail in the following section.

The three radial stages are all located on the same axial plane, 98 cm from the plasma source. All three radial stages allow for 50 cm of travel, but in order to help avoid collisions, each is limited to approximately 30 cm of travel. The two horizontal stages have lead screws with a pitch of 1 cm per turn. The stepper motors are operated such that one revolution is accomplished in 400 steps. This gives a minimum radial resolution of 25 μm. Each stage has a rotary encoder with a resolution of 4000 counts per revolution. The actual position of the probe can be determined to 2.5 μm. The vertical stage has a lead screw with a pitch of 0.25 cm per turn. The finer lead screw was used for smaller backlash for vertical mounting. This gives another factor of 4 decrease in the minimum step size. However, the spatial resolution of the measurements tends to be limited by probe size and not positioning errors.

The internal axial stage uses a special vacuum compatible motor designed to handle the lower heat transfer of the vacuum environment. The center of the translation stage carriage is 22.5 cm from the plasma source at its minimum axial position and can travel 76 cm away from the source. It also has a lead screw with a pitch of 1 cm per turn. The stage is mounted aligned with the cylindrical axis of the chamber at a 45 degree angle from the bottom of the chamber. The motor is equipped with a resolver whose output is equivalent to the 4000 counts per revolution rotary encoders used on the external motors.

Mounted to the carriage of the internal axial stage is another vacuum compatible motor. The shaft of this second motor is coupled to a vertical ring assembly shown in Figure 3.11. The ring assembly consists of two rings with aluminum ball bearings between them that allows them to freely rotate relative to each other. The inner diameter of the ring assembly is 26 cm, which is outside the main plasma column. When the motor spins the six probes, which are equally distributed azimuthally, rotate together. As the assembly rotates, the probe tips remain equally spaced azimuthally and the probes move radially. However, the probe tips suffer a rotation about the symmetry axis of the chamber and unequal radial step sizes. An amplifier capable of micro-stepping is used to control this stepper motor and causes the motor to take 2000 steps to complete a revolution. The micro-stepping results in an angular resolution of 3 mrads.

Let l be the probe length, and the initial position of the probe is such that it is aligned radially. If the probe is displaced by an angle θ from its initial position, the change in radial position of the probe is given by $\Delta r = l(1 - \cos\theta)$. If the probe is at an angle θ relative to its initial position and is displaced by a small angular step $\delta\theta$, the radial step can be expressed as $\delta r = l \sin\theta\delta\theta$. Since the probes will never be displaced by an angle larger than 90^{o}, this expression says that the largest δr will occur for the largest θ.

If we assume a typical probe length of 15 cm and that we want to scan 10 cm in radius, the angular displacement at $r = 10$ cm is approximately 19.5^{o}. Taking a step size of 3 mrads at this angle results in a radial step size of $\delta r = 0.15$ mm. The spatial resolution is again limited by the size of the probe and not the positioning system.

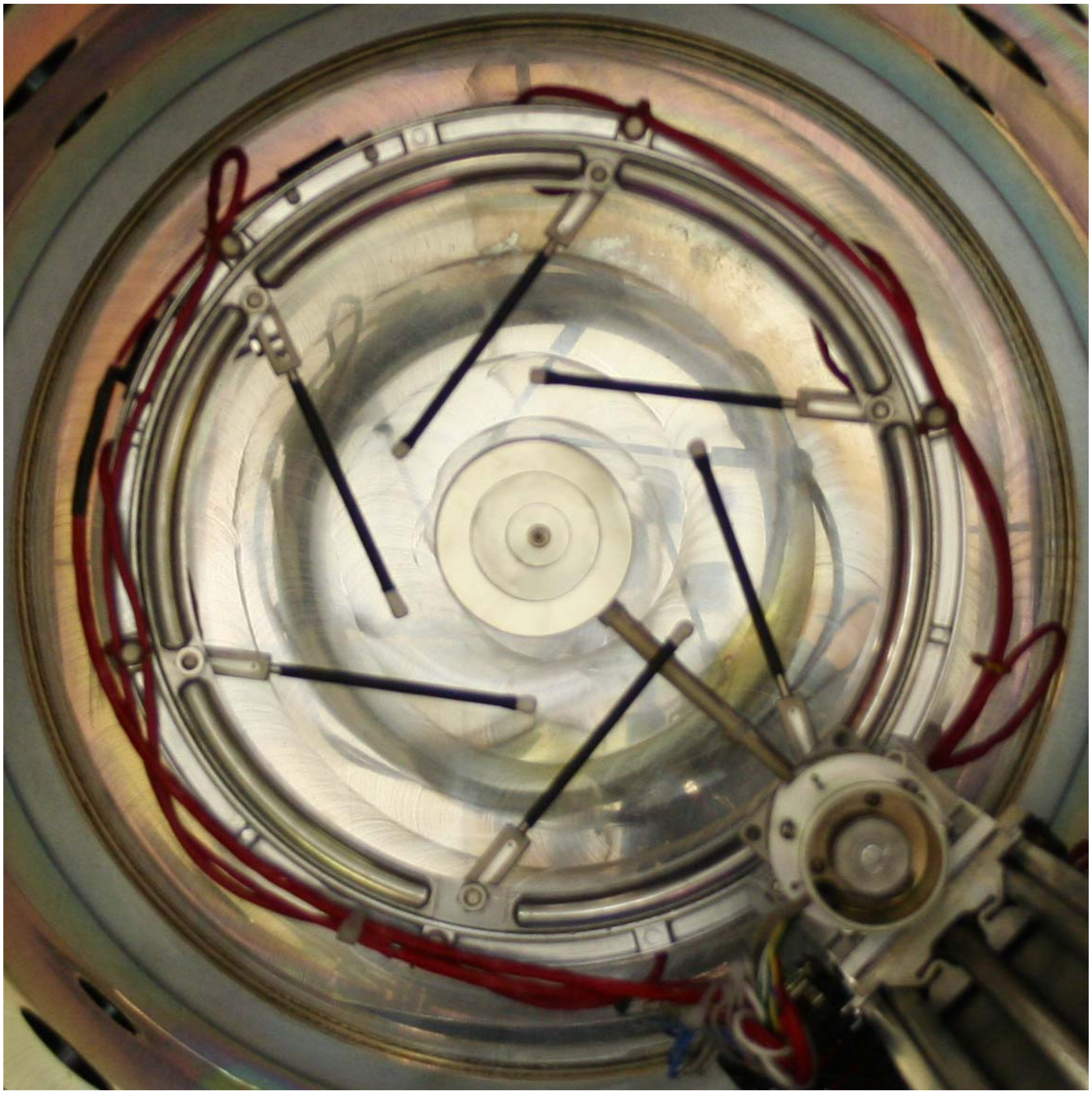

Figure 3.11: Photograph of internal ring assembly, which has six $\dot{B}$ probes mounted on it.

Chapter 4

Analysis

The electrostatic inhomogeneous energy density driven instability was studied thoroughly both theoretically and experimentally as discussed previously. It was also shown that the electromagnetic version of this instability can be well described by the electrostatic theory under certain conditions. This provides a natural starting point for the experiments in search of electromagnetic ion cyclotron waves driven by strongly sheared flows. This chapter will start with the electrostatic experiments used as a benchmark for the subsequent electromagnetic experiments. The second section will present the observations of the electromagnetic mode characteristics. Section three will present the dependence of some of these characteristics on plasma β. This chapter will end with a comparison of the observations to the existing theory.

4.1 Electrostatic Comparison

Parameter	WVU	NRL ES IEDDI	Auburn	NRL EM IEDDI
n (cm^{-3})	1.0×10^9	3.5×10^7	8.0×10^9	1.0×10^{10}
T_i (eV)	0.2	0.05	0.05	0.05
T_e (eV)	0.2	1.0	$5 - 10$	$3.0 - 5.0$
B (G)	1500	40	100	300
β	7.1×10^{-9}	8.8×10^{-7}	4.0×10^{-5}	5.0×10^{-5}
m_e/m_i	1.4×10^{-5}	1.4×10^{-5}	1.4×10^{-4}	1.4×10^{-5}

Table 4.1: Comparison of plasma parameters between previous electrostatic IEDDI experiments.

The previous experiments investigating the velocity shear-driven ion cyclotron instability were conducted under very different plasma conditions. Table 4.1 gives a summary of typical plasma parameters in the previous WVU, NRL, and Auburn electrostatic experiments and the current NRL electromagentic experiments. Although the experiments were conducted under a wide range of plasma conditions, it will be shown that using similar techniques to impose inhomogeneous radial electric fields, we can reproduce the important features of the electrostatic instability. For these experiments, we left the inner electrode disconnected while biasing the outer ring to 100 V. For comparison, the plasma potential with the electrodes disconnected is approximately 30 V. Figure 4.1 is a plot of the radial electric field profile for this configuration with 100 V bias (blue) and all electrodes disconnected (red), where the shaded boxes represent the location of the electrodes.

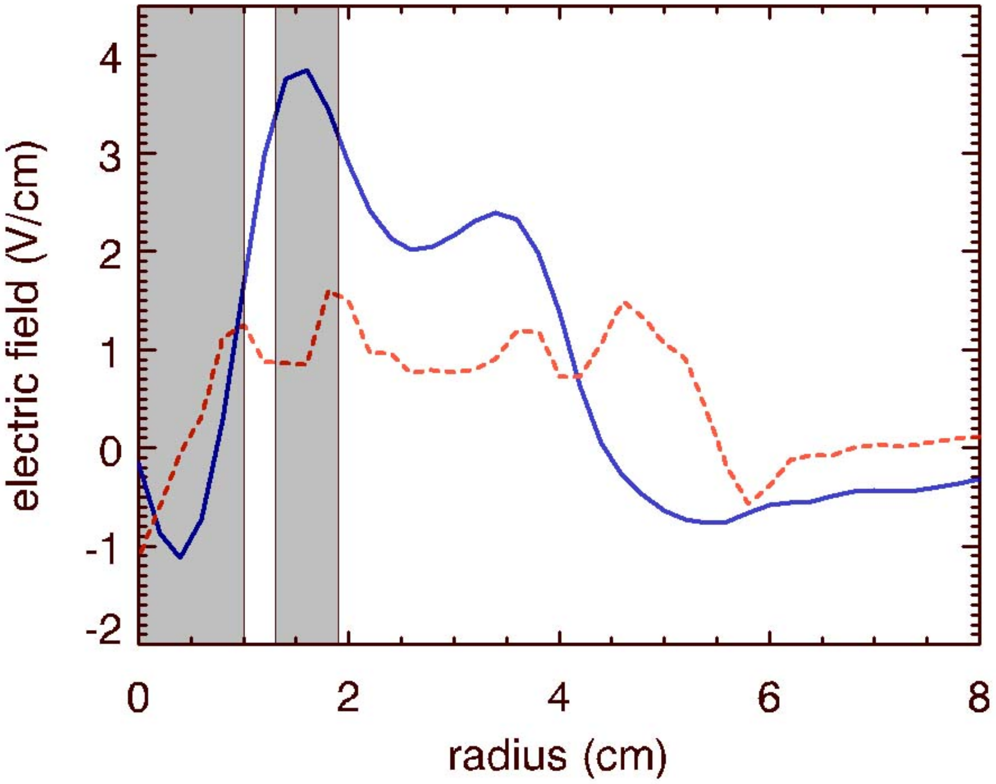

Figure 4.1: A plot of radial electric field with 100 V bias on Ring 2 only (blue) and all electrodes disconnected (red). The shaded boxes represent the location of the electrodes.

Above a threshold electric field, approximately 60.5 V/m, a localized electrostatic wave can been seen in the density fluctuations. Figure 4.2 shows a typical power spectrum of a time series taken from one of the tips of the double probe biased into ion saturation. Since these are steady state measurements, we can assume constant temperature. Under these considerations, ion saturation fluctuations are a measurement of density fluctuations. As can be seen, the mode exhibits the characteristic "spiky" structure of IEDDI with a peak frequency below the ion cyclotron frequency $f/f_{ci} \approx 0.84$, and the observed fluctuations are broadband $\Delta f/f_0 \approx 0.10$.

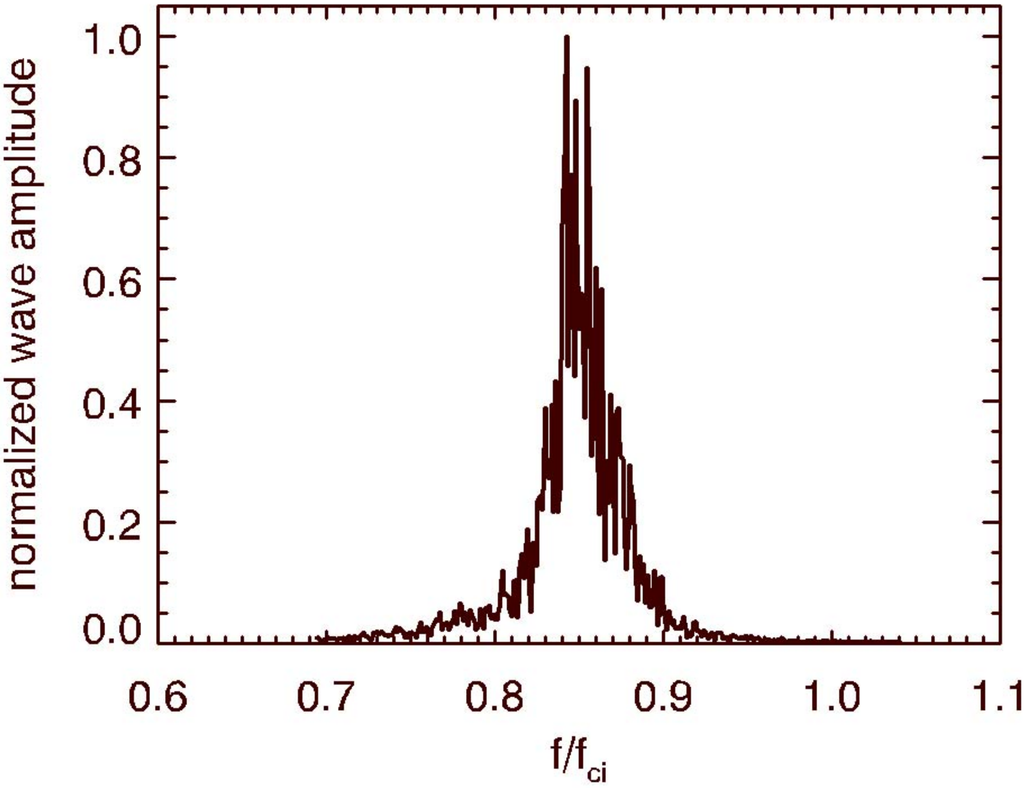

Figure 4.2: A typical power spectrum from time series of density fluctuations.

A radial scan of density fluctuations yields the magnitude of the radial wave packet, as shown in Figure 4.3. Normalized density fluctuations $\delta n/n$ are plotted as a function of radial position in blue. The density fluctuations δn were determined by taking the standard deviation of the time series about the mean value, which is proportional to the density n. The normalized shear frequency $\frac{1}{\Omega_i}\frac{\partial v_E}{\partial x}$ is plotted in red, where the slab $\mathbf{E}\times\mathbf{B}$ drift has been used to estimate the azimuthal flow. It can be seen that the peak in the density fluctuations is spatially localized to the region where the velocity shear is large and negative as predicted by the theory.

The wave vector components of the electrostatic wave were determined by using the phase of the Fourier transform of the cross-correlation of two time series of density fluctuations from spatially separated probes. Figure 4.4 shows the magnitude (top) and phase (bottom) of the Fourier transform of the cross-correlation from the two tips of the double probes. We fit a Lorentzian distribution to the region around the peak amplitude in the cross-correlation magnitude. The Lorentzian used in the fit is defined as:

$$p(f) = a\left(\frac{b^2}{(f-f_0)^2+b^2}\right)+c, \tag{4.1}$$

where we have amplitude a, half-width at half maximum b, peak frequency f_0, and offset c. We use the full width at half maximum $2b$ to window the phase function. The average and standard deviation of the phase within that window are taken as the phase shift and error respectively. We

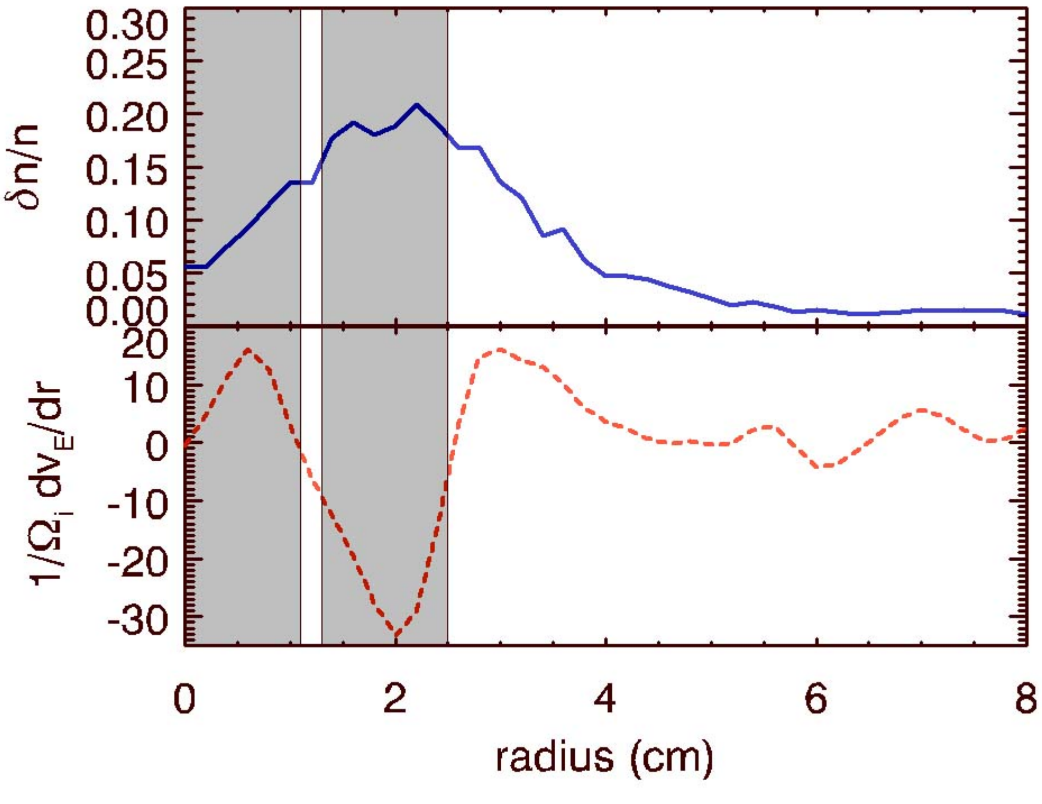

Figure 4.3: A plot of a radial scan of density fluctuations (top) and normalized shear frequency (bottom).

apply this technique to density fluctuation signals from one of the biased electrodes and one of the Langmuir probe tips on the axial translation stage as we move the probe in z. We expect a linear variation of the phase shift as a function of z, and the slope of a linear fit to the data yields the wave vector component in the $\hat{z}$-direction. Figure 4.5 (a) shows a typical measurement of $k_z = 1.25 \pm 0.08\ \mathrm{m}^{-1}$.

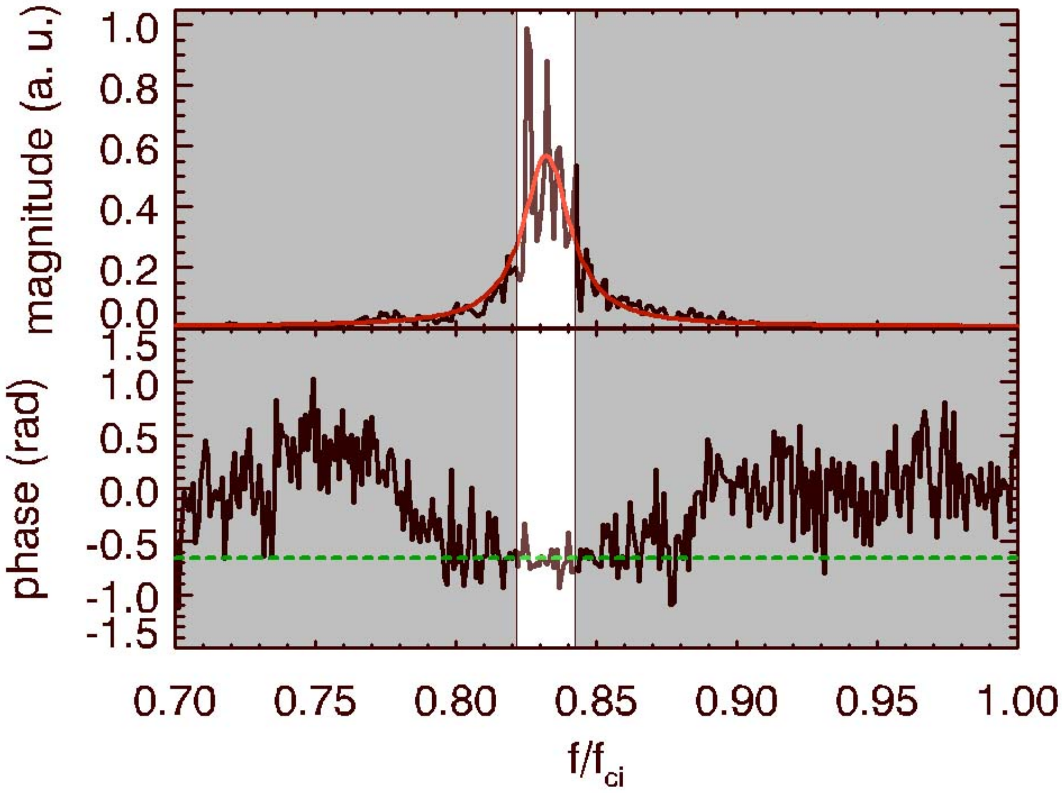

Figure 4.4: Illustration of the phase correlation method used to determine wave vector components, showing (top) cross-correlation magnitude with Lorentzian fit (red) and (bottom) phase showing average value (green) over indicated window (white region).

Applying the same technique to density fluctuation signals from the double probe tips as we rotate the double probe at the radial location of peak wave amplitude, we can determine the azimuthal component of the wave vector. Assuming the axial and azimuthal wavelengths are longer than the separation between the probe tips, we can write the following expression for the measured phase shift between the probe tips:

$$\Delta\phi = k_y d \sin\alpha + k_z d \cos\alpha, \tag{4.2}$$

where α is the angle of the double probe plane relative to the magnetic field and d is the separation between the probe tips. Since the axial wavelength is much longer than the probe separation, the contribution to the phase from the second term of Equation (4.2) is smaller than the error in the phase measurement making this term negligible for this analysis. Figure 4.5 (b) is a typical measurement of the transverse wave number, and a least-squares fit of $a \sin\alpha$ to the data. For this measurement, the probe was positioned at the location of peak wave amplitude, $r = 2.2$ cm. The best fit coefficient for the case shown is $a = -1.34$ and the probe separation is $d = 2.8$ cm, which results in $k_y = -48 \pm 6$ m^{-1}. Radial scans of k_y show a sign reversal as we cross zero, which is indicative of azimuthal propagation. The azimuthal wave number can be written as $k_\theta = m/r$, where m is the azimuthal mode number and r is the radial position. If we set our measurement of $k_y = k_\theta$, we calculate an azimuthal mode number of $|m| = 1.06 \pm 0.13$. Careful analysis of the phase shifts show that the wave propagates in the $-\hat{\theta}$-direction, which is the direction of $\mathbf{E}\times\mathbf{B}$ drift. The results are consistent with the previous experiments, which measured a primarily azimuthally

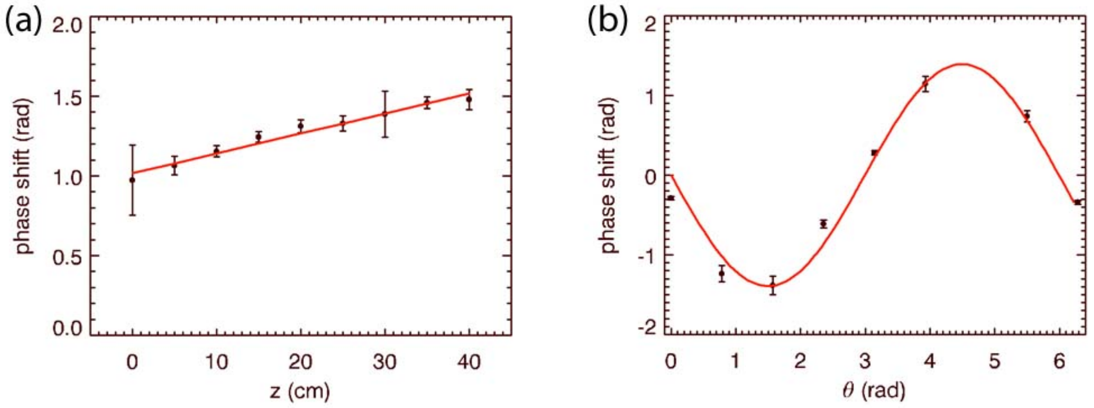

Figure 4.5: Example measurements of k_z (a) and k_θ (b).

propagating mode that propagates in the direction of the $\mathbf{E} \times \mathbf{B}$ drift, which is necessary for the Doppler-shifted frequency to be resonant with the ion cyclotron frequency.

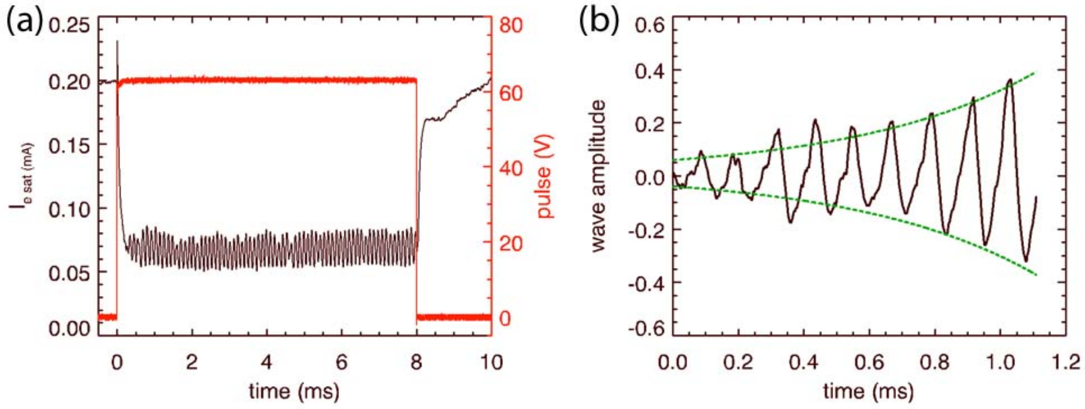

Figure 4.6: Plot (a) shows the pulse applied to the annulus (red) and the resultant electron saturation current showing growth of waves (black). Plot (b) shows a small portion of the electron saturation current (black) in part (a) with the average value subtracted off. The dashed green lines are the exponential envelope illustrating the wave growth.

We measured the growth rate for the instability with a series of experiments where the potential on the outer ring was pulsed. For the case plotted in Figure 4.6, the pulse had an amplitude of 60 V, which is above the threshold for the instability, and a period of 8 ms, which is long enough to ensure saturation of the mode. Figure 4.6 (a) shows the pulse in red and the current collected by a probe biased into electron saturation, approximately 93 V, in black as functions of time. The density depletion, caused by the electron current collected by the biased ring, develops at a characteristic time of 0.1 ms, which is the transit time to cross the distance from the rings to the probe, 20 cm, at the ion sound speed, $c_s = 2690$ m/s. At approximately 0.23 ms after the rising edge of the pulse, the density cavity and the electric field have developed, and the waves begin to grow. We take half the distance between each peak and trough as the amplitude and the average time between each peak and trough as the time associated with the amplitude. We fit a growing exponential to this data of the form $a\exp(\gamma t)$, where γ is the growth rate. Figure 4.6 (b) shows the result of applying this fit to the data in part (a). The dotted red line is the best fit and the dashed green line is the exponential envelope illustrating the growth of the instability. Every measurement of the growth rate is a result of the average of the γ determined from 25 time series. Applying this technique the growth rate of the electrostatic mode was $\gamma = 1840 \pm 90$ rads, equivalently $\gamma = 0.03\Omega_i$.

4.2 Electromagnetic Mode Characteristics

Plasma $\beta = \frac{nkT}{B^2/2\mu_0}$ is a measure of the ability of the plasma to modify the background magnetic field, as is necessary for the fluctuating magnetic field of an electromagnetic plasma wave. If the Alfvén velocity $v_A = B/\sqrt{\mu_0 n m_i}$ is less than the electron thermal speed $v_{Te} = \sqrt{2T_e/m_e}$, kinetic Alfvén waves will propagate in the medium. In the opposite limit, the waves will be inertial Alfvén waves. The requirement for a kinetic Alfvén wave can be expressed as $\beta > m_e/m_i$. As Table 4.1 shows, the previous electrostatic experiments were conducted at values of β much less than the ratio of the electron to ion mass ratio m_e/m_i. Under these conditions, any magnetic fluctuations would be very difficult to detect. The plasma β in the current experiments can be varied from $0.07\, m_e/m_i < \beta < 3.73\, m_e/m_i$.

Above a threshold electric field, approximately 60.5 V/m, we measure magnetic fluctuations in addition to the electrostatic fluctuations. Figure 4.7 shows a typical power spectrum of the magnetic fluctuations seen in the experiment. The power spectrum of the magnetic fluctuations displays the same characteristics as the electrostatic fluctuations, including the "spiky" nature of the instability with a peak near the cyclotron frequency and the mode is broadband $\Delta f/f_{ci} = 0.10 - 0.15$. The amplitudes of the wave magnetic field components are roughly equal, with the total magnetic field fluctuation amplitude $B_1 \approx 0.25\ \mu$T. The wave electric field can be approximated using the measured electrostatic wave potential as $E_1 = k\phi_1 \approx 2$ V/m. The contribution to the electric field from the time varying vector potential can be estimated by $-\frac{\partial A_1}{\partial x} \approx \frac{\omega}{k} B_1 < 7 \times 10^{-4}$ V/m. This resulted in an E_1/B_1 ratio of approximately ten times the Alfvén speed.

Figure 4.8 shows a comparison of radial profiles of normalized wave amplitude for the electrostatic (dashed line) and electromagnetic fluctuations (solid line). The outer electrode was biased to 150 V relative to chamber ground, while the center disk was disconnected. Both profiles indicate a spatial localization to regions of strong velocity shear, where the inhomogeneous electric field

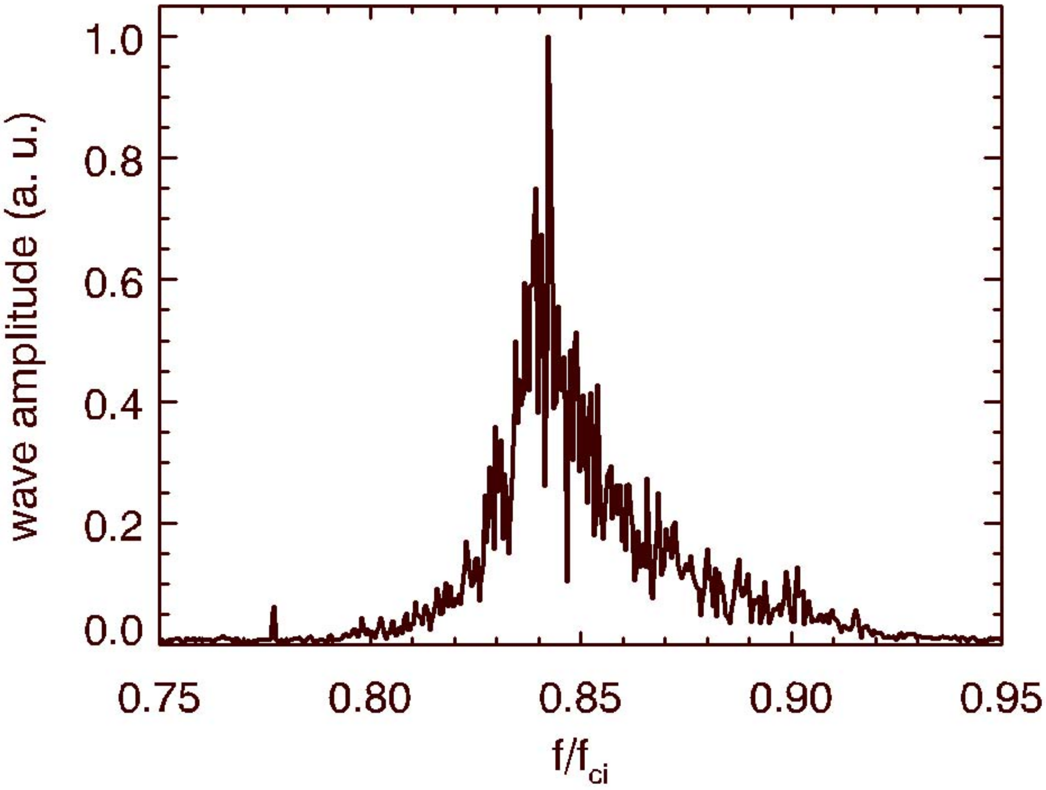

Figure 4.7: Typical power spectrum of the magnetic fluctuations seen in the experiment.

was present. However, the electromagnetic profile shows significant wave power outside the shear layer.

The phase shift between magnetic fluctuations detected by two spatially separated magnetic probes was determined as described in the previous section using the Fourier transform of the cross-correlation function. The measurement of the axial wave number was made by fitting a line to three unequally spaced axial phase shift measurements at the center of the chamber. The least-squares fit indicated a propagation direction parallel to B with $k_z = 0.05 \pm 0.007$ cm^{-1}. The measurement of the azimuthal component of the wave number was made between two magnetic probes that could be translated radially and separated by 90 degrees in the azimuthal direction. The two probes were scanned radially, recording the measured phase shifts. The phase shifts were constant and approximately equal to $\pi/2$, as shown in Figure 4.9. These measurements

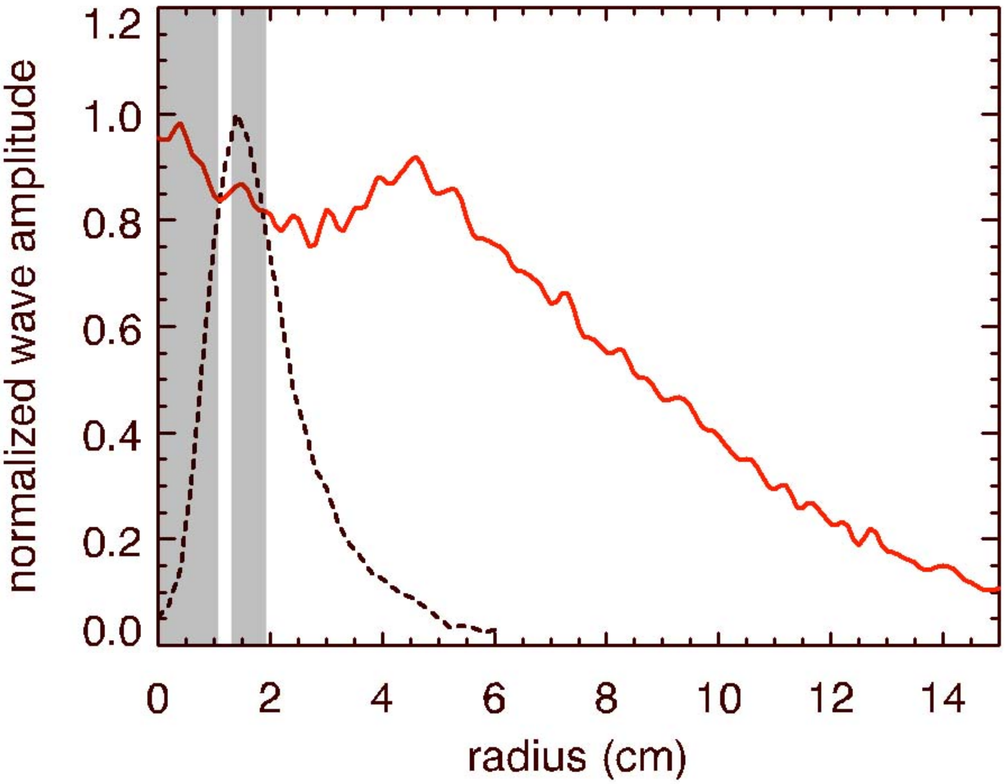

Figure 4.8: Profiles of normalized wave amplitude as a function of radial position are shown, where the dashed line and the solid line depict the electrostatic ($\delta n/\delta n_{max}$) and electromagnetic ($\delta B/\delta B_{max}$) fluctuations respectively. The shaded regions indicate the positions of the electrodes.

of the azimuthal mode number are consistent with an $m = 1$ cylindrical mode, rotating in the direction of the azimuthal flow. The measurement of the wave number components are consistent with a primarily azimuthally propagating electromagnetic wave with a radial eigenmode structure as expected for the instability under study. The normalized amplitude for the electromagnetic fluctuations are plotted as a green dashed line to lend context to the profile. The linearly increasing region is outside the main plasma column and far out on the tail of the radial eigenmode.

When the electrodes are biased, magnetic field-aligned current and density gradients are established in addition to the radial electric field. Care must be taken to identify the source of the free energy that is driving the observed instability. The measurements of the field-aligned current also show an oscillating current up to approximately $I = 3.3$ mA due to the electrostatic mode.

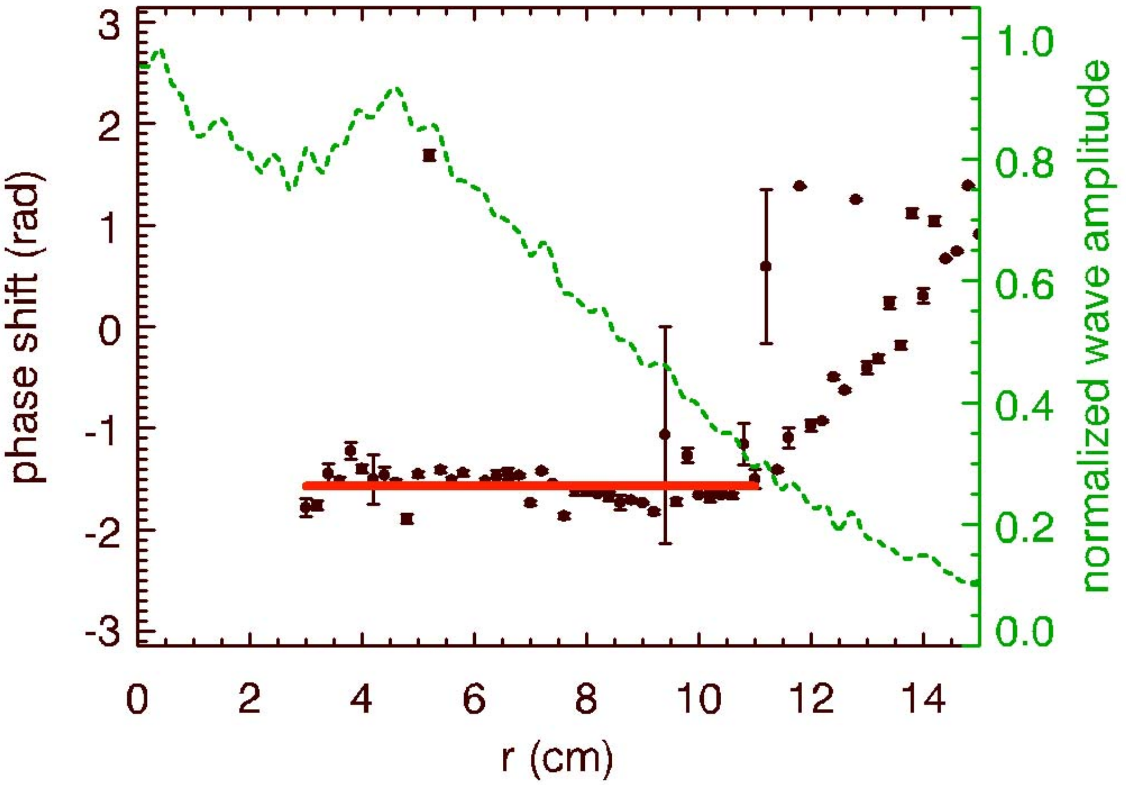

Figure 4.9: Phase shift between two magnetic probes separated by $\pi/2$ azimuthally while both probes are scanned together radially. The solid red line is at a phase shift equal to -$\pi/2$, which is the phase shift expected for an $m = 1$ cylindrical mode propagating in the direction of the azimuthal flow. The normalized amplitude for the electromagnetic fluctuations (green dashed line) is plotted to give context to the phase shift profile.

As a zeroth order sanity check, we imagine this current flowing through an infinitesimal wire, and compute the magnitude of the oscillating magnetic field produced by this wire. The resulting magnetic field magnitude is $B = \mu_0 I/(2\pi r)$. An oscillating current of 3.3 mA would produce an oscillating magnetic field on the order of the observed magnetic fluctuations only when within a few millimeters of the oscillating current. The observed local maxima in the magnetic fluctuations are too far from the field-aligned current for the magnetic fluctuations to be caused merely by this oscillating current.

The parallel electron drift velocity was estimated from measurements of the maximum field-aligned current collected by the electrodes. Assuming that the field-aligned current profile was uniform, we can use the expression for the ion saturation current collected by a biased Langmuir probe to estimate the electron drift velocity, $I = enAv_d$ [24], where e is the charge on the electron, n is the bulk plasma density, A is the electrode area, and v_d is now the drift velocity of the electrons. Under these assumptions, the maximum electron drift velocity was found to be $v_d \approx 16$ km/s. The theory incorporating the effects of collisions on the current-driven ion cyclotron instability were presented in a paper by *Satyanarayana et al.* [88]. In the weakly collisional limit where $\nu_i/\Omega_i < 1$ and $\nu_e/(k_\| v_{te})$, the critical drift velocity v_c is given by:

$$\frac{v_c}{v_{te}} = \frac{\omega_r}{k_\| v_{te}} + \frac{\tau \Gamma_1}{\sqrt{\pi}} \left[1 - \frac{\nu_e \sqrt{\pi}}{k_\| v_{te}} \right] \left(\frac{\nu_i}{\omega_r - \Omega_i} \right) \left(1 + \frac{\omega_r \Gamma_1}{\omega_r - \Omega_i} \right), \tag{4.3}$$

where ν_e and ν_i are the electron-neutral and ion-neutral collision frequencies, v_{te} is the electron thermal speed, τ is the electron to ion temperature ratio, and $\Gamma_1 = I_1(k_\perp \rho_i/2) \exp{(k_\perp \rho_i/2)}$, where I_1 is the modified Bessel function of first order and ρ_i is the ion gyroradius. The resultant critical drift velocity is $v_c \approx 550$ km/s for our experimental parameters, which is more than 30 times larger than the estimated electron drift in the experiment. The observed mode cannot be current driven.

Distinguishing between the density gradient and the inhomogeneous electric field as the source of free energy requires a bit more care, since the density gradient and the largest gradient in the electric field occur at the same radial location. In Figure 4.10, the top panel shows the normalized magnetic (solid) and electrostatic (dashed) fluctuation amplitudes as a function of radius. The bottom panel shows the normalized shear frequency (solid) $\omega_s = \frac{1}{\Omega_i}\frac{\partial v_E}{\partial r}$ and the normalized density gradient (dashed) $\delta_e \frac{\partial \ln{(n)}}{\partial r}$ as a function of radius, where $\delta_e = c/\omega_{ce}$ is the electron skin depth. The normalized shear frequency is much larger than the normalized density gradient, which suggests that the sheared flows are the dominant source of free energy.

We examine the behavior of the electric field and the density gradient near the threshold for the wave. Figure 4.11 shows a plot of the normalized mode amplitude (solid line) as a function of the bias applied to the outer electrode. A comparison of the fractional change in the electric field (filled circles) and the density gradient (open triangles) as functions of bias demonstrates a clear

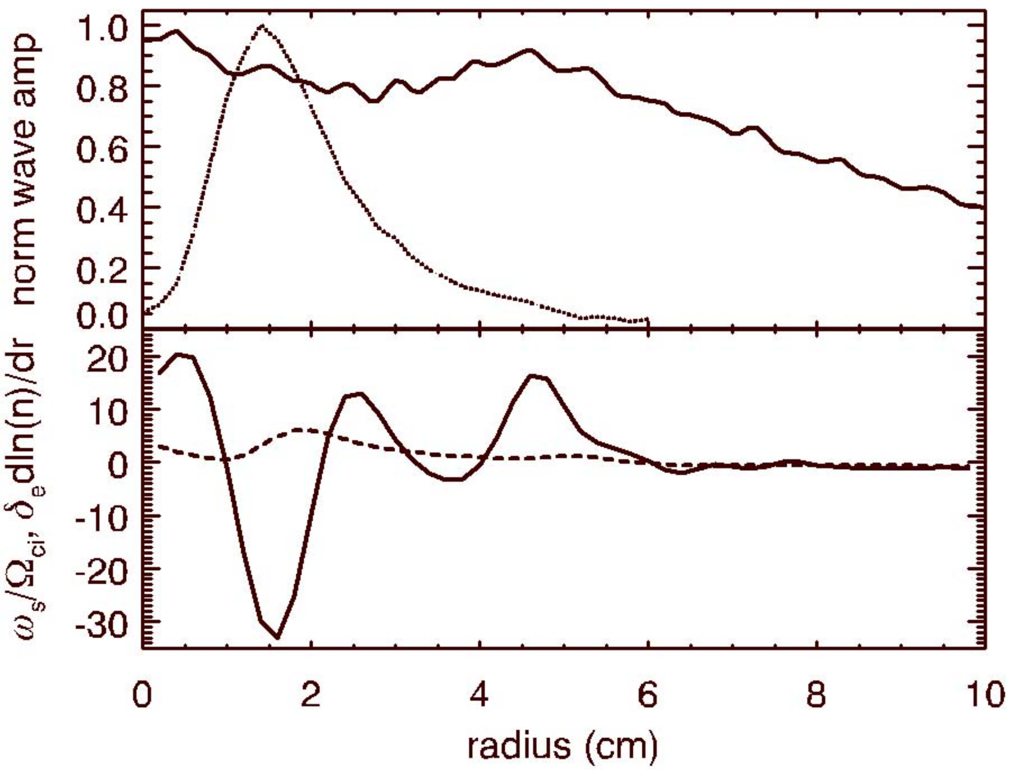

Figure 4.10: The solid and dashed lines in the top plot are the radial profiles of the normalized magnetic and electrostatic fluctuation amplitude respectively. The bottom plot shows radial profiles of shear frequency (solid) and normalized density gradient (dashed).

correlation between the growth of the mode and the electric field. The reference values at threshold are $E_0 = 60.5$ V/m and $(\partial \ln n/\partial r)_0 = 19.5$ m^{-1}. As the wave amplitude changes rapidly above threshold, the electric field changes by a factor of 4 while the density gradient remains fairly constant. This clearly indicates that the electric field and hence the sheared flows are responsible for driving the observed waves, not the density gradients. Furthermore, the expected frequencies for drift waves are much higher than the observed frequencies. At the maximum of the electrostatic signal, the diamagnetic drift frequency is $\omega_* = -k_\theta \frac{k_B T_e}{eB_0} \frac{\partial \ln n}{\partial r} = -5.9\Omega_{ci}$, which is well above the observed frequency. In addition, the observed wave propagates in the direction of the $E \times B$ drift and not the electron diamagnetic drift direction.

In order to further test whether the electromagnetic wave and the electrostatic wave are created by the same shear-driven instability, a bias scan of the outer electrode was conducted. Changing the bias on the electrodes changed the radial electric field and thus the flow shear, which resulted in a different frequency for the observed mode. The inset in Figure 4.11 shows that the frequency of the electromagnetic wave (open squares) tracks the frequency of the electrostatic wave (filled circles).

4.3 Beta Dependence

A common and often difficult problem associated with using magnetic probes to measure oscillating magnetic fields is the possibility of capacitive pickup contaminating the inductive electric field being measured. A variety of techniques were used to minimize these effects, including electrostatic shielding of the coils and the use of differential amplifiers. It is important to verify that the magnetic fluctuations that were measured are indeed a result of an inductive electric field an not electrostatic pickup. For a stringent test, we can make use of the fact that as the plasma beta is decreased, electromagnetic effects are diminished.

A series of scans were performed, changing the plasma β by scanning the RF power used to produce the plasma. Varying the RF power results in changes to both the density and the electron temperature, both of which will affect the plasma β. The density and electron temperature in

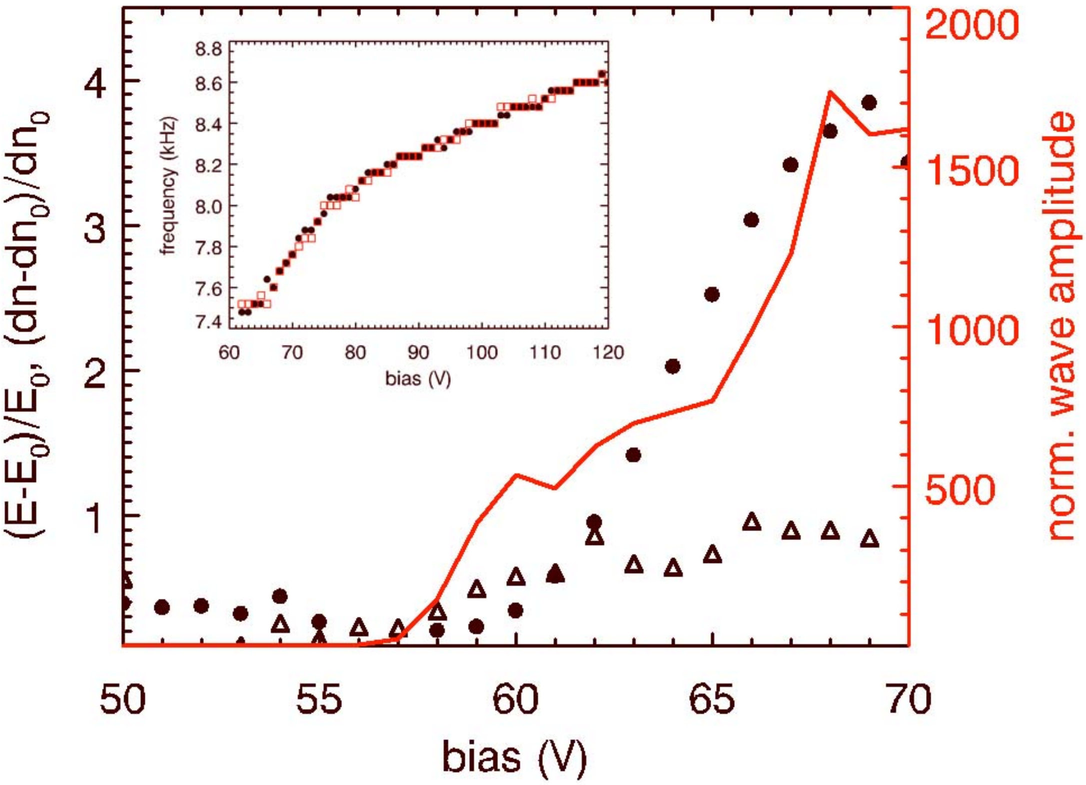

Figure 4.11: Normalized wave amplitude (solid line), fractional electric field (filled circles), $(E - E_0)/E_0$, where $E_0 = 60.5$ V/m, and fractional density gradient (open triangles), $(\partial \ln n/\partial r - (\partial \ln n/\partial r)_0)/(\partial \ln n/\partial r)_0$, where $(\partial \ln n/\partial r)_0 = 19.5\ \mathrm{m}^{-1}$, as a function of applied ring bias. The inset is a plot of observed frequency as a function of the applied electrode bias: peak frequency of electrostatic fluctuations (filled circles) within the shear layer and magnetic fluctuations (open squares) at the edge of the plasma column.

an inductively coupled plasma are functions of magnetic field, background gas pressure, and RF power, however, for conditions during this scan, β varied approximately as a linear function of the applied RF power.

Figure 4.12 shows an RF power scan of β for a magnetic field of 300 G. The electrostatic wave amplitude is shown as green circles, while the electromagnetic wave amplitude is shown as red circles. Both amplitudes exhibit a three order of magnitude change for a relatively small range of β. The most important feature to note in Figure 4.12 is that the electromagnetic wave amplitude decreases by a factor of approximately 1000 while the electrostatic wave amplitude decreases by less than a factor of 2. This situation would not be possible if the magnetic fluctuation signal is merely due to electrostatic pickup. The voltage fluctuations detected by the magnetic loop are induced by a changing magnetic field, and those magnetic fluctuations behave appropriately as a function of β. However, the apparent β threshold is in reality due to the sensitivity of the magnetic probe and the inherent noise in the system.

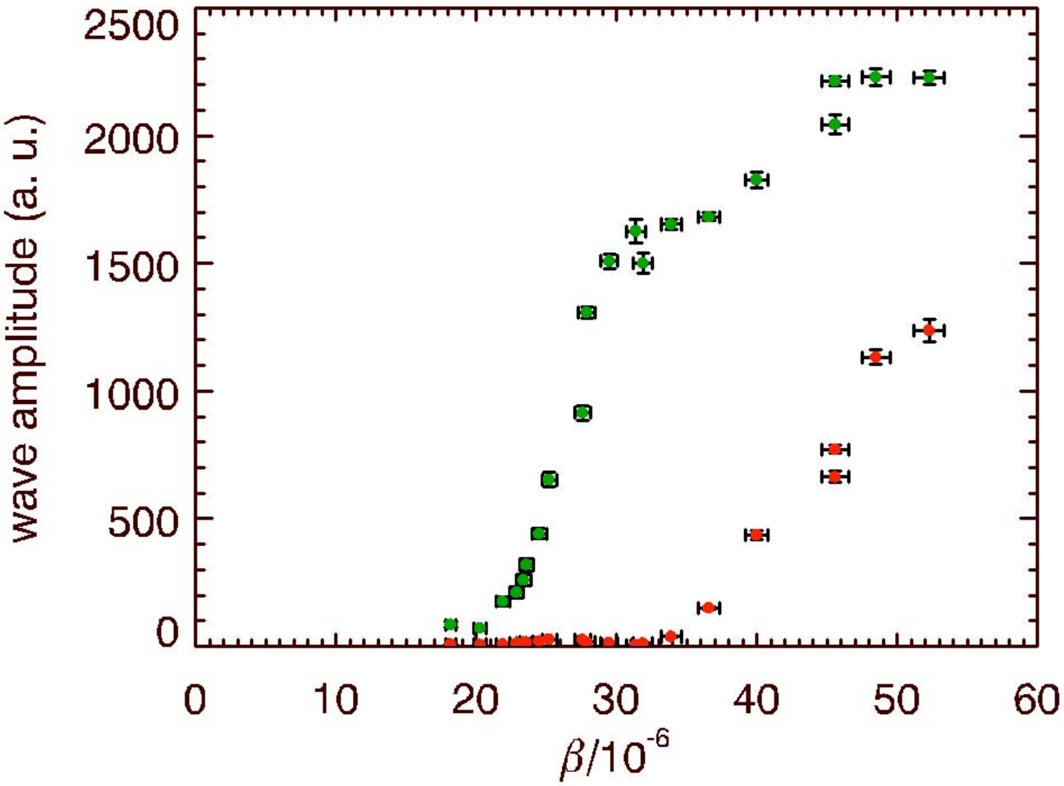

Figure 4.12: Electrostatic (green circles) and electromagnetic (red circles) wave amplitude (not to scale) as a function plasma β. Electromagnetic wave amplitude decreases as β decreases, while a significant electrostatic wave power remains.

These RF power scans were repeated for a range of magnetic field values, 300-600 G. The general behavior remained the same with the amplitude of the magnetic fluctuations decreasing with decreasing β while the electrostatic fluctuation amplitude remained large. Figure 4.13 examines the data set from the perspective of a constant applied RF power and varying background magnetic field. For a given RF power, the magnetic fluctuation amplitude decreases as the background magnetic field is increased. For the background magnetic field value where the magnetic fluctuation amplitude decreases to the noise floor, the value of β was computed and plotted as a function of the applied RF power. The value of β that reduces the magnetic field amplitude below the detectable level for our probes is a constant value, $1.66 \pm 0.34 \times 10^{-5}$.

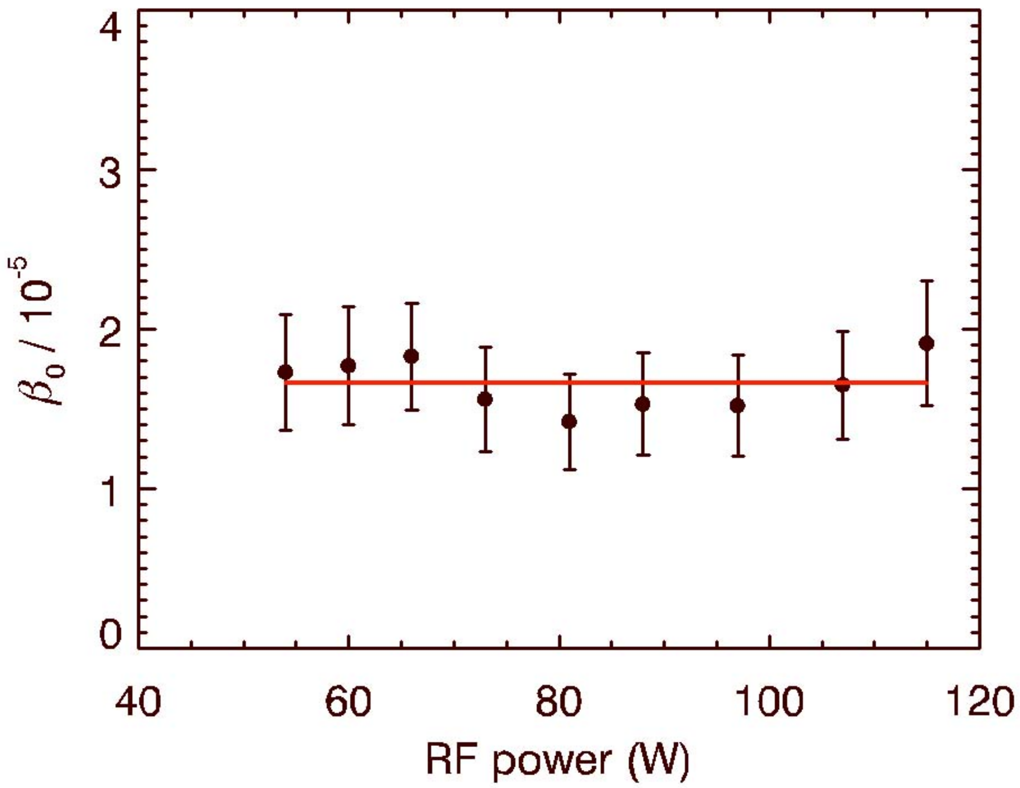

Figure 4.13: The value of β (black circles) at which the magnetic fluctuation amplitude decreases to the noise floor as a function of the applied RF power with a linear fit (solid red line) to the data.

4.4 Theory Comparison

There are two interesting experimental observations that we can directly compare to predictions from the theoretical model discussed in Chapter 2. The first is the velocity shear-modified Alfvén wave dispersion relation given in Equation (2.80). The second is the difference in width

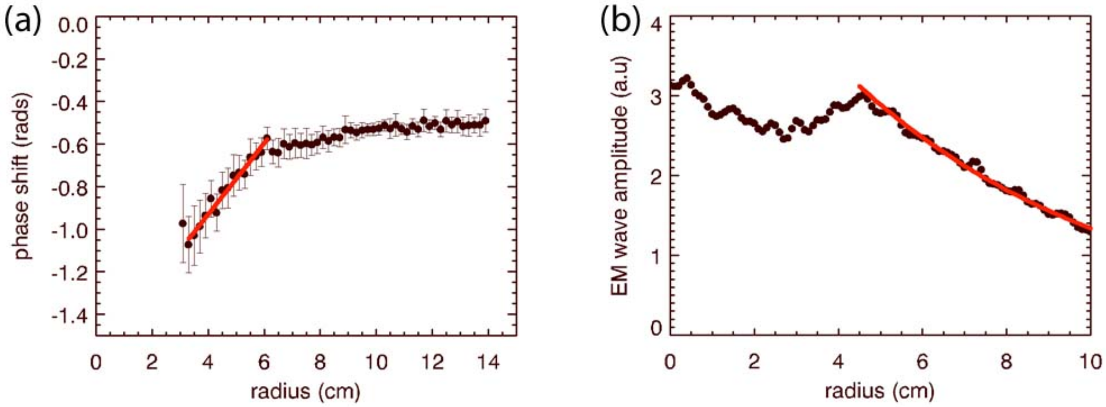

Figure 4.14: Determination of the real (a) and imaginary (b) parts of the average radial wave vector. The real part is determined from the slope of a linear fit to phase shift data as a function of the radial separation between two probes. The imaginary part is determined from a fit of the exponential decay of the radial eigenmode.

of the radial eigenmodes for the electrostatic and electromagnetic fluctuations shown in Figure 4.8. As we will show, the derived model captures some of the essential physics of the instability observed in the experiment.

In order to see if the observations are consistent with the velocity shear-modified Alfvén wave dispersion relation, Equation (2.80), we first need to determine a complex averaged k_x. Figure 4.14 illustrates how the real and imaginary parts of k_r were determined from the experimental measurements. The slope of a linear fit to the phase shift between two magnetic probes as a function of the radial distance between them yields the real part of $k_r = 0.168$ cm^{-1}, Figure 4.14 (a). A least squares fit to the electromagnetic wave amplitude profile of the form $A\exp[i\kappa r]$, yields the imaginary part of k_r, $\kappa = -0.15$ cm^{-1}, Figure 4.14 (b). We fit data in different spatial regions, because the dominant real k_r should occur near the peak amplitude but the imaginary part will manifest itself in the decay of the profile.

We use the measured, complex value of k_r as an estimate for our spatially averaged quantity k_x used in Equation (2.80). Using the experimentally measured plasma parameters, complex k_x, and electric field, we can make plots of γ/ω from Equation (2.80) as a function of k_z. The results are plotted (solid line) in Figure 4.15, where the dashed lines are the upper and lower bound due to the

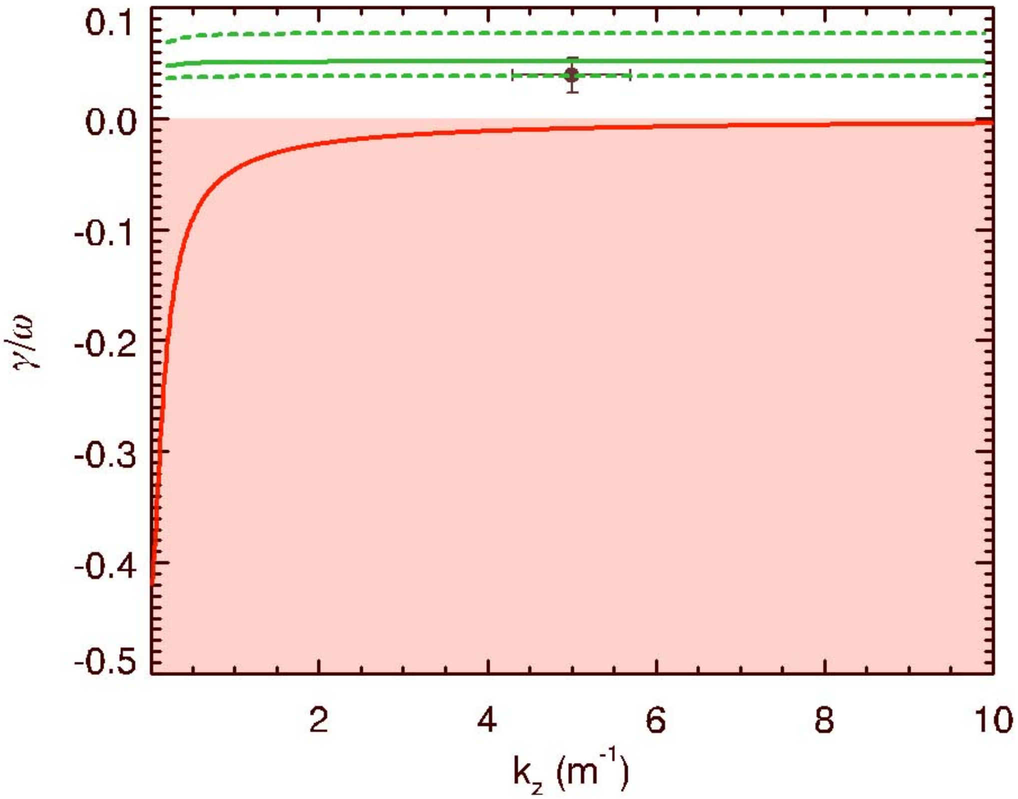

Figure 4.15: Growth rate divided by real frequency as a function of k_z for Equation (2.80) including sheared flow (green) with upper and lower bound due to the error in the measured E (dashed) and a similar plot for shear Alfvén waves from homogeneous plasma theory (red), which are damped for all values of k_z plotted here. Experimental observations appear in the shaded box.

error in the measured E. The black circle represents the observed values incorporating the spectral width of the mode and the error in k_z measurement. For comparison, the red line is the solution for shear Alfvén waves from homogeneous plasma theory, which leads to damped modes. Even when considering the effects of electron Landau damping, the instability has a positive growth rate in the presence of sheared flows for much larger values of k_z than would be expected from homogeneous plasma theory. The observations are consistent with the predictions from velocity-shear modified dispersion relation.

The radial eigenfunctions shown in Figure 2.1 allow us to predict the radial profile of the electrostatic ϕ_1 and electromagnetic fluctuations $\mathbf{B}_1 = \nabla \times \mathbf{A}_1$. Using the Coulomb gauge $\nabla \cdot \mathbf{A}_1 =$

0 and the definition of the electric field

$$\mathbf{E}_1 = -\nabla \phi_1 - \frac{\partial \mathbf{A}_1}{\partial t}, \tag{4.4}$$

we can arrive at the following differential equation for the electrostatic fluctuations in terms of the radial eigenfunctions from the simulation:

$$\frac{\partial^2 \phi_1}{\partial x^2} - \left(k_y^2 + k_z^2\right) \phi_1 = -\frac{\partial E_{1x}}{\partial x} - i k_y E_{1y} - i k_z E_{1z} \tag{4.5}$$

and the components of the vector potential:

$$\frac{\partial A_{1x}}{\partial x} = -\frac{k_y}{\omega} E_{1y} - \frac{k_z}{\omega} E_{1z} - i \left(\frac{k_y^2 + k_z^2}{\omega}\right) \phi_1 \tag{4.6}$$

$$A_{1y} = -\frac{i}{\omega} \left(E_{1y} + i k_y \phi_1\right) \tag{4.7}$$

$$A_{1z} = -\frac{i}{\omega} \left(E_{1z} + i k_z \phi_1\right). \tag{4.8}$$

The results of these calculations have been plotted in Figure 4.16, where we have taken the curl of the vector potential to get B_1. The dashed black line is the fluctuating electrostatic potential and the solid red line is the magnitude of the magnetic fluctuations as functions of position normalized to the size of the flow layer. The full-width at half-maximum of $|\mathbf{B}_1|$ is approximately 3 times larger than the full-width at half-maximum of ϕ_1. This is consistent with the experimental observations, where the corresponding ratio is approximately 5. This indicates that the theory predicts the localization of the electrostatic fluctuations to the shear layer, while the electromagnetic fluctuations extend further and have the possibility to influence the dynamics outside of the region of generation.

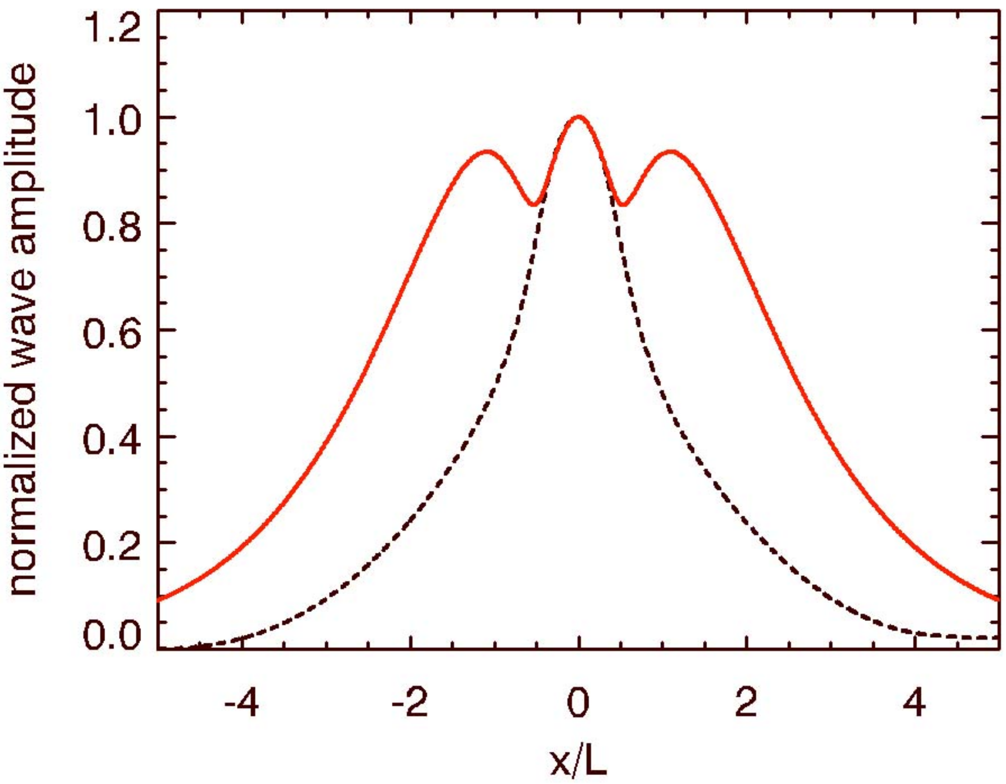

Figure 4.16: Fluctuating electrostatic potential (black dashed line) and magnitude of the magnetic fluctuations (solid red line) calculated from the eigenfunction solutions from the electromagnetic top hat from chapter 2.

Chapter 5

Conclusion

The experiments presented establish that strongly localized dc electric fields perpendicular to the ambient magnetic field can behave as a radiation source for electromagnetic ion cyclotron waves, which can transport energy away from the region of wave generation. We established a foundation for this laboratory investigation of velocity shear-driven electromagnetic ion cyclotron instabilities by reproducing the electrostatic experiments on the inhomogeneous energy density driven instability. Biasable electrodes were employed to create controllable inhomogeneous radial electric fields, which would establish the azimuthal sheared flows that would be the free energy source for the instability. We observed modes with a "spiky", broadband spectrum near the ion cyclotron frequency whose frequency shifted with applied electric field. The wave was observed to be a predominantly azimuthally propagating, $m = 1$ cylindrical wave with a radial eigenmode structure confined to the shear layer. The wave propagation is in the direction of the $\mathbf{E} \times \mathbf{B}$ drift. All of these observations are consistent with the characteristics of the previous electrostatic IEDDI experiments.

Once this foundation was firmly established, we used the magnetic loop probes to look for the presence of magnetic fluctuations. The observed magnetic fluctuations had similar frequency content to the electrostatic fluctuations. We have ruled out potential alternative sources for the observed magnetic fluctuations, i.e. oscillating parallel current and electrostatic pickup. Due to the strength and extend of the radial profile of the oscillations, the oscillating parallel current could not account for the magnetic fluctuations. Electrostatic pickup could also be ruled out due to the different behavior of the electrostatic and electromagnetic fluctuations as the plasma β was decreased. The power spectrum of the magnetic signals exhibited the same "spiky", broadband spectrum, with similar peak frequency and whose frequency shifted in the same manner with applied electric field. We measured the magnetic fluctuations to be a predominantly azimuthally propagating, $m = 1$ cylindrical wave whose radial eigenmode structure, however, extended much further than the electrostatic fluctuations. Again, the wave propagation direction was observed to be along the $\mathbf{E} \times \mathbf{B}$ drift.

The general characteristics of the electromagnetic wave are consistent with the intuition developed from studying the electrostatic mode, however, a detailed analysis of the source of free energy is required to ensure that the observed instability is driven by the sheared flows. A comparison of the estimated parallel electron drift in the experiment and the critical drift velocity for current driven instability using the weakly collisional theory, indicated that the observed parallel drift was 30 times smaller than the critical drift velocity necessary for the observed mode to be a result of a current driven instability. We considered the density gradient as another possible candidate for the source of free energy, however, the diamagnetic drift frequency in the region of interest is $\omega_* = -5.9\Omega_{ci}$, which is well above the observed frequency. In addition, the observed wave propagates in the direction of the $\mathbf{E} \times \mathbf{B}$ drift and not the electron diamagnetic drift. Near the threshold for the instability, the fraction change in the electric field and the density gradient were compared to the fractional increase in the wave amplitude. The growth of the wave was well correlated with the growth of the electric field, leading us to determine that the electric field and, hence, the flows are responsible for the growth of the instability.

As expected, the amplitude of the magnetic fluctuations decreased as the plasma β decreased. This trend was consistent regardless of whether β was modified by changing the kinetic pressure or the magnetic pressure. The amplitude of the magnetic fluctuations decreased by a factor of approximately 1000 over the relatively small range of β in the experiments. With the appropriate directional, oscillating electric field diagnostics, these β scans could result in a clear observation of the electrostatic to electromagnetic transition of this instability.

Finally, we made comparisons of the experimental observations with predictions from the present theory of Peñano and Ganguli [82]. Although, the existing theory assumes Cartesian coordinates, thereby neglecting cylindrical effect, there is compelling agreement between theory and experiment. We determined numerically that the radial profiles of the electrostatic potential and the magnetic field of the wave are consistent with those observed in the experiment, where the ratio of the full-width at half-maximum of the magnetic fluctuations to electrostatic fluctuations is approximately 5. In addition, the observed dispersion of the wave in the experiment was consistent with the velocity shear-modified Alfvén wave dispersion relation derived in the weak shear limit from the electromagnetic model and inconsistent with homogeneous shear Alfvén wave theory. However, more of the dispersion relation needs to be mapped out before the theory can be verified. It would also be beneficial to determine where warm ion effects, which are not included in the present model, begin to substantially modify the dispersion relation.

The experimental observations and the agreement with the theory lead us to conclude that we have made the first observation of electromagnetic ion cyclotron waves driven by strongly sheared plasma flows. The experimental observation of these waves and additional careful studies of their characteristics may lead to an explanation of the origins of broadband electromagnetic waves observed near auroral arcs and the resultant ion heating. In future experiments, we plan to investigate ion heating effects and the development of ion conics due to the presence of these waves.

Bibliography

[1] T. Abe, B. A. Whalen, A. W. Yau, R. E. Horita, S. Watanabe, and E. Sagawa. EXOS-D (Akebono) SMS observations of the polar wind. *J. Geophys. Res.*, 98:11191, 1993.

[2] M. J. Alport, S. L. Cartier, and R. L. Merlino. Laboratory observations of ion cyclotron waves associated with a double layer in an inhomogeneous magnetic field. *J. Geophys. Res.*, 91:1599, 1986.

[3] W. E. Amatucci. *Experimental observation of ion-cyclotron turbulence in the presence of transverse velocity shear*. PhD thesis, West Va. Univ., Morgantown, WV, 1994.

[4] W. E. Amatucci, M. E. Koepke, J. J. Carroll III, and T. E. Sheridan. Observation of ion-cyclotron turbulence at small values of magentic-field-aligned current. *Geophys. Res. Lett.*, 21(15):1595, 1994.

[5] W. E. Amatucci, D. N. Walker, G. Ganguli, J. A. Antoniades, D. Duncan, J. H. Bowles, V. Gavrishchaka, and M. E. Koepke. Plasma response to strongly sheared flow. *Phys. Rev. Lett.*, 77(10):1978, 1996.

[6] W. E. Amatucci, D. N. Walker, G. Ganguli, D. Duncan, J. A. Antoniades, J. H. Bowles, V. Gavrishchaka, and M. E. Koepke. Velocity-shear-driven ion-cyclotron waves and associated transverse ion heating. *J. Geophys. Res.*, 103(A6):11711, 1998.

[7] M. André, P. Norqvist, L. Andersson, L. Eliasson, A. I. Eriksson, L. Blomberg, R. E. Erlandson, and J. Waldemark. Ion energization mechanisms at 1700 km in the auroral region. *J. Geophys. Res.*, 103:4199, 1998.

[8] M. André and A. W. Yau. Theories and observations of ion energization and outflow in the high latitude magnetosphere. *Space Sci. Rev.*, 80:27, 1997.

[9] M. P. André, P. Norqvist, A. Vaivads, L. Eliasson, A. I. Norberg, O. Eriksson, and B. Holback. Transverse ion energization and wave emissions observed by the Freja satellite. *Geophys. Res. Lett.*, 21:1915, 1994.

[10] R. K. Arnoldy, K. A. Lynch, P. M. Kintner, S. Vago, J. Chesney, T. E. Moore, and C. J. Pollack. Bursts of transverse ion acceleration at rocket altitudes. *Geophys. Res. Lett.*, 19:413, 1992.

[11] W. I. Axford. The polar wind and the terrestrial helium budget. *J. Geophys. Res.*, 73:6855, 1968.

[12] P. M. Banks and T. E. Holzer. High-latitude plasma transport: The polar wind. *J. Geophys. Res.*, 74:6317, 1969.

[13] S. Basu, S. Basu, E. MacKenzie, P. F. Fourgere, W. R. Coley, N. C. Maynard, J. D. Winningham, M. Sugiura, W. B. Hanson, and W. R. Hoegy. Simultaneous density and electric field fluctuation spectra associated with velocity shears in the auroral oval. *J. Geophys. Res.*, 93:115, 1988.

[14] P. R. Bevington and D. K. Robinson. *Data Reduction and Error Analysis for the Physical Sciences*. McGraw-Hill, Boston, MA, second edition, 1992.

[15] M. H. Boehm, J. Clemmons, and G. Paschmann. Freja observations of a ten-meter boundary within monoenergetic auroral electron precipitation. *Geophys. Res. Lett.*, 22:69, 1995.

[16] J. Bonnell, P. M. Kintner, J.-E. Wahlund, K. Lynch, and R. Arnoldy. Interferometric determination of broadband ELF wave phase velocity within a region of transverse auroral ion acceleration. *Geophys. Res. Lett.*, 23:3297, 1996.

[17] J. W. Bonnell. *Identification of broadband ELF waves observed during transverse ion acceleration in the auroral ionosphere*. PhD thesis, Cornell, Univ., Ithaca, NY, 1997.

[18] J. E. Borovsky, D. M. Suszcynsky, M. I. Buchwald, and H. V. DeHaven. Measuring the thicknesses of auroral curtains. *Arctic*, 44:231, 1991.

[19] E. L. Bronaugh. Helmholtz coils for calibration of probes and sensors: Limits of magnetic field accuracy and uniformity. In *Proceeding of International Symposium on Electromagnetic Compatibility*, page 72, 1995.

[20] C. W. Carlson, J. P. McFadden, R. E. Ergun, M. Temerin, W. Peria, F. S. Mozer, D. M. Klumpar, E. G. Shelley, W. K. Peterson, E. Moebius, R. Elphic, R. Strangeway, C. Cattell, and R. Pfaff. FAST observations in the downward auroral current region: Energetic upgoing electron beams, parallel potential drops, and ion heating. *Geophys. Res. Lett.*, 25(12):2017, 1998.

[21] J. J. Carroll III, M. E. Koepke, W. E. Amatucci, T. E. Sheridan, and M. J. Alport. A segmented disk electrode to produce and control parallel and transverse particle drifts in a cylindrical plasma. *Rev. Sci. Instrum.*, 65:2991, 1994.

[22] C. A. Cattell, T. Nguyen, M. Temerin, W. Lennartsson, and W. K. Peterson. Effects of solar cycle on auroral particle acceleration. *Geophys. Monogr. Ser.*, 80:219, 1993.

[23] C. R. Chappell. The terrestrial plasma source: A new perspective in solar-terrestrial processes from dynamics explorer. *Rev. Geophys.*, 26:229, 1988.

[24] F. F. Chen. *Introduction to Plasma Physics and Controlled Fusion*. Plenum Press, New York, NY, second edition, 1984.

[25] F. F. Chen. Experiments on helicon plasma sources. *J. Vac. Sci. Technol. A*, 10(4):1389, 1992.

[26] N. D'Angelo. Kelvin-Helmholtz instability in a fully ionized plasma in a magnetic field. *Phys. Fluids*, 8:1748, 1965.

[27] N. D'Angelo, A. Bahnsen, and H. Rosenbauer. Wave and particle measurements at the polar cusp. *J. Geophys. Res.*, 79:3129, 1974.

[28] N. D'Angelo and R. Motley. Low frequency oscillations in a potassium plasma. *Phys. Fluids*, 6:422, 1963.

[29] N. D'Angelo and S. von Goeler. Investigation of the Kelvin-Helmholtz instability in a cesium plasma. *Phys. Fluids*, 9:309, 1966.

[30] W. E. Drummond and M. N. Rosenbluth. Anomalous diffusion arising from microinstabilities in a plasma. *Phys. Fluids*, 5:1507, 1962.

[31] G. D. Earle, M. C. Kelley, and G. Ganguli. Large velocity shears and associated electrostatic waves and turbulence in the auroral F region. *J. Geophys. Res.*, 94:15321, 1989.

[32] R. R. J. Gagné and A. Cantin. Investigation of an rf plasma with symmetrical and asymmetrical electrostatic probes. *J. Appl. Phys.*, 43(6):2639, 1972.

[33] G. Ganguli. Stability of an inhomogeneous transverse plasma flow. *Phys. Plasmas*, 5:1544, 1997.

[34] G. Ganguli, M. J. Keskinen, H. Romero, R. Heelis, T. Moore, and C. J. Pollack. Coupling of microprocesses and macroprocesses due to velocity shear: An application to the low-altitude ionosphere. *J. Geophys. Res.*, 99:8873, 1996.

[35] G. Ganguli, Y. C. Lee, and P. Palmadesso. Electrostatic ion-cyclotron instability caused by a nonuniform electric field perpendicular to the external magnetic field. *Phys. Fluids*, 28(3):761, 1985.

[36] G. Ganguli, Y. C. Lee, and P. J. Palmadesso. Kinetic theory for electrostatic waves due to transverse velocity shears. *Phys. Fluids*, 31(4):823, 1988.

[37] G. Ganguli, Y. C. Lee, P. J. Palmadesso, and S. L. Ossakow. Oscillations in a plasma with parallel currents and transverse velocity shears. In T. Chang, Crew J. B., and R. Jasperse, editors, *Physics of Space Plasmas (1988), SPI Conf. Proc. Reprint Ser. Vol. 8*, page 231, Cambridge, MA, 1989. Scientific.

[38] G. Ganguli, P. Palmadesso, and Y. C. Lee. A new mechanism for excitation of electrostatic ion cyclotron waves and associated perpendicular ion heating. *Geophys. Res. Lett.*, 12(10):643, 1985.

[39] V. Gavrishchaka, M. E. Koepke, and G. Ganguli. Dispersive properties of a magnetized plasma with a field-aligned drift and inhomogeneous transverse flow. *Phys. Plasmas*, 3(8):3091, 1996.

[40] V. V. Gavrishchaka. *Collective phenomena in a magnetized plasma with a field-aligned drift and inhomogeneous transverse flow*. PhD thesis, West Va. Univ,, Morgantown, WV, 1996.

[41] V. V. Gavrishchaka, S. B. Ganguli, and G. I. Ganguli. Origin of low-frequency oscillations in the ionosphere. *Phys. Rev. Lett.*, 80:728, 1998.

[42] V. V. Gavrishchaka, M. E. Koepke, J. J. Carroll III, W. E. Amatucci, and G. Ganguli. Frequency range and spectral width of waves associated with transverse velocity shear. In J. L. Horwitz, N. Singh, and J. L. Burch, editors, *Cross-Scale Coupling in Space Plasmas, Geophys. Monogr. Ser. Vol. 93*, page 81, Washington, DC, 1995. AGU.

[43] V. V. Gavrishchaka, M. E. Koepke, and G. Ganguli. Ion cyclotron modes in a two-ion-component plasma with transverse-velocity shear. *J. Geophys. Res.*, 102:11653, 1997.

[44] D. A. Gurnett, R. L. Huff, J. D. Menietti, J. L. Burch, J. D. Winningham, and S. D. Shawhan. Correlated low-frequency electric and magnetic noise along auroral field lines. *J. Geophys. Res.*, 89:8971, 1984.

[45] N. Hershkowitz. *Plasma Diagnostics*, chapter 3 How Langmuir Probes Work, pages 113–183. Academic Press, Inc., Boston, MA, 1989.

[46] J. H. Hoffman and W. H. Dobson. Light ion concentrations and fluxes in the polar regions during magnetically quiet times. *J. Geophys. Res.*, 85:626, 1980.

[47] B. Hultqvist. On the origin of the hot ions in the disturbed dayside magnetosphere. *Planet Space Sci.*, 31:173, 1983.

[48] D. L. Jassby. Transverse velocity shear instabilities within a magnetically confined plasma. *Phys. Fluids*, 15:1590, 1972.

[49] M. C. Kelley and C. W. Carlson. Obervations of intense velocity shear and associated electrostatic waves near an auroral arc. *J. Geophys. Res.*, 82(16):2343, 1977.

[50] R. F Kemp and J. M. Sellen. Plasma potential measurements by electron emissive probes. *Rev. Sci. Instrum.*, 37:455, 1966.

[51] G. I. Kent, C. Jay, and F. F. Chen. Transverse Kelvin-Helmholtz instability in a rotating plasma. *Phys. Fluids*, 12:2140, 1969.

[52] M. J. Keskinen, H. G. Mitchell, J. A. Fedder, P. Satyanarayana, S. T. Zalesak, and J. D. Huba. Nonlinear evolution of the Kelvin-Helmholtz instability in the high latitude ionosphere. *J. Geophys. Res.*, 93:137, 1988.

[53] J. M. Kindel and C. F. Kennel. Topside current instabilities. *J. Geophys. Res.*, 76:2055, 1971.

[54] P. M. Kintner, J. Bonnell, R. Arnoldy, K. Lynch, C. Pollock, and T. Moore. SCIFER - Transverse ion acceleration and plasma waves. *Geophys. Res. Lett.*, 23:1873, 1996.

[55] P. M. Kintner, J. Franz, P. Schuck, and E. Klatt. Interferometric coherency determination of wavelength or what are broadband ELF waves? *J. Geophys. Res.*, 105:21237, 2000.

[56] Ö. Kivanç and R. Heelis. On relationships between horizontal velocity structure and thermal ion upwellings at high latitudes. *Geophys. Res. Lett.*, 26(13):1829, 1999.

[57] E. M. Klatt, P. M. Kintner, C. E. Seyler, K. Liu, E. A. MacDonald, and K. A. Lynch. SIERRA observations of alfvénic processes in the topside auroral ionosphere. *J. Geophys. Res.*, 110:A10S12, 2005.

[58] D. M. Klumpar. Transversely accelerated ions: An ionospheric source of hot magnetospheric ions. *J. Geophys. Res.*, 84:4229, 1979.

[59] D. J. Knudsen and J.-E. Wahlund. Core ion flux bursts within solitary kinetic alfvén waves. *J. Geophys. Res.*, 103:4157, 1998.

[60] M. E. Koepke, W. E. Amatucci, J. J. Carroll III, V. Gavrishchaka, and G. Ganguli. Velocity-shear-induced ion-cyclotron turbulence: Laboratory identification and space applications. *Phys. Plasmas*, 2(6):2523, 1995.

[61] M. E. Koepke, W. E. Amatucci, J. J. Carroll III, and T. E. Sheridan. Experimental verification of the inhomogeneous energy-density driven instability. *Phys. Rev. Lett.*, 72(21):3355, 1994.

[62] K. Levenberg. A method for the solution of certain non-linear problems in least squares. *Quar. Appl. Math.*, 2:164, 1944.

[63] M. Lockwood, M. O. Chandler, J. L. Horowitz, J. H. Waite Jr., T. E. Moore, and C. R. Chappell. The cleft ion fountain. *J. Geophys. Res.*, 90:9736, 1985.

[64] M. Lockwood and J. E. Titheridge. Ionopsheric origin of magnetospheric o^+ ions. *Geophys. Res. Lett.*, 8:381, 1981.

[65] M. Lockwood, J. H. Waite Jr., T. E. Moore, J. F. E. Johnson, and C. R. Chappell. A new source of suprathermal o^+ ions near the dayside polar cap boundary. *J. Geophys. Res.*, 90:4099, 1985.

[66] M. Loranc, W. B. Hanson, R. A. Heelis, and J. P. St.-Maurice. A morphological study of vertical ionospheric flows in the high-latitude F region. *J. Geophys. Res.*, 96:3627, 1991.

[67] G. Lu, P. H. Reif, T. E. Moore, and R. A. Heelis. Upflowing ionospheric ions in the auroral region. *J. Geophys. Res.*, 97:16855, 1992.

[68] E. J. Lund, E. Möbius, C. W. Carlson, R. E. Ergun, L. M. Kistler, B. Klecker, D. M. Klumpar, J. P. McFadden, M. A. Popecki, R. J. Strangeway, and Y. K. Tung. Transverse ion acceleration mechanisms in the aurora at solar minimum: occurrence distributions. *J. Atmos. Sol.-Terr. Phys.*, 62(6):467, 2000.

[69] K. Lynch, R. Arnoldy, P. M. Kintner, and J. Bonnell. The AMICIST auroral sounding rocket - A comparison of transverse ion acceleration mechanisms. *Geophys. Res. Lett.*, 21:1847, 1996.

[70] J. E. Maggs and T. N. Davis. Measurement of the thicknesses of auroral structures. *Planet. Space Sci.*, 16(2):205, 1968.

[71] M. G. McHarg, D. L. Hampton, and H. Steinbeck. Fast photometry of flickering aurora in discrete auroral arcs. *Geophys. Res. Lett.*, 25:2637, 1998.

[72] H. M. Mott-Smith and I. Langmuir. The theory of collectors in gaseous discharges. *Physical Review*, 28:727, 1926.

[73] F. S. Mozer, C. W. Carlson, M. K. Hudson, R. B. Torbert, B. Parady, J. Yatteau, and M. C. Kelley. Observations of paired electrostatic shocks in the polar magnetosphere. *Phys. Rev. Lett.*, 38(6):292, 1977.

[74] F. S. Mozer, R. Ergun, M. Temerin, C. Cattell, J. Dombeck, and J. Wygant. New features of time domain electric-field structures in the auroral acceleration region. *Phys. Rev. Lett.*, 79(7):1281, 1997.

[75] T. Nagai, J. H. Waite Jr., J. L. Green, C. R. Chappell, R. C. Olsen, and R. H. Comfort. First measurements of supersonic polar wind in the polar magnetosphere. *Geophys. Res. Lett.*, 11:669, 1984.

[76] M. V. Nezlin. Negative-energy waves and the anomalous Doppler effect. *Sov. Phys. Usp.*, 19(11):946, 1976.

[77] K.-I. Nishikawa, G. Ganguli, Y. C. Lee, and P. J. Palmadesso. Simulation of ion-cyclotron-like modes in a magnetoplasma with transverse inhomogeneous electric field. *Phys. Fluids*, 31(6):1568, 1988.

[78] P. Norqvist, M. André, and M. Tyrland. A statistical study of ion energization mechanisms in the auroral region. *J. Geophys. Res.*, 103:23459, 1998.

[79] P. Palmadesso, G. Ganguli, and Y. C. Lee. A new mechanism for excitation of waves in a magnetoplasma: II. Wave-particle and nonlinear aspects. In *Ion Acceleration in the Magnetosphere and Ionosphere, Geophys. Monogr. Ser. Vol. 38*, page 301, Washington, DC, 1986. AGU.

[80] P. J. Palmadesso, T. P. Coffey, S. L. Ossakow, and K. Papadopoulos. Fast photometry of flickering aurora in discrete auroral arcs. *Geophys. Res. Lett.*, 1:105, 1974.

[81] J. R. Peñano and G. Ganguli. Ionospheric source for low-frequency broadband electromagnetic signatures. *Phys. Rev. Lett.*, 83(7):1343, 1999.

[82] J. R. Peñano and G. Ganguli. Generation of elf electromagnetic waves in the ionosphere by localized transverse dc electric fields: Subcyclotron frequency regime. *J. Geophys. Res.*, 105(A4):7441, 2000.

[83] J. R. Peñano and G. Ganguli. Generation of electromagnetic ion cyclotron waves in the ionosphere by localized transverse dc electric fields. *J. Geophys. Res.*, 107(A8):1189, 2002.

[84] J. R. Peñano, G. Ganguli, W. E. Amatucci, D. N. Walker, and V. Gavrishchaka. Velocity shear-driven instabilities in a rotating plasma. *Phys. Plasmas*, 5(12):4377, 1998.

[85] T. A. Potemra, J. P. Doering, W. K. Petersen, C. O. Bostrom, R. A. Hoffman, and L. H. Brace. AE-C observations of low-energy particles and ionospheric temperatures in the turbulent polar cusp: Evidence for the Kelvin-Helmholtz instability. *J. Geophys. Res.*, 83:3877, 1978.

[86] J. Providakes, D. Farley, W. Swartz, and D. Riggin. Plasma irregularities associated with a morning discrete auroral arc: Radar interferometer observations and theory. *J. Geophys. Res.*, 90(A8):7513, 1985.

[87] N. Sato, M. Nakamura, and R. Hatakeyama. Three-dimensional double layers inducing ion-cyclotron oscillations in a collisionless plasma. *Phys. Rev. Lett.*, 57:1227, 1986.

[88] P. Satyanarayana, P. K. Chaturvedi, M. J. Keskinen, J. D. Huba, and S. L. Ossakow. Inhomogeneous plasma flows: A review of in situ observations and laboratory experiments. *J. Geophys. Res.*, 90(A12):12209, 1985.

[89] R. Scrittwieser and G. Eder, editors. *U-shaped double layers and associated ion-cyclotron instability*, 1984.

[90] C. E. Seyler. Nonlinear 3-d evolution of bounded kinetic alfven waves due to shear flow and collisionless tearing instability. *Geophys. Res. Lett.*, 15(8):756, 1988.

[91] C. E Seyler and K. Wu. Instability at the electron inertial scale. *J. Geophys. Res.*, 106(a10):21623, 2001.

[92] E. G. Shelley, R. G Johnson, and R. D. Sharp. Satellite observations of energetic heavy ions during a geomagnetic storm. *J. Geophys. Res.*, 77:6104, 1972.

[93] E. G. Shelley, W. K Peterson, A. G. Ghielmetti, and J. Geiss. The polar ionosphere as a source of energetic magnetospheric plasma. *Geophys. Res. Lett.*, 9:941, 1982.

[94] E. G. Shelley, R. D Sharp, and R. G Johnson. Satellite observations of an ionospheric acceleration mechanism. *Geophys. Res. Lett.*, 3:654, 1976.

[95] J. R. Smith, N. Hershkowitz, and P. Coakley. Inflection-point method of interpreting emissive probe characteristics. *Rev. Sci. Instrum.*, 50:210, 1979.

[96] K. Stasiewicz, Y. Khotyaintsev, M. Berthomier, and J.-E. Wahlund. Identification of widespread turbulence of dispersive alfvén waves. *Geophys. Res. Lett.*, 27(2):173, 2000.

[97] T. H. Stix. *The Theory of Plasma Waves*. McGraw-Hill, New York, NY, first edition, 1962.

[98] H. C. Straub, P. Renault, B. G. Lindsay, K. A. Smith, and R. F. Stebbings. Absolute partial and total cross sections for electron-impact ionization of argon from threshold to 1000 ev. *Phys. Rev. A*, 52(2):1115, 1995.

[99] W. E. Swartz and D. T. Farley. High-resolution measurements of turbulent structure in the equatorial electrojet. *J. Geophys. Res.*, 99:309, 1994.

[100] E. Thomas, Jr., J. D. Jackson, E. A. Wallace, and G. Ganguli. Observations of low frequency oscillations due to transverse sheared flows. *Phys. Plasmas*, 10(5):1191, 2003.

[101] R. T. Tsunoda, R. C. Livingston, J. F. Vickrey, R. A. Heelis, W. B. Hanson, F. J. Rich, and P. F. Bythrow. Day observations of thermal-ion upwellings at 800-km altitude: an ionospheric signature of the cleft ion fountain. *J. Geophys. Res.*, 94:15277, 1989.

[102] J.-E. Wahlund, A. I. Eriksson, B. Holback, M. H. Boehm, J. Bonnell, P. M. Kintner, C. E. Seyler, J. H. Clemmons, L. Eliasson, D. J. Knudsen, P. Norqvist, and L. J. Zanetti. Broadband ELF plasma emission during auroral energization 1. Slow ion acoustic waves. *J. Geophys. Res.*, 103:4343, 1998.

[103] J.-E. Wahlund, H. J. Opgenoorth, F. R. E. Forme, M. A. L. Persson, I. Häggström, and J. Lilensten. Electron energization in the topside auroral ionosphere: on the importance of ion-acoustic turbulence. *J. Atmos. Terr. Phys.*, 55:623, 1993.

[104] J. E. Wahlund, H. J. Opgenoorth, I. Häggström, K. J. Winser, and G. O. L. Jones. EISCAT observations of the topside ionospheric ion outflows during auroral activity; revisited. *J. Geophys. Res.*, 97:3019, 1992.

[105] J.-E. Wahlund, A. Yilmaz, M. Backrud, D. Sundkvist, A. Vaivads, D. Winningham, M. André, J. Balogh, A. Bonnell, S. Buchert, T. Carozzi, N. Cornilleau, M. Dunlop, A. I. Eriksson, A. Fazakerley, G. Gustafsson, M. Parrot, P. Robert, and A. Tjulin. Observations of auroral broadband emissions by CLUSTER. *Geophys. Res. Lett.*, 30(11):1563, 2003.

[106] D. N. Walker, W. E. Amatucci, G. Ganguli, J. A. Antoniades, J. H. Bowles, and D. Duncan. Perpendicular ion heating by velocity-shear-driven waves. *Geophys. Res. Lett.*, 24(10):1187, 1997.

[107] T. Watari, T. Hatori, R. Kumazawa, S. Hidekuma, T. Aoki, T. Kawamoto, M. Inutake, A. Hiroe, S. Nishizawa, K. Adati, T. Sato, T. Watanabe, H. Obayashi, and K. Takayama. Radio-frequency plugging of a high density plasma. *Phys. Fluids*, 21(11):2076, 1978.

[108] J. Willig, R. L. Merlino, and N. D'Angelo. Experimental study of the parallel velocity shear instability. *Phys. Lett. A*, 236(3):223, 1997.

[109] A. Yau, B. Whalen, A. McNamara, P. Kellogg, and W. Bernstein. Particle and wave observations of low-altitude ionospheric ion acceleration events. *J. Geophys. Res.*, 88:341, 1983.

[110] A. W. Yau and M. André. Sources of ion outflow in th ehigh latitude ionosphere. *Space Sci. Rev.*, 80:1, 1997.

Appendices

Appendix A

Dispersion Relation for Electromagnetic Waves in Presence of Transverse Velocity Shear

A.1 Model Derivation

We are following the derivation in the 2000 JGR paper by Peñano and Ganguli. Ion and perpendicular electron dynamics can be described by the cold fluid equations:

$$\frac{\partial n_\alpha}{\partial t} + \nabla \cdot (n_\alpha \mathbf{v}_\alpha) = 0 \tag{A.1}$$

$$\left(\frac{\partial}{\partial t} + \mathbf{v}_\alpha \cdot \nabla\right) \mathbf{v}_\alpha = \frac{q}{m_\alpha} \left(\mathbf{E} + \mathbf{v}_\alpha \times \mathbf{B}\right), \tag{A.2}$$

where α refers to particle species. We linearize the above equations by assuming the following forms:

$$\begin{aligned} \mathbf{B} &= B_0 \hat{z} + \mathbf{B_1}(x) \exp\left[i\left(k_y y + k_z z - \omega t\right)\right] \\ \mathbf{E} &= E_0(x) \hat{x} + \mathbf{E_1}(x) \exp\left[i\left(k_y y + k_z z - \omega t\right)\right] \\ \mathbf{v}_\alpha &= v_{\alpha 0}(x) \hat{y} + \mathbf{v}_{\alpha \mathbf{1}}(x) \exp\left[i\left(k_y y + k_z z - \omega t\right)\right] \end{aligned} \tag{A.3}$$

The 0 subscripts refer to the equilibrium values for each quantity,and $v_{\alpha 0}$ is the $\mathbf{E} \times \mathbf{B}$ velocity $v_E = -E_0(x)/B_0 \hat{y}$. Linearizing the equation of motion, we arrive at the following system of equations:

$$\begin{aligned} -i\omega_1 v_{\alpha 1x} &= \frac{q}{m_\alpha}\left(E_{1x} + v_E B_{1z} + v_{1y} B_0\right) \\ -i\omega_1 v_{\alpha 1y} + v_{\alpha 1x}\frac{\partial v_E}{\partial x} &= \frac{q}{m_\alpha}\left(E_{1y} - v_{1x} B_0\right) \\ -i\omega_1 v_{i1z} &= \frac{e}{m_i}\left(E_{1z} - v_E B_{1z}\right), \end{aligned}$$

where $\omega_1 = \omega - k_y v_E$. Note that the third equation above is only for the ions. We will deal with the parallel motion of the electrons separately. The above system of equations can be solved for the following velocities:

$$\begin{aligned} v_{\alpha 1x} &= \frac{1}{\Omega_\alpha^2 D_\alpha}\frac{q}{m_\alpha}\left[E_{1y}\Omega_\alpha - i\omega_1\left(E_{1x} + v_E B_{1z}\right)\right] \\ v_{\alpha 1y} &= -\frac{1}{\Omega_\alpha^2 D_\alpha}\frac{q}{m_\alpha}\left[\Omega_\alpha \eta_\alpha\left(E_{1x} + v_E B_{1z}\right) + i\omega_1 E_{1y}\right] \\ v_{i1z} &= \frac{i}{\omega_1}\frac{q}{m_i}\left[E_{1z} - v_E B_{1x}\right], \end{aligned} \tag{A.4}$$

where $\Omega_\alpha = \frac{qB_0}{m_\alpha}$, $\eta_\alpha = 1 + \frac{1}{\Omega_\alpha}\frac{\partial v_E}{\partial x}$, and $D_\alpha = \eta_\alpha - \frac{\omega_1}{\Omega_\alpha^2}$. We can use Faraday's law to eliminate $\mathbf{B}_1$ in the above expressions. Due to the inhomogeneity in the $\hat{x}$-direction, we apply a spatial Fourier transform only in the $\hat{y}$- and $\hat{z}$-directions as shown above in Equation (A.3). The appropriate form for the del operator is $\nabla = \frac{\partial}{\partial x}\hat{x} + ik_y\hat{y} + ik_z\hat{z}$. Applying this in the expression for Faraday's law, we can write the following expressions for the first order magnetic fluctuations:

$$\begin{aligned} B_{1x} &= \frac{k_y}{\omega}E_{1z} - \frac{k_z}{\omega}E_{1y} \\ B_{1y} &= \frac{k_z}{\omega}E_{1x} + \frac{i}{\omega}\frac{\partial E_{1z}}{\partial x} \\ B_{1z} &= -\frac{i}{\omega}\frac{\partial E_{1y}}{\partial x} - \frac{k_y}{\omega}E_{1x}. \end{aligned} \tag{A.5}$$

Substituting Equation (A.5) into Equation (A.4), we are left with expressions for the first order velocities in terms of the electric field fluctuations:

$$\begin{aligned} v_{\alpha 1x} &= \frac{1}{\Omega^2 D_\alpha}\frac{q}{m_\alpha}\left(\Omega_\alpha E_{1y} - v_E\frac{\omega_1}{\omega}\frac{\partial E_{1y}}{\partial x} - i\frac{\omega_1^2}{\omega}E_{1x}\right) \\ v_{\alpha 1y} &= -\frac{1}{\Omega^2 D_\alpha}\frac{q}{m_\alpha}\left(\frac{\Omega_\alpha\eta_\alpha\omega_1}{\omega}E_{1x} + i\omega_1 E_{1y} - iv_E\frac{\Omega_\alpha\eta_\alpha}{\omega}\frac{\partial E_{1y}}{\partial x}\right) \\ v_{i1z} &= \frac{i}{\omega_1}\frac{e}{m_i}\left(\frac{\omega_1}{\omega}E_{1z} + \frac{k_z v_E}{\omega}E_{1y}\right). \end{aligned} \tag{A.6}$$

We are now in a position to determine the expression for the first order perpendicular current density:

$$\mathbf{J}_{1\perp} = \rho_1 v_E\hat{y} + \sum_\alpha q n_{\alpha 0}\mathbf{v}_{\alpha 1\perp}, \tag{A.7}$$

where ρ_1 is a placeholder for the first order charge density fluctuations that we will determine from the continuity equation later. Substituting the velocities in the $\hat{x}$- and $\hat{y}$-directions from Equation (A.6), we arrive at the following expressions for the perpendicular components of $\mathbf{J}_1$:

$$J_{1x} = -i\omega\epsilon_0\sum_\alpha\frac{\omega_{p\alpha}^2}{\omega^2\Omega_\alpha^2 D_\alpha}\left(\omega_1^2 E_{1x} + i\omega\Omega_\alpha E_{1y} - i\omega_1 v_E\frac{\partial E_{1y}}{\partial x}\right) \tag{A.8}$$

$$J_{1y} = \rho_1 v_E - i\omega\epsilon_0\sum_\alpha\frac{\omega_{p\alpha}^2}{\omega^2\Omega_\alpha^2 D_\alpha}\left(\omega\omega_1 E_{1y} - \Omega_\alpha\eta_\alpha v_E\frac{\partial E_{1y}}{\partial x} - i\Omega_\alpha\eta_\alpha\omega_1 E_{1x}\right), \tag{A.9}$$

where the plasma frequency for a given species α is given by $\omega_{p\alpha}^2 = \frac{e^2 n_{\alpha 0}}{\epsilon_0 m_\alpha}$.

The first order current density parallel to the background magnetic field can be written as the sum of the ion and electron contributions: $J_{1z} = J_{i1z} + J_{e1z}$. The ion contribution can be calculated using the $\hat{z}$ component from Equation (A.6):

$$J_{i1z} = i\omega\epsilon_0\left(\frac{\omega_{pi}^2}{\omega}\right)\left(E_{1z} + \frac{k_z v_E}{\omega_1}E_{1y}\right). \tag{A.10}$$

Electron Landau damping is retained by keeping the lowest-order kinetic contributions to J_{e1z}.

$$J_{e1z} = i\omega\epsilon_0 \left(\frac{\omega_{pe}^2}{\omega^2}\right) \zeta_e^2 Z'(\zeta_e) \left(E_{1z} + \frac{k_z v_E}{\omega_1} E_{1y}\right), \tag{A.11}$$

where $\zeta_e = \omega_1 / \left(\sqrt{2} k_z v_{the}\right)$, $v_{the} = \sqrt{T_e/m_e}$, and Z' is the derivative of the plasma dispersion function with respect to its argument. The perturbed parallel current density is

$$J_{1z} = -i\omega\epsilon_0 \left(P - 1\right) \left(E_{1z} + \frac{k_z v_E}{\omega_1} E_{1y}\right), \tag{A.12}$$

where $P = 1 - \frac{\omega_{pi}^2}{\omega^2} - \frac{\omega_{pe}^2}{\omega^2}\zeta_e^2 Z'\left(\zeta_e\right)$. Using a linearized version of Equation (A.1), we arrive at the following expression for the perturbed charge density

$$\begin{aligned} \rho_1 = &- i\frac{\omega\epsilon_0}{\omega_1}\left\{\frac{\partial}{\partial x}\left[\sum_\alpha \frac{\omega_{p\alpha}^2}{\omega^2\Omega_\alpha^2 D_\alpha}\left(\omega_1^2 E_{1x} + i\omega\Omega_\alpha E_{1y} - i\omega_1 v_E \frac{\partial E_{1y}}{\partial x}\right)\right]\right. \\ &+ ik_y \sum_\alpha \frac{\omega_{p\alpha}^2}{\omega^2\Omega_\alpha^2 D_\alpha}\left(\omega\omega_1 E_{1y} - \Omega_\alpha\eta_\alpha v_E \frac{\partial E_{1y}}{\partial x} - i\Omega_\alpha\eta_\alpha\omega_1 E_{1x}\right) \\ &\left. + ik_z\left(P-1\right)\left(E_{1z} + \frac{k_z v_E}{\omega_1}E_{1y}\right)\right\}. \end{aligned} \tag{A.13}$$

Taking the curl of Faraday's law and substituting Ampere's law, we can write the wave equation as

$$\nabla \times \nabla \times \tilde{\mathbf{E}}_1 - \frac{\omega^2}{c^2}\left(\tilde{\mathbf{E}}_1 - \frac{1}{i\omega\epsilon_0}\tilde{\mathbf{J}}_1\right) = 0. \tag{A.14}$$

This can be written as the following matrix equation:

$$\mathbf{M} \cdot \mathbf{E}_1 = 0, \tag{A.15}$$

where the vector $\mathbf{E}_1$ is

$$\mathbf{E}_1 = \begin{pmatrix} E_{1x} \\ E_{1y} \\ E_{1z} \end{pmatrix} \tag{A.16}$$

and we will determine the matrix elements individually. Note that in writing Equation (A.15) we have multiplied Equation (A.14) by $-\frac{c^2}{\omega^2}$.

$$M_{11} = 1 - \frac{k_y^2 c^2}{\omega^2} - \frac{k_z^2 c^2}{\omega^2} + \sum_\alpha \frac{\omega_{p\alpha}^2}{\omega^2}\frac{\omega_1^2}{\Omega_\alpha^2 D_\alpha} \tag{A.17}$$

$$M_{12} = -i\left[\frac{k_y^2 c^2}{\omega^2} + \sum_\alpha \frac{\omega_{p\alpha}^2}{\omega^2}\frac{\omega_1 v_E}{\Omega_\alpha^2 D_\alpha}\right]\frac{\partial}{\partial x} + i\sum_\alpha \frac{\omega_{p\alpha}^2}{\omega^2}\frac{\omega}{\Omega_\alpha D_\alpha} \tag{A.18}$$

$$M_{13} = -i\frac{k_z c^2}{\omega^2}\frac{\partial}{\partial x} \tag{A.19}$$

$$M_{21} = -i\left[\frac{k_y c^2}{\omega^2} + \sum_\alpha \frac{\omega_{p\alpha}^2}{\omega^2}\frac{\omega_1 v_E}{\Omega_\alpha^2 D_\alpha}\right]\frac{\partial}{\partial x} - i\frac{v_E}{\omega_1}\frac{\partial}{\partial x}\left(\sum_\alpha \frac{\omega_{p\alpha}^2}{\omega^2}\frac{\omega_1^2}{\Omega_\alpha^2 D_\alpha}\right) - i\sum_\alpha \frac{\omega_{p\alpha}^2}{\omega}\frac{\Omega_\alpha \eta_\alpha \omega}{\Omega_\alpha^2 D_\alpha}$$

Note that the derivative in the second term above is not applied to the electric field vector. Expand η_α in the third term and rearrange the terms:

$$\begin{aligned}M_{21} =& -i\left[\frac{k_y c^2}{\omega^2} + \sum_\alpha \frac{\omega_{p\alpha}^2}{\omega^2}\frac{\omega_1 v_E}{\Omega_\alpha^2 D_\alpha}\right]\frac{\partial}{\partial x} - i\sum_\alpha \frac{\omega_{p\alpha}^2}{\omega^2}\frac{\omega}{\Omega_\alpha D_\alpha} \\ &- \frac{i}{\omega_1}\left[v_E\frac{\partial}{\partial x}\left(\sum_\alpha \frac{\omega_{p\alpha}^2}{\omega^2}\frac{\omega_1^2}{\Omega_\alpha^2 D_\alpha}\right) + \sum_\alpha \frac{\omega_{p\alpha}^2}{\omega}\frac{\omega_1}{\Omega_\alpha^2 D_\alpha}\frac{\partial}{\partial x}\left(\omega - k_y v_E + k_y v_E\right)\right]\end{aligned}$$

Let's focus on the last term in brackets. Since, $\omega_1 = \omega - k_y v_E$ the terms in the parentheses goes to $\omega_1 + k_y v_E$. The ω_1 part of this term can combine with the first term in the brackets allowing us to take the v_E into the derivative.

$$\begin{aligned}M_{21} =& -i\left[\frac{k_y c^2}{\omega^2} + \sum_\alpha \frac{\omega_{p\alpha}^2}{\omega^2}\frac{\omega_1 v_E}{\Omega_\alpha^2 D_\alpha}\right]\frac{\partial}{\partial x} - i\sum_\alpha \frac{\omega_{p\alpha}^2}{\omega^2}\frac{\omega}{\Omega_\alpha D_\alpha} \\ &- \frac{i}{\omega_1}\left[\frac{\partial}{\partial x}\left(\sum_\alpha \frac{\omega_{p\alpha}^2}{\omega^2}\frac{\omega_1^2 v_E}{\Omega_\alpha^2 D_\alpha}\right) + \sum_\alpha \frac{\omega_{p\alpha}^2}{\omega^2}\frac{\omega_1 k_y v_E}{\Omega_\alpha^2 D_\alpha}\frac{\partial v_E}{\partial x}\right]\end{aligned}$$

Again focusing on last term in brackets, take the derivative of one ω_1 in the first term. One of the resulting terms will cancel the second term in brackets. By adding a constant within the derivative, we arrive at the final form for this term.

$$\begin{aligned}M_{21} =& -i\left[\frac{k_y c^2}{\omega^2} + \sum_\alpha \frac{\omega_{p\alpha}^2}{\omega^2}\frac{\omega_1 v_E}{\Omega_\alpha^2 D_\alpha}\right]\frac{\partial}{\partial x} - i\sum_\alpha \frac{\omega_{p\alpha}^2}{\omega^2}\frac{\omega}{\Omega_\alpha D_\alpha} \\ &- i\frac{\partial}{\partial x}\left[\frac{k_y c^2}{\omega^2} + \sum_\alpha \frac{\omega_{p\alpha}^2}{\omega^2}\frac{\omega_1 v_E}{\Omega_\alpha^2 D_\alpha}\right]\end{aligned}\tag{A.20}$$

Again it is important to note that the derivative in the last term does not act on the electric field vector.

$$\begin{aligned}M_{22} =& \left(\frac{c^2}{\omega^2} - \sum_\alpha \frac{\omega_{p\alpha}^2}{\omega^2}\frac{v_E^2}{\Omega_\alpha^2 D_\alpha}\right)\frac{\partial^2}{\partial x^2} + 1 - \frac{k_z^2 c^2}{\omega^2} + \frac{k_z^2 v_E^2}{\omega_1^2}\left(P-1\right) + \frac{v_E}{\omega_1}\frac{\partial}{\partial x}\left(\sum_\alpha \frac{\omega_{p\alpha}^2}{\omega^2}\frac{\omega\Omega_\alpha}{\Omega_\alpha^2 D_\alpha}\right) \\ &+ \sum_\alpha \frac{\omega_{p\alpha}^2}{\omega^2}\frac{k_y v_E \omega}{\Omega_\alpha^2 D_\alpha} + \sum_\alpha \frac{\omega_{p\alpha}^2}{\omega^2}\frac{\omega_1 \omega}{\Omega_\alpha^2 D_\alpha} - \sum_\alpha \frac{\omega_{p\alpha}^2}{\omega^2}\frac{v_E \omega}{\omega_1 \Omega_\alpha^2 D_\alpha}\left(\Omega_\alpha + \frac{\partial v_E}{\partial x}\right)\frac{\partial}{\partial x} \\ &- \frac{v_E}{\omega_1}\frac{\partial}{\partial x}\left(\sum_\alpha \frac{\omega_{p\alpha}^2}{\omega^2}\frac{\omega_1 v_E}{\Omega_\alpha^2 D_\alpha}\frac{\partial}{\partial x}\right)\end{aligned}$$

The derivative in the fifth term does not act on the electric field vector, however, all others do. We take a derivative of ω_1 in the last term.

$$\begin{aligned}M_{22} = &\left(\frac{c^2}{\omega^2} - \sum_\alpha \frac{\omega_{p\alpha}^2}{\omega^2}\frac{v_E^2}{\Omega_\alpha^2 D_\alpha}\right)\frac{\partial^2}{\partial x^2} + 1 - \frac{k_z^2 c^2}{\omega^2} + \frac{k_z^2 v_E^2}{\omega_1^2}\left(P-1\right) + \frac{v_E}{\omega_1}\frac{\partial}{\partial x}\left(\sum_\alpha \frac{\omega_{p\alpha}^2}{\omega^2}\frac{\omega\Omega_\alpha}{\Omega_\alpha^2 D_\alpha}\right)\\ &+ \sum_\alpha \frac{\omega_{p\alpha}^2}{\omega^2}\frac{k_y v_E \omega}{\Omega_\alpha^2 D_\alpha} + \sum_\alpha \frac{\omega_{p\alpha}^2}{\omega^2}\frac{\omega_1\omega}{\Omega_\alpha^2 D_\alpha} - \sum_\alpha \frac{\omega_{p\alpha}^2}{\omega^2}\frac{v_E\omega\Omega_\alpha}{\omega_1\Omega_\alpha^2 D_\alpha}\frac{\partial}{\partial x} - \sum_\alpha \frac{\omega_{p\alpha}^2}{\omega^2}\frac{v_E\omega}{\omega_1\Omega_\alpha^2 D_\alpha}\frac{\partial v_E}{\partial x}\frac{\partial}{\partial x}\\ &+ \frac{v_E}{\omega_1}\sum_\alpha \frac{\omega_{p\alpha}^2}{\omega^2}\frac{k_y v_E}{\Omega_\alpha^2 D_\alpha}\frac{\partial v_E}{\partial x}\frac{\partial}{\partial x} - v_E\frac{\partial}{\partial x}\left(\sum_\alpha \frac{\omega_{p\alpha}^2}{\omega^2}\frac{v_E}{\Omega_\alpha^2 D_\alpha}\right)\frac{\partial}{\partial x}\end{aligned}$$

The first term and last three terms can be combined, and we arrive at the following expression.

$$\begin{aligned}M_{22} = &\frac{\partial}{\partial x}\left[\left(\frac{c^2}{\omega^2} - \sum_\alpha \frac{\omega_{p\alpha}^2}{\omega^2}\frac{v_E^2}{\Omega_\alpha^2 D_\alpha}\right)\frac{\partial}{\partial x}\right] + 1 - \frac{k_z^2 c^2}{\omega^2} + \frac{k_z^2 v_E^2}{\omega_1^2}\left(P-1\right) + \sum_\alpha \frac{\omega_{p\alpha}^2}{\omega^2}\frac{k_y v_E\omega}{\Omega_\alpha^2 D_\alpha}\\ &+ \frac{v_E}{\omega_1}\frac{\partial}{\partial x}\left(\sum_\alpha \frac{\omega_{p\alpha}^2}{\omega^2}\frac{\omega\Omega_\alpha}{\Omega_\alpha^2 D_\alpha}\right) + \sum_\alpha \frac{\omega_{p\alpha}^2}{\omega^2}\frac{\omega_1\omega}{\Omega_\alpha^2 D_\alpha} - \sum_\alpha \frac{\omega_{p\alpha}^2}{\omega^2}\frac{\Omega_\alpha\eta_\alpha v_E\omega}{\omega_1\Omega_\alpha^2 D_\alpha}\frac{\partial}{\partial x}\end{aligned}$$

We evaluate the derivative in the sixth term and notice that one of the resulting terms cancels the last term. We also rewrite the fifth term by taking $k_y v_E = \omega - \omega_1$ and notice that the ω_1 term cancels with the seventh term.

$$\begin{aligned}M_{22} = &\frac{\partial}{\partial x}\left[\left(\frac{c^2}{\omega^2} - \sum_\alpha \frac{\omega_{p\alpha}^2}{\omega^2}\frac{v_E^2}{\Omega_\alpha^2 D_\alpha}\right)\frac{\partial}{\partial x}\right] + 1 - \frac{k_z^2 c^2}{\omega^2} + \frac{k_z^2 v_E^2}{\omega_1^2}\left(P-1\right)\\ &+ \sum_\alpha \frac{\omega_{p\alpha}^2}{\Omega_\alpha^2 D_\alpha} + \sum_\alpha \frac{\omega_{p\alpha}^2}{\omega^2}\frac{\omega v_E}{\omega_1\Omega_\alpha}\frac{\partial}{\partial x}\left(\frac{1}{D_\alpha}\right)\end{aligned}$$

We add and subtract the term $\sum_\alpha \frac{\omega_{p\alpha}^2}{\Omega_\alpha^2 D_\alpha}\frac{\Omega_\alpha}{\omega_1^2}\frac{\partial v_E}{\partial x}$, and we combine the term we added and the last term above to write the following.

$$\begin{aligned}M_{22} = &\frac{\partial}{\partial x}\left[\left(\frac{c^2}{\omega^2} - \sum_\alpha \frac{\omega_{p\alpha}^2}{\omega^2}\frac{v_E^2}{\Omega_\alpha^2 D_\alpha}\right)\frac{\partial}{\partial x}\right] + 1 - \frac{k_z^2 c^2}{\omega^2} + \frac{k_z^2 v_E^2}{\omega_1^2}\left(P-1\right)\\ &- \sum_\alpha \frac{\omega_{p\alpha}^2}{\Omega_\alpha^2 D_\alpha}\left(\frac{\Omega_\alpha}{\omega_1^2}\frac{\partial v_E}{\partial x} - 1\right) + \frac{\partial}{\partial x}\left[\sum_\alpha \frac{\omega_{p\alpha}^2}{\omega^2}\left(\frac{\omega v_E}{\omega_1\Omega_\alpha D_\alpha}\right)\right]\end{aligned} \tag{A.21}$$

Note that only the derivatives in the first term act on the electric field vector.

$$M_{23} = \frac{k_y k_z c^2}{\omega^2} + \frac{k_z v_E}{\omega_1}\left(P-1\right) \tag{A.22}$$

$$M_{31} = -i\frac{k_z c^2}{\omega^2}\frac{\partial}{\partial x} \tag{A.23}$$

$$M_{32} = \frac{k_y k_z c^2}{\omega^2} + \frac{k_z v_E}{\omega_1}(P-1) \tag{A.24}$$

$$M_{33} = P - \frac{k_y^2 c^2}{\omega^2} + \frac{c^2}{\omega^2}\frac{\partial^2}{\partial x^2} \tag{A.25}$$

We can use Equations (A.17-A.25) to rewrite Equation (A.15) as

$$\frac{\partial}{\partial x}\left(\mathbf{A}\cdot\frac{\partial \mathbf{E}_1}{\partial x}\right) + \mathbf{B}\cdot\frac{\partial \mathbf{E}_1}{\partial x} + \frac{\partial}{\partial x}\left(\mathbf{B}^T\cdot\mathbf{E}_1\right) + \mathbf{C}\cdot\mathbf{E}_1 = 0, \tag{A.26}$$

where we have grouped terms that contain derivatives of the electric field vector. We could alternatively write the expression as

$$\begin{pmatrix} C_{11} & B_{12}\frac{\partial}{\partial x} + C_{12} & B_{13}\frac{\partial}{\partial x} \\ \frac{\partial B_{12}}{\partial x} + B_{12}\frac{\partial}{\partial x} - C_{12} & \frac{\partial A_{22}}{\partial x}\frac{\partial}{\partial x} + A_{22}\frac{\partial^2}{\partial x^2} + C_{22} & C_{23} \\ \frac{\partial B_{13}}{\partial x} + B_{13}\frac{\partial}{\partial x} & C_{23} & A_{33}\frac{\partial^2}{\partial x^2} + C_{33} \end{pmatrix}\begin{pmatrix} E_{1x} \\ E_{1y} \\ E_{1z} \end{pmatrix} = 0. \tag{A.27}$$

The individual matrix elements used above are given below.

$$A_{22} = \frac{c^2}{\omega^2} - \sum_\alpha \frac{\omega_{p\alpha}^2}{\omega^2}\frac{v_E^2}{\Omega_\alpha^2 D_\alpha} \tag{A.28}$$

$$A_{33} = \frac{c^2}{\omega^2} \tag{A.29}$$

$$B_{12} = -i\left[\frac{k_y c^2}{\omega^2} + \sum_\alpha \frac{\omega_{p\alpha}^2}{\omega^2}\frac{\omega_1 v_E}{\Omega_\alpha^2 D_\alpha}\right] \tag{A.30}$$

$$B_{13} = -i\frac{k_z c^2}{\omega^2} \tag{A.31}$$

$$C_{11} = 1 - \frac{k_y^2 c^2}{\omega^2} - \frac{k_z^2 c^2}{\omega^2} + \sum_\alpha \frac{\omega_{p\alpha}^2}{\omega^2}\frac{\omega_1^2}{\Omega_\alpha^2 D_\alpha} \tag{A.32}$$

$$C_{12} = -C_{21} = i\sum_\alpha \frac{\omega_{p\alpha}^2}{\omega^2}\frac{\omega}{\Omega_\alpha D_\alpha} \tag{A.33}$$

$$\begin{aligned} C_{22} = 1 - \frac{k_z^2 c^2}{\omega^2} - \sum_\alpha \frac{\omega_{p\alpha}^2}{\Omega_\alpha^2 D_\alpha}\left(\frac{\Omega_\alpha}{\omega_1^2}\frac{\partial v_E}{\partial x} - 1\right) \\ + \frac{k_z^2 v_E^2}{\omega_1^2}(P-1) + \frac{\partial}{\partial x}\left[\sum_\alpha \frac{\omega_{p\alpha}^2}{\omega^2}\left(\frac{\omega v_E}{\omega_1 \Omega_\alpha D_\alpha}\right)\right] \end{aligned} \tag{A.34}$$

$$C_{23} = C_{32} = \frac{k_y k_z c^2}{\omega^2} + \frac{k_z v_E}{\omega_1}(P-1) \tag{A.35}$$

$$C_{33} = P - \frac{k_y^2 c^2}{\omega^2} \tag{A.36}$$

A.2 Zero Flow Limit

If there is no flow $v_E = 0$, then we can evaluate several parameters: $\eta_\alpha = 1$, $\omega_1 = \omega$, and $D_\alpha = \Omega_\alpha^2 - \omega^2$. Since there is no structure in the $\hat{x}$-direction, terms containing derivatives with respect to x are zero. Applying these conditions to Equation (A.27) results in the following expression:

$$\begin{pmatrix} S-\mu^2 & -iD & 0 \\ iD & S-\mu_z^2 & \mu_y\mu_z \\ 0 & \mu_y\mu_z & P-\mu_y^2 \end{pmatrix} \begin{pmatrix} E_{1x} \\ E_{1y} \\ E_{1z} \end{pmatrix} = 0, \tag{A.37}$$

where we have used that $k^2 = k_y^2 + k_z^2$ such that $\mu = \frac{kc}{\omega}$, $\mu_y = \frac{k_y c}{\omega}$, and $\mu_z = \frac{k_z c}{\omega}$.

$$S = 1 - \frac{\omega_{pi}^2}{\omega^2 - \Omega_i^2} - \frac{\omega_{pe}^2}{\omega^2 - \Omega_e^2} \tag{A.38}$$

$$D = \frac{\omega_{pi}^2}{\omega^2}\frac{\omega\Omega_i}{\Omega_i^2 - \omega^2} + \frac{\omega_{pe}^2}{\omega^2}\frac{\omega\Omega_e}{\Omega_e^2 - \omega^2} \tag{A.39}$$

As T_e goes to zero, ζ_e goes to infinity, and in the large argument limit $Z' \to \frac{1}{\zeta_e^2}$. In this limit P can be written as

$$P = 1 - \frac{\omega_{pi}^2}{\omega^2} - \frac{\omega_{pe}^2}{\omega^2} \tag{A.40}$$

Under the cold plasma limit, Equation (A.37) reduces to the standard wave equation with the cold plasma dielectric tensor as expected. S, D, and P are the standard “sum”, “difference”, and “principal” definitions contained in the cold plasma dielectric tensor.